Universidade de São Paulo
Instituto de Física

Rumo ao teletransporte entre átomos de rubídio e luz na banda C de telecomunicações

Luiz Couto Corrêa Pinto Filho

Orientador: Prof. Dr. **MARCELO MARTINELLI**
Coorientador: Prof. Dr. **BRENO MARQUES GONÇALVES TEIXEIRA**

Dissertação de mestrado apresentada ao Instituto de Física da Universidade de São Paulo como requisito parcial para obtenção do título de Mestre em Ciências.

Banca Examinadora:
Prof. Dr. Marcelo Martinelli - Orientador (USP)
Prof. Dr. Jose Wellington Rocha Tabosa (UFPE)
Prof. Dr. José Augusto Oliveira Huguenin (UFF)

São Paulo
2020

FICHA CATALOGRÁFICA
Preparada pelo Serviço de Biblioteca e Informação
do Instituto de Física da Universidade de São Paulo

Pinto Filho, Luiz Couto Corrêa

Rumo ao teletransporte entre átomos de rubídio e luz na banda C de telecomunicações. São Paulo, 2020.

Dissertação (Mestrado) – Universidade de São Paulo. Instituto de Física. Depto. de Física Experimental

Orientador: Prof. Dr. Marcelo Martinelli
Área de Concentração: Ótica Quântica, Informação Quântica

Unitermos: 1. Física; 2. Física experimental; 3. Mecânica quântica; 4. Óptica Quântica; 5. Física atômica.

USP/IF/SBI-073/2020

University of São Paulo
Physics Institute

Towards the teleportation between rubidium atoms and light in the telecom C-band

Luiz Couto Corrêa Pinto Filho

Supervisor: Prof. Dr. **MARCELO MARTINELLI**
Co-supervisor: Prof. Dr. **BRENO MARQUES GONÇALVES TEIXEIRA**

Dissertation submitted to the Physics Institute of the University of São Paulo in partial fulfilment of the requirements for the degree of Master of Science.

Examining Committee:
Prof. Dr. Marcelo Martinelli - Supervisor (USP)
Prof. Dr. Jose Wellington Rocha Tabosa (UFPE)
Prof. Dr. José Augusto Oliveira Huguenin (UFF)

São Paulo
2020

ACKNOWLEDGEMENTS

This research was supported in part by the grants 2017/27096-9 and 2019/13608-3, São Paulo Research Foundation (FAPESP).

CONTENTS

RESUMO

Rumo ao teletransporte entre átomos de rubídio e luz na banda C de telecomunicações

Nós desenvolvemos um sistema capaz de gerar emaranhamento bipartido, com resultados promissores na geração de emaranhamento tripartido em campos eletromagneticos instensos utilizando um Oscilador Paramétrico Óptico. Os campos gerados são ressonantes com a linha D2 do rubídio, a 780 nm para o bombeio refletido, e com a banda-C de telecomunicações, a 1560 nm para sinal e complementar. Nós verificamos que o ruído de fônons no cristal era responsável por introduzir ruído de fase e que ao baixar a temperatura do sistema o ruído diminuiria, melhorando as possibilidades de obter emaranhamento tripartido. Em um experimento distinto, nós construímos um sistema de bombeio óptico no qual, junto com um escudo magnético e campos magnéticos gerados por bobinas, fomos capazes de preparar e caracterizar um estado de polarização atômica com orientação $p = 0.9$ e um ruído de polarização de 2.6 dB acima do *shotnoise* em uma frequencia central de 23.5 kHz e uma largura de linha de 70 Hz. Esses dois sistemas foram contruídos como os primeiros passos para a implementação de um protocolo de teletransporte entre átomos e luz ressoantes em comprimentos de onda distintos, estabelecendo as bases para a implementação de uma rede quântica de comunicação.

Palavras-chave: Oscilador Paramétrico Óptico, Emaranhamento, Teletransporte, Polarização Atômica.

ABSTRACT

Towards the teleportation between rubidium atoms and light in the telecom C-band

We developed a system capable of generating bipartite entanglement, and with promising results towards the generation of tripartite entangled states of light, using an Optical Parametric Oscillator. The generated fields are resonant with the Rubidium D2 transition line at 780 nm for the reflected pump, and with the C-band of telecommunications channels at 1560 nm for signal and idler. We verified that phonon noise in the crystal was responsible for introducing phase noise and that lowering the temperature of the system would reduce the noise, improving the prospects of obtaining tripartite entanglement. In a separate experiment, we built an optical pumping system in which, along with a magnetic shield and magnetic fields generated by coils, we were able to prepare and characterize an atomic polarization state with an orientation $p = 0.9$ and a polarization noise of 2.6 dB above the shot noise limit at a central frequency of 23.5 kHz and a linewidth of 70 Hz. These two systems were built as the first steps towards the implementation of a teleportation protocol between atoms and light resonant at different wavelengths, setting the foundations for the implementation a quantum network.

Keywords: Optical Parametric Oscillator, Entanglement, Teleportation, Atomic Polarization.

ACRONYMS AND ABBREVIATIONS

AC	Alternating Current
AM	Amplitude Modulation
BS	Beamsplitter
DC	Direct Current
DFB	Distributed Feedback
DGCZ	Duan, Giedke, Cirac, Zoller
DROPO	Doubly Resonant Optical Parametric Oscillator
EOM	Electro-Optical Modulator
EPR	Einstein-Podolski-Rosen
FC	Fiber Coupler
FR	Faraday Rotator
FSR	Free Spectral Range
GWD	Gravitational-Wave Detector
HR	High Reflectivity
LF	Liot Filter
LIGO	Laser Interferometer Gravitational-Wave Observatory
LMCAL	Laboratory for Coherent Manipulation of Atoms and Light
MORS	Magneto-Optical Resonance Signal
NBI	Niels Bohr Institute
OPO	Optical Parametric Oscillator
PBS	Polarizing Beamsplitter
PD	Photodetector / Photodiode
PID	Proportional–Integral–Derivative
PM	Phase Modulation
PPKTP	Periodically Poled Potassium Titanyl Phosphate
PPT	Positive Partial Transpose
PZT	Lead Zirconate Titanate
QBA	Quantum Back-Action
RF	Radio Frequency
SFG	Sum Frequency Generation
SN	Shot-Noise
SNL	Shot-Noise Limit
SNR	Signal to Noise Ratio
SQL	Standard Quantum Limit
SROPO	Single Resonant Optical Parametric Oscillator
TROPO	Triply Resonant Optical Parametric Oscillator

x

Part I

Introduction

1 OBJECTIVES

An important way to manipulate quantum systems is through the application of a resonant optical field to read and prepare the quantum states of interest. The interaction between such systems is essential to the development of quantum computation and quantum information science and it can be done by using entangled light. Many quantum information protocols, such as quantum cryptography (Ekert, 1991) and quantum teleportation(Furusawa *et al.*, 1998), take advantage of entanglement to establish communication between quantum systems. However, given the impossibility of copying a quantum state, as stated in the no-cloning theorem (Wootters and Zurek, 1982), we can single out quantum teleportation as an essential resource to transfer quantum information between such systems.

Entangled light can be generated by simple procedures, for instance, via beam splitter operations. In the single photon regime one can create a single photon Fock state $|1\rangle$ and send it through one port of a symmetric beamsplitter, while we consider vacuum $|0\rangle$ as the input of the other. As consequence one obtains a path entangled state $(|0\rangle_A |1\rangle_B + |1\rangle_A |0\rangle_B)/\sqrt{2}$, where if a photon is found in one path, it is immediately known that there is no photon on the other. This is the minimal system in which entanglement can be obtained. However, often enough, quantum systems are resonant at different frequencies requiring the generation of entangled light at different wavelengths. In continuous variables systems a well known source of entangled light for such purposes is the Optical Parametric Oscillator (OPO).

The main purpose of this work is to start building the basis for the development of an experiment capable of preparing a quantum state in an atomic cloud and interact it with wavelengths compatible with optical transmission lines. Our lab has a long history in the development of entangled states of light using OPOs (Villar *et al.*, 2006; Coelho *et al.*, 2009; Barbosa *et al.*, 2018; Muñoz-Martínez *et al.*, 2018) that are a natural choice as a source of entanglement in our case. The know-how on the preparation and characterization of atomic polarization states was obtained through an internship at the Niels Bohr Institute (NBI) under the supervision of Professor Eugene Polzik.

The fact that rubidium cells are readily available in our lab and the fact that our Titanium Sapphire lasers can be easily tuned to the wavelengths of their atomic transitions (780 nm and 795 nm), made them a natural choice for the preparation of atomic polarization states. For this reason we decided to use a triply resonant OPO to generate tripartite entanglement between the reflected pump at 780 nm and the downconverted fields (signal and idler) at 1560 nm. The first is resonant with the rubidium D2 transition line and the last two propagate with low losses through the optical fibers already implemented by the telecommunication's infrastructure. This technique is interesting due to the possibility of integration of distinct parts of the quantum hardware. Atoms can play the role as memories (Specht *et al.*, 2011) while light is a natural information conveyor. The obtained entanglement is a fundamental part for teleportation and information processing protocols.

The second part of the current work demonstrates one of the necessary steps for the implementation of a quantum protocol involving those distinct wavelengths, the manipulation of an atomic polarization state. For that we use a bias magnetic field to define the quantization axis and the Larmor precession frequency while the optical pumping drives as many atoms as possible to the desired polarization state. For the characterization of the prepared state, we use the Magneto-Optical Resonance Signal (MORS) (Julsgaard *et al.*, 2004). Given that the atomic state preparation was performed at the NBI, the experiments were performed with cesium cells, which is the atomic species commonly used in their experiments. However, the transition from cesium to rubidium is straightforward and the same technique can be easily ported to prepare and characterize polarization states using the rubidium cells in our lab.

Ultimately, the long term goal is to prepare an atomic polarization state in the rubidium cells in our lab and, using the entangled states generated in our OPO, implement a teleportation protocol between atoms and light. Of course, given the duration of a master's program, there is not enough

available time to to build all these systems and make them work. That is why in this work, our intention is to take the first steps in that direction. First by fine tuning a system to the point of generating the entangled states of light necessary for the implementation of the teleportation protocol and then by learning how prepare and characterize the atomic state involved in that protocol.

This Master's thesis is divided in four parts. In part I we discuss our motivations and objectives and introduce some of the theory necessary to the general understanding of experiments in quantum optics. Part II has all the discussion regarding the generation of entangled states of light in our OPO. In part III we present the preparation and characterization of atomic polarization states developed at the NBI. Finally in part IV we discuss our accomplishments and talk about the next steps to be taken in order to achieve our final goals.

2 RELEVANT TOPICS IN QUANTUM OPTICS EXPERIMENTS

In this section we introduce the pertinent concepts to the general understanding of experiments in quantum optics. We begin with a description of the density operator where we will preferentially follow the work of Furusawa and van Loock (2011). Then we proceed to a brief introduction of optical cavities as presented in Bachor and Ralph (2019). We conclude with a general detection theory followed by the resonator detection technique for the measurement of phase fluctuations.

2.1 Density Operator Representation

Complex physical systems, such as a statistical mixture of quantum states, and their time evolution, are better described by the introduction of the density operator representation (Scully and Zubairy, 1997). Under this representation the state of the system is described by an operator instead of a vector. For the quantized electromagnetic field, a convenient description can be done with the help of a basis of Fock (number) states $\{|n\rangle\}$ as:

$$\rho = \sum C_{nm} \left|n\right\rangle \left\langle m\right| , \tag{2.1}$$

where C_{nm} are complex coefficients.

However, in quantum optics, coherent states are better suited to describe the physical systems involved. These are the states that are ideally produced by a laser source and in this sense are closer to a classical description of the field. An important characteristic of coherent states is that they possess the minimum uncertainty relations allowed by the Heisenberg uncertainty principle.

By definition, coherent states are eigenstates of the annihilation operator $\hat{a}$:

$$\hat{a} \left|\alpha\right\rangle = \alpha \left|\alpha\right\rangle , \tag{2.2}$$

where α are complex eigenvalues. They form an overcomplete set of states and can be used as a basis, despite not being an orthogonal set. We can write a coherent state as a displaced vacuum state by introducing the displacement operator $\hat{D}(\alpha)$:

$$\hat{D}(\alpha) = \exp\left(\alpha\, \hat{a}^{\dagger} - \alpha^{*}\, \hat{a}\right) = \exp\left(2ip_{\alpha}\, \hat{x} - 2ix_{\alpha}\, \hat{p}\right) , \tag{2.3}$$

where we introduce a pair of quadrature operators $\hat{x}$ and $\hat{p}$ such that $\hat{a} = \hat{x} + i\hat{p}$ and $\alpha = x_{\alpha} + ip_{\alpha}$. Then, we write the coherent state as:

$$\left|\alpha\right\rangle = D(\alpha) \left|0\right\rangle . \tag{2.4}$$

Another important operation performed on the states generated in the laboratory is squeezing. This operation reduces the fluctuations in one of the quadratures while increasing the uncertainty on its conjugate. As a consequence, a coherent squeezed state is still bounded by Heisenberg's uncertainty principle, even if one quadrature is squeezed beyond its standard quantum limit. The squeezing operator may be defined as

$$\hat{S}(\zeta) = \exp\left(\frac{\zeta^{*}}{2}\hat{a}^{2} - \frac{\zeta}{2}\hat{a}^{\dagger 2}\right) , \tag{2.5}$$

where $\zeta \equiv r\exp(i\Theta)$, r is the squeezing parameter and Θ a phase.

There are many different mappings of the density operator in the basis of coherent states (Schleich, 2001). One of the commonly used is the P-representation (or Glauber-Sudarshan representation):

$$\rho = \int P(\alpha) \left|\alpha\right\rangle \left\langle\alpha\right| \mathrm{d}^{2}\alpha, \tag{2.6}$$

where $\mathrm{d}^{2}\alpha = \mathrm{d}(\mathrm{Re}\{\alpha\})\mathrm{d}(\mathrm{Im}\{\alpha\})$. In most cases we want to represent these quantum states in a way that is more convenient to compute expectation values of phase space variables. The most popular representation for that is the Wigner Function (Furusawa and van Loock, 2011).

2.1.1 Wigner Function

One way to uniquely determine the density operator is through its characteristic function $\chi(\eta)$ which in symmetric order is given by:

$$\chi(\eta) = \mathrm{Tr}\left\{\rho\, \mathrm{e}^{\eta a^\dagger - \eta^* a}\right\}. \tag{2.7}$$

The Wigner function may then be defined as the Fourier transform of the characteristic function:

$$W(\alpha) = \frac{1}{\pi^2}\int \mathrm{e}^{(\eta^*\alpha - \eta\,\alpha^*)}\,\chi(\eta)\,\mathrm{d}^2\eta. \tag{2.8}$$

This function always exists for a given state but is not necessarily positive, which is one of the reasons the Wigner function can not be considered a real probability distribution and why it is often referred to as a quasi-probability distribution.

There is an important aspect regarding the negativity of the Wigner function. States with negative valued Wigner functions cannot be generated by classical means, being a strong example of quantum states. Nevertheless, negativity is not a necessary condition for nonclassicality which means that there are nonclassical states whose Wigner functions are non-negative, but it is a sufficient one. Moreover, negativity of the Wigner function has been identified as a necessary ingredient for implementing processes that cannot be simulated efficiently with classical resources and is therefore an essential resource to achieve quantum advantage (Mari and Eisert, 2012; Albarelli *et al.*, 2018).

2.1.2 Gaussian States and the Covariance Matrix

Gaussian states are the most common states available in the laboratory. Most states with a positive Wigner function, including pure and entangled states, are often Gaussian states. They have that name due to the fact that their Wigner function is Gaussian. One example is the Wigner function of a single mode displaced position-squeezed vacuum state $D(\alpha)S(\zeta)\,|0\rangle$:

$$W(x,p) = \frac{2}{\pi}\exp\left[-2\mathrm{e}^{+2r}\,(x-x_\alpha)^2 - 2\mathrm{e}^{-2r}\,(p-p_\alpha)^2\right]. \tag{2.9}$$

We may now rewrite it as:

$$W(x,p) = \frac{2}{\pi}\exp\left[-\frac{1}{2}\,(x-x_\alpha, p-p_\alpha)\begin{pmatrix} 4\mathrm{e}^{+2r} & 0 \\ 0 & 4\mathrm{e}^{-2r}\end{pmatrix}\begin{pmatrix} x-x_\alpha \\ p-p_\alpha\end{pmatrix}\right]. \tag{2.10}$$

We may expand this notation to the general case of a multi-mode Gaussian state with N modes and write

$$W(\xi) = \frac{1}{(2\pi)^N\sqrt{\det V^{(N)}}}\exp\left\{-\frac{1}{2}\,(\xi-\xi_0)\left[V^{(N)}\right]^{-1}(\xi-\xi_0)^T\right\}, \tag{2.11}$$

where in the case of equation 2.10: $N=1$, $\xi=(x,p)$, $\xi_0=(x_\alpha,p_\alpha)$,

$$V^{(1)} = \frac{1}{4}\begin{pmatrix} \mathrm{e}^{-2r} & 0 \\ 0 & \mathrm{e}^{+2r}\end{pmatrix} \tag{2.12}$$

is the covariance matrix of the state and may be defined in terms of the quadrature operators as

$$V^{(1)} = \begin{pmatrix} \langle\hat{x}^2\rangle - \langle\hat{x}\rangle^2 & \frac{1}{2}\langle\hat{x}\hat{p}+\hat{p}\hat{x}\rangle - \langle\hat{p}\rangle\langle\hat{x}\rangle \\ \frac{1}{2}\langle\hat{x}\hat{p}+\hat{p}\hat{x}\rangle - \langle\hat{p}\rangle\langle\hat{x}\rangle & \langle\hat{p}^2\rangle - \langle\hat{p}\rangle^2\end{pmatrix}. \tag{2.13}$$

For the more general case we write $\xi = (x_1,p_1,x_2,p_2,\ldots,x_N,p_N)$ and $\hat{\xi} = (\hat{x}_1,\hat{p}_1,\hat{x}_2,\hat{p}_2,\ldots,\hat{x}_N,\hat{p}_N)$, such that the first moments are given by $\xi_0 = (\langle\hat{x}_1\rangle,\langle\hat{p}_1\rangle,\langle\hat{x}_2\rangle,\langle\hat{p}_2\rangle,\ldots,\langle\hat{x}_N\rangle,\langle\hat{p}_N\rangle)$. We may now express the general form of the covariance matrix as $V_{ij}^{(N)} = \langle(\hat{\xi}_i\hat{\xi}_j + \hat{\xi}_j\hat{\xi}_i)/2\rangle - \langle\hat{\xi}_i\rangle\langle\hat{\xi}_j\rangle$.

However, most of the time we are interested in properties involving multiple modes, like entanglement. These properties are often independent of the first moments, since these can be locally adjusted with displacements in phase-space. This allows us to disregard the first moments and define the correlation matrix as

$$\begin{aligned} \mathrm{Tr}\left[\hat{\rho}\left(\Delta\hat{\xi}_i\,\Delta\hat{\xi}_j + \Delta\hat{\xi}_j\,\Delta\hat{\xi}_i\right)\right] &= \left\langle\left(\hat{\xi}_i\hat{\xi}_j + \hat{\xi}_j\hat{\xi}_i\right)/2\right\rangle \\ &= \int W(\xi)\,\xi_i\,\xi_j\,\mathrm{d}^{2N}\xi \equiv V_{ij}^{N}, \end{aligned} \tag{2.14}$$

where $\Delta\hat{\xi}_i = \hat{\xi}_i - \langle\hat{\xi}_i\rangle \equiv \hat{\xi}_i$, for zero first moments, and we have used the so-called Weyl correspondence to be able to calculate the expectation value of the operator $S(\hat{x}^n\hat{p}^m)$ in the classical way:

$$\mathrm{Tr}[\hat{\rho}S(\hat{x}^n\hat{p}^m)] = \int W(x,p)x^n\,p^m\,\mathrm{d}x\,\mathrm{d}p. \tag{2.15}$$

When considering Gaussian states with zero mean and in the form of equation 2.11, we may say that the Wigner function of such states is completely determined by their second moment correlation matrix. For physical states the correlation function must be real, symmetric and positive and must obey the commutation relation

$$\left[\hat{\xi}_k,\hat{\xi}_l\right] = \frac{i}{2}\Lambda_{kl}, \qquad k,l = 1,2,3,\ldots,2N, \tag{2.16}$$

where Λ is a block diagonal symplectic matrix that contains the J matrix as its diagonal entries such that

$$\Lambda = \bigoplus_{k=1}^{N} J, \qquad J = \begin{pmatrix} 0 & 1 \\ -1 & 0 \end{pmatrix}. \tag{2.17}$$

We then arrive at the N-mode uncertainty relation

$$V^{(N)} + \frac{i}{4}\Lambda \geq 0, \tag{2.18}$$

which is a necessary condition on a physical state.

2.2 Optical Cavities

Optical cavities, or optical resonators, basically consist in an arrangement of mirrors that confine light with interference (Siegman, 1986). These can be used for many different purposes such as build up power in a gain medium providing feedback for lasers to oscillate; as a reference for the frequency of light, since the resonance frequency mostly depends on the optical path for one round trip; as a way to select spatial modes of light (mode cleaner); and many others. This is an essential device in many quantum optics experiments and and specially true for our experiment, as it will become clear throughout the text.

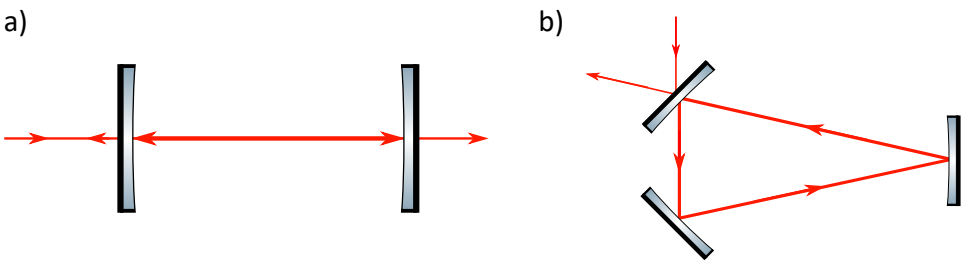

Figure 2.1: a) Linear cavity leading to a standing wave. b) Triangular cavity leading to a travelling wave.

For convenience in our description we divide optical cavities roughly in two types when considering near resonant light being injected: standing wave cavities and travelling wave cavities. In the

standing wave cavity (figure 2.1.a) the field enters the cavity after being transmitted through the first mirror and is reflected on the second mirror, propagating in the opposite direction. The two counter-propagating beams interfere forming a standing wave inside the resonator. In the travelling wave cavity (figure 2.1.b), the intracavity beam after one round trip will add up with the incoming beam, building up after each interaction, forming a single beam propagating forward.

The resonance condition for the light entering a cavity is that its wavelength must be an integer multiple of the perimeter of the cavity, disregarding the phase effects of the reflection on the mirrors. So the resonance frequencies for a cavity with a fixed perimeter p is given by:

$$\nu_{\text{cav}} = \frac{j\,c}{p}, \quad j = \text{integer} \tag{2.19}$$

and c is the speed of light. Resonance frequencies are evenly spaced and the difference between two consecutive resonances is called Free Spectral Range or FSR for short. Another important property of an optical resonator is its linewidth Γ. The resonance frequency is not the only frequency allowed through the cavity, a range of nearby frequencies are also allowed to propagate, however with less intensity. The linewidth of a cavity determines how wide is this range of frequencies and is associated with the time the intracavity field takes to decay after the incident beam is turned off. Both the FSR and the linewidth are depicted in figure 2.2.

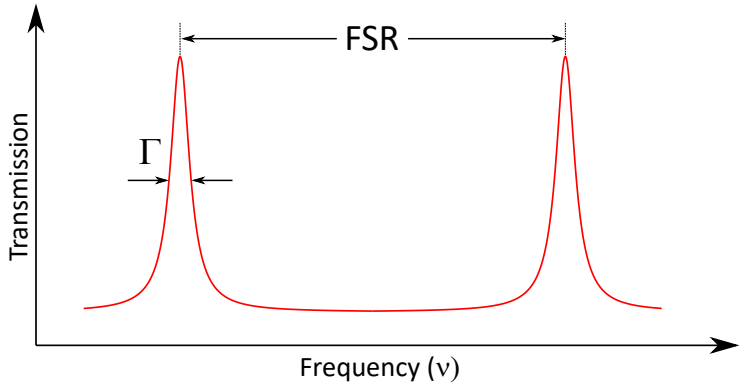

Figure 2.2: FSR and the linewidth Γ when measuring the transmission from the cavity with fixed perimeter and scanning the frequency of the incident beam.

To begin our description of an optical cavity we shall consider the simple example of a linear cavity with input mirror M_1 and output mirror M_2 separated by a distance d_{12}, such that the perimeter is given by $p = 2d_{12}$, as in figure 2.3. Call T_1 and T_2 the transmission coefficients of mirrors M_1 and M_2 respectively and R_1 and R_2 their respective reflectivities. We also model any intracavity losses by defining the coefficient β such that the intensity losses after one round trip are given by $\exp(-\beta p)$. So, after each round trip the amplitude of the intracavity field is attenuated by

$$g_m = \sqrt{R_1 R_2 \exp(-\beta p)}, \tag{2.20}$$

and the field also picks up a phase

$$\delta\phi = 2\pi(\nu_L - \nu_{\text{cav}})\frac{p}{c}, \tag{2.21}$$

where ν_L is the frequency of the incident light. We can then describe the total effect of the cavity after one round trip by the complex number

$$g(\nu) = g_m \exp\left(-i\delta\phi(\nu)\right). \tag{2.22}$$

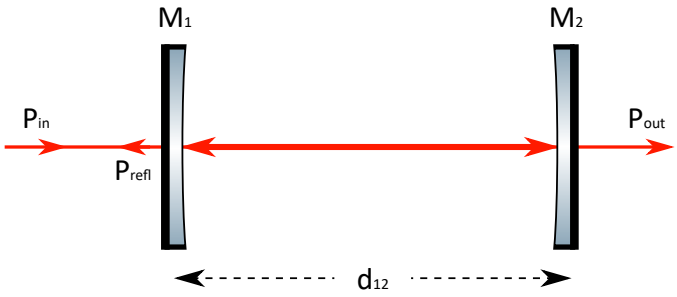

Figure 2.3: Linear cavity with perimeter $p = 2d_{12}$. The mirrors M_1 and M_2 have transmissivities T_1 and T_2 and reflectivities R_1 and R_2 respectively.

When the incoming field with amplitude α_{in} hits the cavity it gets partially transmitted and only the amount $\alpha_0 = \sqrt{T_1}\alpha_{in}$ is allowed through the mirror M_1. After one round trip the intracavity field will be $\alpha_0 + \alpha_1$, after two round trips $\alpha_0 + \alpha_1 + \alpha_2$, and so on, such that $\alpha_{\text{cav}} = \sum_j \alpha_j$. Given that we can model $\alpha_{j+1} = g(\nu)\alpha_j$, and assuming $j \to \infty$, we arrive at the following compact expression for the amplitude of the intracavity field (Bachor and Ralph, 2019):

$$\alpha_{\text{cav}} = \frac{\alpha_0}{1 - g(\nu)}. \tag{2.23}$$

The intracavity power is then, after some calculations, given by

$$P_{\text{cav}} \propto |\alpha_{\text{cav}}|^2 = P_{\max} \frac{1}{1 + (2F/\pi)^2 \sin^2(\delta\phi/2)}, \tag{2.24}$$

where $P_{\max}$ refers to the maximum intracavity power, which occurs when the frequency of the incoming beam is in resonance with the cavity, and is given by

$$P_{\max} = \left(\frac{\alpha_0}{1 - g_m}\right)^2, \tag{2.25}$$

and

$$F = \frac{\pi\sqrt{g_m}}{(1 - g_m)} \tag{2.26}$$

is an important property called Finesse, commonly used as a measure of the quality of a cavity. The Finesse is usually defined as the free spectral range divided by the linewidth of the cavity (FSR/Γ) and as it can be seen from equation 2.26, it can be fully determined by the resonator losses (g_m).

We can have better insight about the effects of the cavity over the incoming field by looking at the input and output relations for a given loss coefficient β:

$$\begin{aligned} \alpha_0 &= \sqrt{T_1}\alpha_{\text{in}} \\ \alpha_{\text{out}} &= \sqrt{T_2}\exp(-\beta d_{12} + i\delta\phi/2)\alpha_{\text{cav}} \\ \alpha_{\text{refl}} &= -\sqrt{R_1}\alpha_{\text{in}} + \sqrt{T_1}\alpha_{\text{cav}} \end{aligned} \tag{2.27}$$

where α_{out} refers to the field exiting the cavity and takes into account the transmission on the second mirror as well as the losses and the phase added in the last path d_{12}. α_{refl} refers to field reflected from the first mirror plus the field transmitted back from the cavity through the mirror M_1. So the output,

reflected and intracavity powers normalized by the incoming power are

$$\begin{aligned}\frac{P_{\text{out}}}{P_{\text{in}}} &= T_1 T_2 \frac{\exp(-2\beta d_{12})}{|1-g(\nu)|^2} \\ \frac{P_{\text{refl}}}{P_{\text{in}}} &= \frac{|R_1-(R_1+T_1)g(\nu)|^2}{R_1\,|1-g(\nu)|^2} \\ \frac{P_{\text{cav}}}{P_{\text{in}}} &= \frac{T_1}{|1-g(\nu)|^2}.\end{aligned} \tag{2.28}$$

When considering losses inside a cavity, there is an interesting configuration where the transmission T_1 is made to balance these losses. In such configuration, the reflectivity $R_1 = R_2\exp(-\beta p)$ makes the reflected power of the input mirror exactly match the leakage of intracavity power from the same mirror, such that both fields cancel each other out. This is known, much like in the electronic case, as impedance matching, and in this case the transmission from the cavity is optimized. When this condition is obeyed the optical cavity is impedance matched. The other two scenarios are the under-coupled, where $R_1 < R_2\exp(-\beta p)$ and the over-coupled, where $R_1 > R_2\exp(-\beta p)$. The last two cases lead to some reflection and sub-optimal transmission.

The changes in the incoming field introduced by the cavity are not restricted to its amplitude. Phase shifts will also be added with important consequences to the sidebands of the incoming beam. We take advantage of this effect in our detection scheme through the resonator detection technique (Villar, 2008; Barbosa *et al.*, 2013), which will be discussed in the following section. We shall leave the formal treatment of the phase response of the cavity for then.

Another important characteristic for the resonance of the beam inside the cavity, and therefore building up intracavity power, is the shape of the wavefront. Ideally, the curvature of the wavefront of the spacial modes of the incoming light should match the curvature of the mirrors, but even when this is not the case, it is possible to have resonance inside the cavity. For the simple case of the linear cavity (Kogelnik and Li, 1966) in figure 2.3 let us say that mirrors M_1 and M_2 have focal lengths f_1 and f_2 respectively.

We now define their parameters

$$g_1 = 1-\frac{d_{12}}{2f_1} \quad \text{and} \quad g_2 = 1-\frac{d_{12}}{2f_2}. \tag{2.29}$$

An optical resonator will build up a resonant wave when the condition

$$0 \le g_1 g_2 \le 1 \tag{2.30}$$

is obeyed. A cavity that obeys this condition is said to be stable and we usually call equation 2.30 the cavity stability condition. Many configurations of mirrors form stable cavities. The allowed combinations of g_1 and g_2 are represented by the blue area in figure 2.4, along with some of the more common types of resonators.

But simply obeying the stability condition 2.30 is not enough. If the wavefront of the incoming beam does not match the internal wavefront, the cavity will support not only a fundamental mode, but a series of higher order modes. These can be seen as smaller transmission peaks by scanning the frequency of the incoming beam around the cavity's resonance frequency. Usually it is desirable that only a fundamental mode propagates inside an optical resonator and we must, in this case, match the incoming and the intracavity wavefronts. To do that, in practice, we shape the wavefront of the incoming beam by using optical components, such as lenses, to match the intracavity wavefront. We call this laborious task *mode matching*.

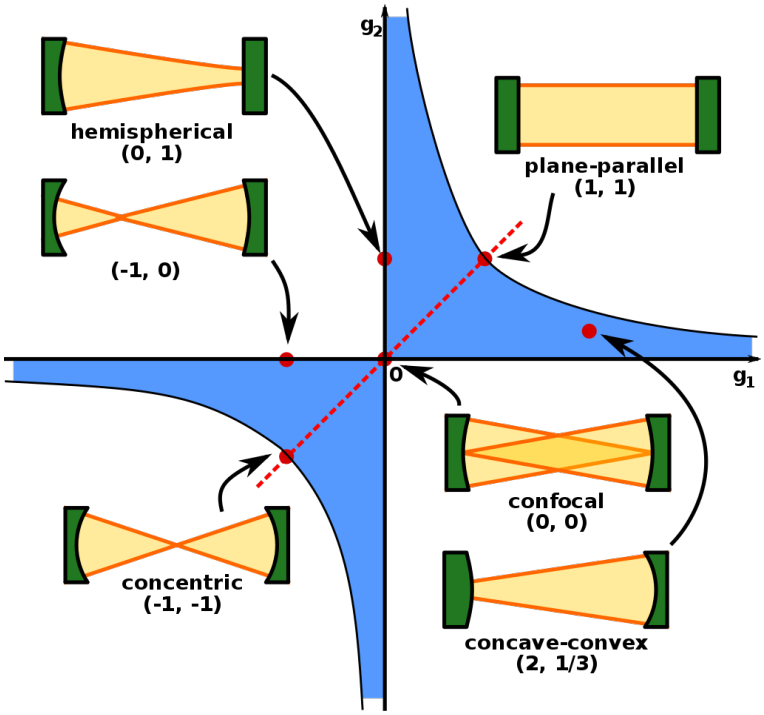

Figure 2.4: Combinations of g_1 and g_2. Stable resonators are represented by the blue area along with with their values for some of the more common types of resonators. *Reprinted from Wikipedia.*

2.3 Detection Theory

Although we use photodetectors in the laboratory, we are not detecting and analyzing individual photons. This is because in our experiments we work with intense beams ($\sim 10^{16}$ photons/s), which means an intense photon flux, and with current technology photodetectors are simply not fast enough to detect them individually. Also, because our photodetectors convert the detected photon flux into an electric signal and this is the signal we analyze.

Photon detection theory is the bridge that allows us to connect the statistics of the electric signals we have available to analyze and the statistics of the photon flux in our beam. By characterizing the statistics of the photons arriving at the detector we can obtain information about the nature of the incoming beam. A coherent state of light (a good laser source) has a Poisson distribution, a natural source of light (or a noisy laser) has a thermal distribution, non-classical states of light (squeezed light) have sub-Poissonian distributions, and so on.

Photodetectors come in different flavors, but given that in our experiment our detectors consist of photodiodes, we are interested in describing the ones that take advantage of the photoelectric effect to generate a photocurrent. Since we are dealing with intense beams, the signal from the photodetector is integrated for a time Δt over a number of photoelectrons $n_e(t)$ and this number is proportional to the power of the incoming beam $P(t)$. Hence, the photocurrent $i(t)$ generated can be expressed as (Bachor and Ralph, 2019)

$$i(t) = \frac{n_e(t)\, e}{\Delta t} = \frac{P(t)\, e\, \eta_{\text{det}}}{h\nu}, \tag{2.31}$$

where e is elementary charge and η_{det} the efficiency of the detector. It is usual to describe the photocurrent as an average current $\langle i(t) \rangle$ (DC current) with some fluctuations $\delta i(t)$ around this value (AC current) such that

$$i(t) = \langle i(t) \rangle + \delta i(t). \tag{2.32}$$

We can analyze the fluctuations $\delta i(t)$ of the photocurrent to obtain information about the noise and the signal carried by the incident beam. The relevant quantity we are interested for a quantitative description of these fluctuations is the variance

$$\Delta i(t)^2 = \Delta\left(\frac{n_e(t)\,e}{\Delta t}\right)^2 = \frac{\Delta(n_e(t))^2\,e^2}{\Delta t^2}. \tag{2.33}$$

For a detector with high quantum efficiency, the photoelectron statistics should mirror the photon statistics of the incident beam. Given that the latter has a Poisson distribution, assuming a sufficiently high quantum efficiency, we can say that the variance of photoelectron number is $\Delta(n_e(t))^2 = \langle n_e(t)\rangle = \langle i(t)\rangle \Delta t/e$. So the variance of the photocurrent is

$$\Delta i(t)^2 = \frac{\langle i(t)\rangle\, e}{\Delta t}. \tag{2.34}$$

This is usually referred to as the shotnoise limit and that is the lowest possible value for the variance when considering classical sources light.

Going below the shotnoise limit requires sub-Poissonian photocurrent statistics, in other words squeezed light. However, a detector with low quantum efficiency will randomly select a fraction of the incoming light, bringing the photocurrent variance closer to the shotnoise limit then to the actual variance of the light intensity. In laboratory experiments we can calibrate the quantum efficiency of our detector and correct for it in our analysis, but ideally for better measurements high quantum efficiency detectors are desirable.

2.3.1 Spectral Analysis

We have showed a direct relation between the photocurrent measured in a photodetector and the number of incoming photons. Now we can, in the quantum description, associate a photocurrent operator with the field operators to measure the quantum properties of the incident field. In the following we are going to give an overview of how these relate and how the information obtained allows us to build the covariance matrix of our system, and hence the Wigner function. For a detailed description refer to original works of Villar (2008) and Barbosa *et al.* (2013), and also the review given in Andrade (2018) who addresses this subject drawing attention to the steps taken in the experimental process.

From the canonical quantization (Mandel and Wolf, 1995) we may write the multimode electric field as

$$\hat{E}(\mathbf{r},t) = \sum_{\omega} \varepsilon_\omega \hat{a}_\omega \mathrm{e}^{i(\mathbf{k}\cdot\mathbf{r}-\omega t)} + \mathbf{h.c.}, \tag{2.35}$$

where $[\hat{a}_\omega, \hat{a}^\dagger_{\omega'}] = \delta_{\omega\omega'}$, ε_ω is the polarization of the frequency mode ω, $\mathbf{k}$ is the wave vector and $\mathbf{r}$ the position. Then we define, in the reference frame of the photodetector ($|\mathbf{r}| = 0$), respectively the positive and negative frequency operators $\hat{E}^+(t)$ and $\hat{E}^-(t)$, such that $\hat{E}^+(t) = (\hat{E}^-(t))^\dagger$. In this formalism, the mean value of the photocurrent operator is given by (Glauber, 1963)

$$\langle \hat{I}(t)\rangle = \langle \hat{E}^-(t)\hat{E}^+(t)\rangle. \tag{2.36}$$

We can separate the state of the incoming beam in two parts: a carrier with a well defined intense coherent mode $|\alpha_{\omega_0}\rangle$, that can be seen as a classical mode, and a continuum of quantum modes $|\psi\rangle$ that can be singled out by demodulating at a specific analysis frequency Ω (sideband modes). The mean value of the photocurrent operator in this framework can now be calculated:

$$\begin{aligned} \langle \hat{I}(t)\rangle &= \langle\psi|\,\langle\alpha_{\omega_0}|\,\hat{E}^-(t)\hat{E}^+(t)\,|\alpha_{\omega_0}\rangle\,|\psi\rangle \\ &= |\alpha_{\omega_0}|^2 + |\alpha_{\omega_0}|\,\langle\delta\hat{I}_\theta(t)\rangle\,, \quad \alpha_{\omega_0} = |\alpha_{\omega_0}|\mathrm{e}^{i\theta} \end{aligned} \tag{2.37}$$

such that the complex number α_{ω_0} is the eigenvalue of the annilation operator for the mode ω_0 of the carrier. We can see from equation 2.37 that much like in equation 2.32 we can separate the photocurrent in a strong classical signal plus a fluctuation term.

It is interesting to note that the term $\langle \delta\hat{I}_\theta(t) \rangle$ in equation 2.37 is associated with the fluctuations in the sidebands and that it is amplified by the amplitude of the carrier. The expression for the operator $\delta\hat{I}_\theta(t)$ is given by $\delta\hat{I}_\theta(t) = \mathrm{e}^{-i\theta}\hat{a}(t) + \mathrm{e}^{i\theta}\hat{a}^\dagger(t)$ and we can write the annihilation and creation operators as:

$$\hat{a}(t) = \int_0^{'\infty} d\omega\, \mathrm{e}^{-i(\omega-\omega_0)t}\, \hat{a}_\omega \quad \text{and} \quad \hat{a}^\dagger(t) = \int_0^{'\infty} d\omega\, \mathrm{e}^{i(\omega-\omega_0)t}\, \hat{a}^\dagger_\omega, \tag{2.38}$$

where the prime on the integral sign denotes that the integrals are performed over all frequency modes with the exception of the carrier frequency ($\omega \neq \omega_0$).

The Fourier transform of the photocurrent fluctuation operator $\delta\hat{I}_\theta(t)$ gives us information about its components in the frequency domain

$$\hat{I}_\Omega = \int \delta\hat{I}_\theta(t)\, \mathrm{e}^{i\Omega t}\, dt, \tag{2.39}$$

where the limits of integration depend on the bandwidth of the detector. For any given analysis frequency Ω this calculation results in spectral components at the frequencies $\omega_0 + \Omega$ and $\omega_0 - \Omega$, regarding respectively the bosonic operators of the upper and lower sidebands $\hat{a}_u$ and $\hat{a}_l$, such that

$$\hat{I}_\Omega = \mathrm{e}^{-i\theta}\hat{a}_u + \mathrm{e}^{i\theta}\hat{a}^\dagger_l. \tag{2.40}$$

Since this analysis of the photocurrent involves two different frequency modes, we need to implement a detection system capable of detecting them separately.

The representation of the photocurrent operator as a complex quantity allows us to express it as real and imaginary parts: $\hat{I}_\Omega = (\hat{I}_{\cos} + i\,\hat{I}_{\sin})/\sqrt{2}$. If we introduce a pair of quadrature operators $\hat{p}_\omega$ and $\hat{q}_\omega$ such that $[\hat{p}_\omega, \hat{q}_{\omega'}] = 2i\delta(\omega - \omega')$, writing $\hat{a}_\omega = (\hat{p}_\omega + i\,\hat{q}_\omega)/2$, $\hat{a}^\dagger_\omega = (\hat{p}_\omega - i\,\hat{q}_\omega)/2$, and noting that $\hat{I}^\dagger_\Omega = \hat{I}_{-\Omega}$, we may express those parts as

$$\hat{I}_{\cos} = \cos\theta\, \frac{\hat{p}_u + \hat{p}_l}{\sqrt{2}} + \sin\theta\, \frac{\hat{q}_u + \hat{q}_l}{\sqrt{2}}, \tag{2.41}$$

$$\hat{I}_{\sin} = \cos\theta\, \frac{\hat{q}_u - \hat{q}_l}{\sqrt{2}} - \sin\theta\, \frac{\hat{p}_u - \hat{p}_l}{\sqrt{2}}. \tag{2.42}$$

We can simultaneously measure $\hat{I}_{\cos}$ and $\hat{I}_{\sin}$ by splitting the photocurrent in two and mixing each part with electronic oscillators in quadrature as shown in figure 2.5.

We can now obtain the power spectral density $S(\Omega)$ for the photocurrent by taking into account the Wiener-Kintchine theorem, that allows us to relate $S(\Omega)$ with the autocorrelation function for a stationary process $\langle \hat{I}_\Omega \hat{I}_{-\Omega} \rangle$. In this case, this implies in

$$\begin{aligned} S(\Omega) &= \langle \hat{I}_\Omega \hat{I}_{-\Omega} \rangle\,, \\ \langle \hat{I}_\Omega \hat{I}_{\Omega'} \rangle &= 0, \quad \forall \quad \Omega' \neq -\Omega. \end{aligned} \tag{2.43}$$

When the photocurrent obeys equation 2.43 it is said to be in a stationary quantum state (Barbosa *et al.*, 2013). And its evaluation from the components of $\hat{I}_\Omega$ yields

$$S(\Omega) = \frac{1}{2}\langle \hat{I}^2_{\cos} \rangle + \frac{1}{2}\langle \hat{I}^2_{\sin} \rangle\,. \tag{2.44}$$

Also, this condition allows us to extract information from our system, since:

$$\langle \hat{I}_\Omega \hat{I}_\Omega \rangle = 0 \quad \Longrightarrow \quad \begin{cases} \Delta^2 \hat{I}_{\cos} - \Delta^2 \hat{I}_{\sin} = 0, \\ \langle \hat{I}_{\cos} \hat{I}_{\sin} \rangle = 0. \end{cases} \tag{2.45}$$

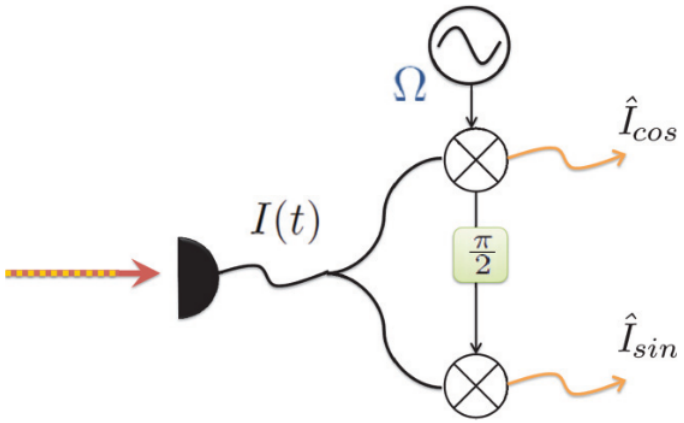

Figure 2.5: Scheme for the simultaneous measurement of the real ($\hat{I}_{\cos}$) and imaginary ($\hat{I}_{\sin}$) parts of the photocurrent operator. *Reprinted from* Barbosa *et al.* (2013).

2.3.2 Resonator detection: Rotation of the Noise Ellipse

Now, everything we mentioned so far involves how we draw information from the amplitude of the field and this is intimately associated with the nature of our photodetectors. They cannot, in principle, give information about the phase of the incoming light. However, to be able to characterize our quantum system, we need that phase information. One clever way to work around these limitations is to convert phase fluctuations into amplitude fluctuations, that can then be recorded by the photodetector (Galatola *et al.*, 1991).

The most common technique used for this purpose is called homodyne detection, and it uses an intense laser with a well defined phase, called local oscillator, that will interfere with the laser that we want to analyse. By tuning the phase of the local oscillator it is possible to convert phase fluctuations into amplitude fluctuations that can now be picked up by our photodetectors. This is a well known technique and its description can be found in most quantum optics books (Scully and Zubairy, 1997; Bachor and Ralph, 2019), and since we do not use it in our experiment we will not go into further detail about it here.

However, we use a similar method that, as mentioned earlier, takes advantage of an empty optical cavity to make the beam interfere with itself, and by changing the size of the cavity we can obtain interchangeably amplitude and phase information. Since this technique makes the beam interfere with itself, it is sometimes referred to as self-homodyne detection. We have seen a classical treatment for the fields reflected and transmitted from an optical cavity in section 2.2 . The quantum treatment is similar to that, but now we must take into account a vacuum input α_{v} at mirror M_2, as shown in figure 2.6. We are interested in a quantum description of the reflected field α_{refl}.

Let us consider the bosonic operators $\hat{a}_\omega$ for the incident field α_{in} at mirror M_1 and $\hat{b}_\omega$ for the vacuum input α_{v} at mirror M_2. The cavity will transform the annihilation operator as:

$$\hat{a}_\omega \longrightarrow r(\Delta_\omega)\,\hat{a}_\omega + t(\Delta_\omega)\,\hat{b}_\omega, \tag{2.46}$$

where transmission $t(\Delta_\omega)$ and reflection $r(\Delta_\omega)$ coefficients are dependent on the detuning $\Delta_\omega = (\omega - \omega_c)/\Gamma$ between the cavity and the field mode (again Γ is the cavity linewidth). For frequencies close to the resonance, the expression for $r(\Delta_\omega)$ becomes:

$$r(\Delta_\omega) = -\frac{\sqrt{d} + 2i\Delta_\omega}{1 - 2i\Delta_\omega}, \tag{2.47}$$

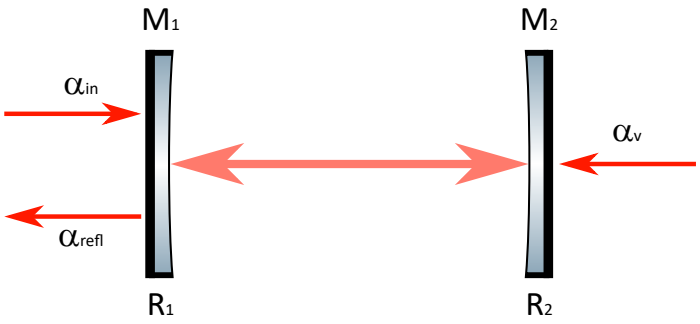

Figure 2.6: Example of a linear cavity for the rotation of the noise ellipse. The incoming field $\alpha_{\rm in}$ gets partially transmitted and partially reflected $\alpha_{\rm refl}$ at mirror M_1. The coupling with vacuum fluctuations $\alpha_{\rm v}$ must be taken in to account at mirror M_2.

where d is the impedance matching parameter, that is associated with the amount of power reflected from the cavity at zero detuning. The value $d = 0$ indicates that the optical cavity is operating in the impedance matched condition.

If we transform the bosonic operators for the upper and lower sidebands in equation 2.40 according to the relation 2.46, we obtain the following expression for the photocurrent operator (Barbosa *et al.*, 2013):

$$\hat{I}_\Omega = R^*_\Omega(\Delta)\,\hat{a}_u + R_{-\Omega}(\Delta)\,\hat{a}^\dagger_l + T^*_\Omega(\Delta)\,\hat{b}_u + T_{-\Omega}(\Delta)\,\hat{b}^\dagger_l, \tag{2.48}$$

where

$$\begin{aligned} R_\Omega(\Delta) &= \frac{1}{\sqrt{2}}\frac{r(\Delta)}{|r(\Delta)|}\,r^*(\Delta+\Omega/\Gamma), \\ T_\Omega(\Delta) &= \frac{1}{\sqrt{2}}\frac{r(\Delta)}{|r(\Delta)|}\,t^*(\Delta+\Omega/\Gamma), \end{aligned} \tag{2.49}$$

and the phase $e^{i\theta}$ is such that $e^{i\theta} = \frac{1}{\sqrt{2}}\frac{r(\Delta)}{|r(\Delta)|}$.

We may write the photocurrent operator in terms of the quadrature components $\hat{I}_{\rm cos}$ and $\hat{I}_{\rm sin}$ as in $\hat{I}_\Omega = (\hat{I}_{\rm cos} + i\,\hat{I}_{\rm sin})/\sqrt{2} + \hat{I}_{\rm vac}$ by introducing the real functions of Δ: $x_\pm$ and $y_\pm$, such that (Barbosa *et al.*, 2013)

$$\begin{aligned} x_+ + i\,y_+ &= (R_\Omega + R^*_{-\Omega})/2 \equiv g_+, \\ x_- + i\,y_- &= i(R_\Omega - R^*_{-\Omega})/2 \equiv g_-. \end{aligned} \tag{2.50}$$

Then, we have:

$$\begin{aligned} \hat{I}_{\rm cos}(\Delta) &= x_+\,\hat{p}_u + y_+\,\hat{q}_u + x_-\,\hat{p}_l - y_-\,\hat{q}_l, \\ \hat{I}_{\rm sin}(\Delta) &= y_-\,\hat{p}_u + x_-\,\hat{q}_u - y_+\,\hat{p}_l + x_+\,\hat{q}_l, \end{aligned} \tag{2.51}$$

where it is important to note that $\hat{I}_{\rm cos}$ and $\hat{I}_{\rm sin}$ commute, since they are independent observables. The power spectral density of the photocurrent can now be obtained from equations 2.51 and 2.44, resulting in

$$S(\Delta) = \frac{1}{2}\Delta^2\hat{I}_{\rm cos} + \frac{1}{2}\Delta^2\hat{I}_{\rm sin} + \frac{1}{2}\Delta^2\hat{I}_{\rm vac}, \tag{2.52}$$

where $\Delta^2\hat{I}_{\rm vac}$ is the variance of vacuum fluctuations.

Ultimately, we are interested in reconstructing the covariance matrix of our system. So, if we look at equations 2.41 and 2.42 as written in a basis of symmetric and antisymmetric combinations of the sideband operators

$$\hat{p}_{s(a)} = \frac{\hat{p}_u \pm \hat{p}_l}{\sqrt{2}} \quad \text{and} \quad \hat{q}_{s(a)} = \frac{\hat{q}_u \pm \hat{q}_l}{\sqrt{2}}, \tag{2.53}$$

we may write

$$\hat{I}_{\cos} = \cos\theta\ \hat{p}_s + \sin\theta\ \hat{q}_s \equiv \hat{X}_s^{\theta}, \tag{2.54}$$

$$\hat{I}_{\sin} = \cos\theta\ \hat{q}_a - \sin\theta\ \hat{p}_a \equiv \hat{X}_a^{\theta+\frac{\pi}{2}}. \tag{2.55}$$

and the stationarity condition 2.45 yields:

$$\langle \hat{I}_\Omega \hat{I}_\Omega \rangle = 0 \quad \Longrightarrow \quad \begin{cases} \Delta^2 \hat{X}_s^{\theta} = \Delta^2 \hat{X}_a^{\theta+\frac{\pi}{2}}, \\ \langle \Delta^2 \hat{X}_s^{\theta}\ \Delta^2 \hat{X}_a^{\theta+\frac{\pi}{2}} \rangle = 0. \end{cases} \tag{2.56}$$

which leads to the conclusion that, in the case of a stationary quantum state, the noise power corresponds to the variance of a field quadrature (Barbosa *et al.*, 2013).

The covariance matrix represented in the basis of symmetric and antisymmetric modes 2.53, and considering condition 2.56, assumes the symmetric form

$$\mathbf{V}_{(s/a)} = \begin{pmatrix} \alpha & \gamma & \delta & 0 \\ \gamma & \beta & 0 & \delta \\ \delta & 0 & \beta & -\gamma \\ 0 & \delta & -\gamma & \alpha \end{pmatrix} \equiv \begin{pmatrix} \mathbf{V}_s & \mathbf{C}_{(s/a)} \\ (\mathbf{C}_{(s/a)})^T & \mathbf{V}_a \end{pmatrix}, \tag{2.57}$$

where we define $\vec{\mathbf{X}}_{s(a)} = (\hat{p}_{s(a)}\, \hat{q}_{s(a)})^T$ to obtain the covariance matrices $\mathbf{V}_{s(a)} = \langle \vec{\mathbf{X}}_{s(a)} \cdot \vec{\mathbf{X}}_{s(a)}^T \rangle$ and the correlation matrix $\mathbf{C}_{(s/a)} = \langle \vec{\mathbf{X}}_s \cdot \vec{\mathbf{X}}_a^T \rangle$.

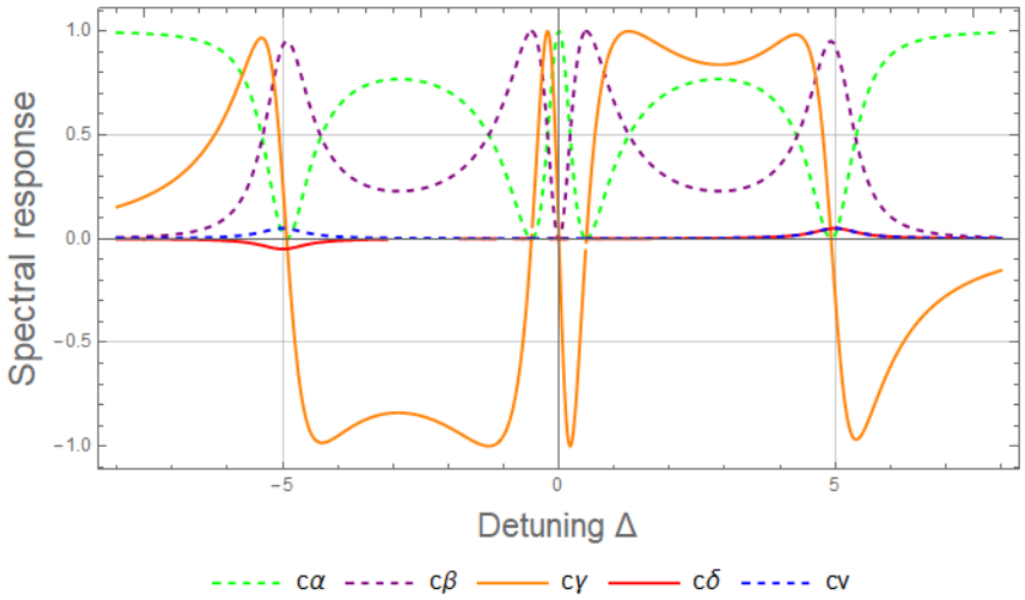

Figure 2.7: Individual plot for the coefficients in equation 2.58 as a function of the cavity detuning Δ for the arbitrary parameters $d = 0.9$ and $\Omega = 5$.

We now finally write the spectral quantum noise for the resonator detection 2.52 in terms of the elements of the covariance matrix 2.57 as (Barbosa *et al.*, 2013):

$$S_{RD}(\Delta) = c_\alpha\ \alpha + c_\beta\ \beta + c_\gamma\ \gamma + c_\delta\ \delta + c_v, \tag{2.58}$$

where we express the coefficients in terms of the functions of Δ in equations 2.50 as: $c_\alpha = |g_+|^2$, $c_\beta = |g_-|^2$, $c_\gamma + i\, c_\delta = 2 g_+^*\, g_-$ and $c_v = 1 - c_\alpha - c_\beta$. As stated earlier in section 2.1.2, this information reveals the second moment correlation matrix, allowing us to reconstruct our Gaussian state. The individual behaviour of the coefficients in equation 2.58 as a function of the cavity detuning Δ are displayed in figure 2.7. The phase rotation of the noise ellipse obtained from equation 2.58 is shown in figure 2.8.

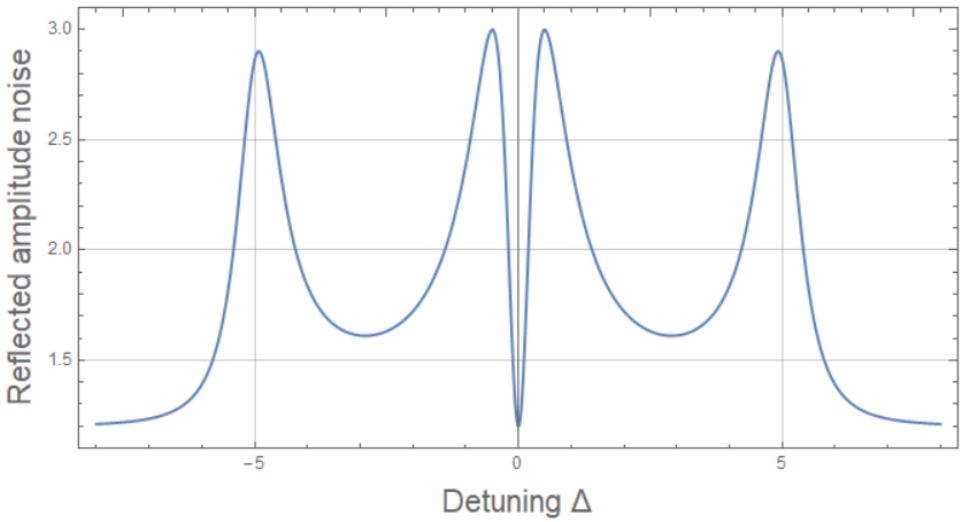

Figure 2.8: Example of the rotation of the noise ellipse in phase space as described by equation 2.58.

We can now take a closer look at the correspondence of the detected signal as a function of the cavity detuning and the rotation of the noise ellipse in phase space. Suppose the incoming beam is squeezed in the amplitude quadrature. If the detuning is large, frame 1 of figure 2.9 shows that the cavity has no effect and we measure amplitude noise. As the relative detuning of the first sideband gets closer to resonance, the noise ellipse rotates until a full $\pi/2$ rotation in frame 3 and conversion of amplitude to phase fluctuation is observed. Between frames 6 and 12, the carrier gets close to resonance and experiences two complete conversions between quadratures. As the carrier moves away from resonance and the second sideband gets closer to it the noise ellipse rotates again converting amplitude to phase and back to amplitude again between frames 13 and 17.

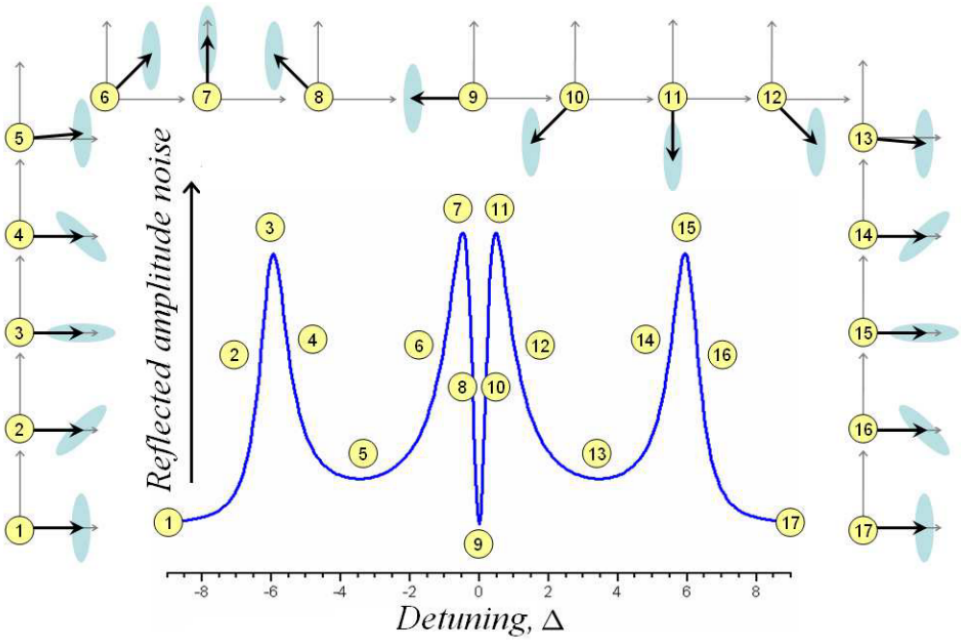

Figure 2.9: Rotation of the noise ellipse in phase space and its correspondence with the amplitude signal as a function of the detuning Δ. *Reprinted from* Villar (2008).

The tools developed in this chapter for the investigation of optical fields pave the basis for the

understanding of the techniques presented throughout this thesis. For instance, optical cavities are widely used in our experiments, from the laser cavities, to frequency stabilization and detection schemes. Also, the resonator detection technique allows us to build the correlation matrix for the fields being detected. Given the correspondence between the Wigner function and the correlation matrix this result is essentially a tomography of the quantum system, providing us with an important tool for the characterization of the quantum states generated in the OPO. In the following parts of this work we will often refer to the formalism introduced in this section.

In the next part we describe the OPO and its importance in the generation of the entangled fields we are interested in. We also provide an experimental description of the scheme we use to generate and characterize these fields and discuss our measurements of their quadratures and correlations.

Part II

Generation of Entangled States of Light

3 INTRODUCTION

Here we present the information regarding the generation of tripartite entanglement in our optical parametric oscillator (OPO). The experiment portrayed here was performed at the Laboratory for Coherent Manipulation of Atoms and Light (LMCAL) at the Physics Intitute of the University of São Paulo as part, and as consequence, of the work by Andrade (2018).

Entanglement is an essential resource for the transmission of information between different components of a system. This shared information allows the implementation of computational processes based on the manipulation of quantum information, improving the efficiency of some systems when compared to a process based on the classical binary logic (Nielsen and Chuang, 2010). The idea behind the experiment is to use an OPO to generate entangled light at different wavelengths. Then use this entanglement to implement quantum information protocols between systems that would not interact with each other under normal circumstances because they have different natural frequencies. Ultimately, we would like to establish the basis for a quantum network (Kimble, 2008).

The output of the OPO presented here consists of three beams: the reflected pump with a wavelength resonant with the Rubidium D2 transition line, at around 780 nm, and a pair of twin beams called signal and idler with wavelengths at around 1560 nm, compatible with the C-band of telecommunication's channels. As stated earlier, the key property of interest to us, shared by the three beams, is entanglement. However, as we will see in the following chapters, entanglement is very sensitive to perturbations in the system and, when these perturbations are not properly controlled, it can be degraded to the point where quantum information protocols, such as teleportation, cannot be implemented with an efficiency that is better that their classical equivalent.

We realized that the main source of noise, responsible for degrading the entanglement between the three beams in our system, is the extra phase noise added due to the coupling of the fields with thermal vibrations (phonons) in the crystal lattice. For this reason we put a lot of work in controlling the crystal temperature and lowering it to acceptable levels.

This part of the thesis is structured as follows: We begin with the classical and quantum descriptions of the OPO in Chapter 4, followed by a model that includes the coupling with phonon noise in the quantum treatment. The chapter proceeds with the theory of quantum correlations such as squeezing and entanglement and ends an overview of the teleportation protocol. In chapter 5 we explain our experiment starting with the pump laser, followed by the OPO and the detection system. Chapter 6 contains the results from our measurements. In chapter 7 we discuss our results and comment on the next steps.

4 THEORETICAL DESCRIPTION

In this chapter we introduce the theory behind the parametric process that generates the output fields from the OPO and how this process creates non-classical correlations between them. These correlations, together with the possibility of having them on fields with distinct wavelengths, allow this system to be used in many quantum information protocols and, consequently, present it as a promising technology for the development of quantum networks.

4.1 Optical Parametric Oscillator

We will divide our description of the OPO in two parts. First we will give a classical treatment for the fields inside an optical cavity that contains a non-linear crystal as described by Debuisschert *et al.* (1993), which gives relevant insight on the oscillation conditions for the OPO and the populated modes for the electromagnetic fields. Then we proceed to the quantum description which will allow us to describe the squeezing (Fabre *et al.*, 1990) and the quantum correlations between the output field modes (Martinelli *et al.*, 2001).

4.1.1 Classical Description

In this work we will focus only on the discussion of a type-II phase matching OPO since this is the type of phase matching present in our crystal. In this case, the polarization modes for the downconverted fields, signal and idler, are orthogonal. For information on type-I phase matching OPOs we recomend the work of Eckardt *et al.* (1991).

As hinted earlier, an OPO consists of an optical cavity with a non-linear medium inside it that is responsible for converting a photon of an incoming field mode with frequency ω_0, that we call pump, into a pair of photons of frequencies ω_1 and ω_2, that we call signal and idler. Since this is a parametric process, energy conservation is obeyed and $\omega_0 = \omega_1 + \omega_2$. As a consequence of the annihilation of a pump photon and the simultaneous creation of photons in the signal and idler modes, we expect correlations in intensity between the three modes. We also expect phase correlations, given that the sum of the phases of signal and idler is locked to the phase of the pump for the same reason.

We can take into account three different regimes of operation for OPOs that differ with respect to the number of resonant fields inside the cavity. When only the signal is resonant we call it a single resonant OPO (SROPO). When signal and idler are resonant we have a doubly resonant OPO. When the three fields are resonant we have a triply resonant OPO (TROPO), which has the advantage of a lower oscillation threshold since the pump intensity on the crystal will increase due to the multiple round trips of the pump. The latter is the configuration of our OPO and the one that will be considered throughout this work.

For simplicity, let us consider an OPO formed by a triangular traveling wave cavity and a nonlinear crystal of length l as depicted in figure 4.1. We define the total length of the cavity as $L_{\text{cav}} = L + l$, where L is the length of the empty part of the cavity. The mirrors that form this cavity are taken to be perfectly reflective ($R = 1$), with the exception of the coupling mirror, which is the only one that allows partial transmission t_0, t_1 and t_2 of the fields α_0, α_1 and α_2 and has reflection coefficients r_0, r_1 and r_2 for each of them. We shall consider that the transmission coefficients are small such that

$$\begin{aligned} r_j &= \mathrm{e}^{-\gamma_j} \simeq 1 - \gamma_j, \\ t_j &= \sqrt{2\gamma_j}, \end{aligned} \tag{4.1}$$

where $j = 0, 1, 2$ and $\gamma_j \ll 1$ was used for the first order approximation.

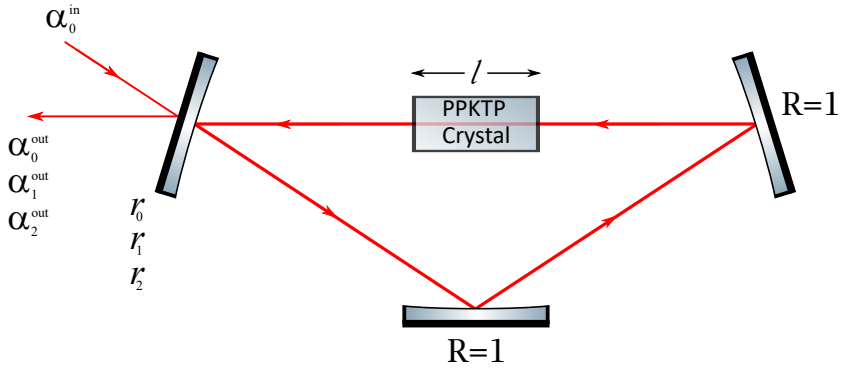

Figure 4.1: Example of a traveling wave cavity OPO.

The propagation equations for the electromagnetic field inside the cavity considering the slow varying envelope method (Debuisschert *et al.*, 1993) allow us to obtain an expression for the change of the fields along the optical axis z:

$$\begin{aligned} \frac{d\alpha_0}{dz} &= -2\chi^*_{\text{eff}}\,\alpha_2(z)\,\alpha_1(z)\,\mathrm{e}^{-i\,\Delta k\,z}, \\ \frac{d\alpha_1}{dz} &= 2\chi_{\text{eff}}\,\alpha_0(z)\,\alpha_2^*(z)\,\mathrm{e}^{i\,\Delta k\,z}, \\ \frac{d\alpha_2}{dz} &= 2\chi_{\text{eff}}\,\alpha_0(z)\,\alpha_1^*(z)\,\mathrm{e}^{i\,\Delta k\,z}, \end{aligned} \tag{4.2}$$

where $\Delta k = k_0 - k_1 - k_2$ is the mismatch between the wave vectors k_0, k_1 and k_2 of the fields. χ_{eff} depends on the beam waist for each field inside the crystal and on the second order susceptibility coefficient $\chi^{(2)}$.

The behavior of the fields depends on the total losses γ'_j inside the cavity. These losses are split in basically in two types, losses associated with the transmission through the coupling mirror γ_j and spurious losses μ_j, that may occur due to scattering in optical surfaces or absorption in the crystal, such that the total losses are $\gamma'_j = \gamma_j + \mu_j$. Oscillation occurs when the gain overcomes the total losses.

Taking φ_j to be the accumulated phase in a round trip, we define the normalized detuning as $\Delta_j = \delta\varphi_j/\gamma'_j$, where $\delta\varphi_j$ is the detuning of the field j from the cavity resonance. Considering the steady state condition, we obtain the amplitude of the fields in a round trip inside the cavity close to resonance ($\delta\varphi_j \ll 2\pi$) by integrating equations 4.2:

$$\begin{aligned} \alpha_0\,\gamma'_0\,(1 - i\Delta_0) &= -2\chi^*\alpha_1\,\alpha_2 + \sqrt{2\gamma_0}\,\alpha_0^{\text{in}}, \\ \alpha_1\,\gamma'_1\,(1 - i\Delta_1) &= 2\chi\alpha_0\,\alpha_2^*, \\ \alpha_2\,\gamma'_2\,(1 - i\Delta_2) &= 2\chi\alpha_0\,\alpha_1^*, \end{aligned} \tag{4.3}$$

where

$$\chi = \chi_{\text{eff}}\,l\,\frac{\sin(\Delta k\,l/2)}{\Delta k\,l/2}\mathrm{e}^{-i\Delta k\,l/2}. \tag{4.4}$$

We can draw conclusions about the operation of the OPO from equations 4.3. If we look at the trivial solution $\alpha_1 = \alpha_2 = 0$, we find that its stability holds until a specific value for the incident pump amplitude α_0^{in} is reached, after that the OPO oscillates and α_1 and α_2 are no longer zero. Through some manipulation of the second and third equations we find that the detunings for signal and idler must be the same ($\Delta_1 = \Delta_2 = \Delta$) for the steady state operation (Debuisschert *et al.*, 1993). Given this condition the intracavity power necessary for oscillation depends on the total losses for those modes, on their detunings and on the coupling coefficient χ, which in turn is a function of the phase mismatch

(equation 4.4), such that:

$$|\alpha_0|^2 = \frac{\gamma_1'\gamma_2'(1+\Delta^2)}{4|\chi|^2}. \tag{4.5}$$

Now if we look at the first of equations 4.3 and at equation 4.5 we find the threshold value with respect to the incoming power

$$|\alpha_0^{\text{in}}|^2_{\text{th}} = \frac{{\gamma_0'}^2\gamma_1'\gamma_2'(1+\Delta^2)(1+\Delta_0^2)}{8|\chi|^2\gamma_0}. \tag{4.6}$$

With equation 4.4 in mind, it is easy to see that the effect of phase mismatch is to increase the threshold. The minimum value of equation 4.6 is obtained for zero detuning ($\Delta = \Delta_0 = 0$), this is the on resonance threshold power ($|\alpha_0^{\text{in}}|^2_{\text{res}}$). We use this minimum value to define the incoming power normalized by the resonance power at zero detuning:

$$\sigma = \frac{|\alpha_0^{\text{in}}|^2}{|\alpha_0^{\text{in}}|^2_{\text{res}}}. \tag{4.7}$$

The OPO output power may be obtained from equations 4.3 and 4.6 (Martinelli *et al.*, 2001). After some calculations we can write the following expression for the normalized pump power (equation 4.7):

$$\sigma = \left(1 - \Delta\Delta_0 + \frac{4|\chi|^2|\alpha_1|^2}{\gamma_2'\gamma_0'}\right)^2 + (\Delta + \Delta_0)^2. \tag{4.8}$$

The non-zero stable solution for the output power through the coupling mirror for the triply resonant condition and $\Delta\Delta_0 \leq 1$ is:

$$|\alpha_j^{\text{out}}|^2 = \frac{\gamma_j\gamma_k'\gamma_0'}{2|\chi|^2}(\sqrt{\sigma} - 1), \tag{4.9}$$

with $j, k = 1, 2$ and $j \neq k$. This solution becomes unstable and the OPO enters a self pulsing chaotic operation for high values of the pump and the detunings.

The efficiency of the OPO can be obtained considering the total output power P_{out}, which is the sum of the output powers of the signal and idler beams. Assuming, as we may in our case, that all the losses and the frequencies for both beams are the same we get

$$P_{\text{out}} = \hbar\omega_0\left[\frac{\gamma\gamma'\gamma_0'}{2|\chi|^2}(\sqrt{\sigma} - 1)\right] = 4\eta_{\max}(\sqrt{P \cdot P_{\text{th}}} - P_{\text{th}}), \tag{4.10}$$

where P is the input power, $P_{\text{th}} = |\alpha_0^{\text{in}}|^2_{\text{th}}$, $\gamma = \gamma_1 = \gamma_2$ and the same goes for the total losses γ'. The maximum efficiency is defined as

$$\eta_{\max} = \frac{\gamma}{\gamma'}\frac{\gamma_0}{\gamma_0'} = \xi\xi_0, \tag{4.11}$$

where $\xi_j = \gamma_j/\gamma_j'$.

Although this discussion gives us important insight on the oscillation conditions for the OPO and the output powers for signal and idler, it is not enough for us to draw conclusions about the correlations between the three fields, which ultimately is our goal. For that we need a quantum treatment of this system.

4.1.2 Quantum Description

In the quantum description of the OPO, we need to use a set tools capable of dealing with the time evolution of our quantum system in the presence of losses. For that we use the master equation formalism, which considers the coupling of the system of interest to a heat bath (or a reservoir). A detailed derivation of this equation for the density operator can be found in Walls and Milburn (2008), and considering the three fields in our OPO and their losses we may write it as:

$$\frac{d}{dt}\rho = -\frac{i}{\hbar}\left[H_{\text{f}} + H_{\text{i}} + H_{\text{ext}}\,,\,\rho\right] + (\Lambda_0 + \Lambda_1 + \Lambda_2)\rho. \tag{4.12}$$

The Hamiltonian for the free fields propagating inside the cavity $H_{\rm f}$ is

$$H_{\rm f} = -\hbar\Delta_0\frac{\gamma_0'}{\tau}a_0^\dagger a_0 - \hbar\Delta_1\frac{\gamma_1'}{\tau}a_1^\dagger a_1 - \hbar\Delta_2\frac{\gamma_2'}{\tau}a_2^\dagger a_2, \tag{4.13}$$

where we have dropped the hat in our notation for the annihilation (creation) operator a_j ($a_j^\dagger$), and τ is the intracavity round-trip time.

The the effective interaction Hamiltonian for the three fields $H_{\rm i}$ describes the parametric down-conversion process in the nonlinear crystal:

$$H_{\rm i} = i\hbar\frac{2\chi}{\tau}(a_1^\dagger a_2^\dagger a_0 - a_1 a_2 a_0^\dagger). \tag{4.14}$$

Finally, the injection of the pump field ε in the cavity is given by

$$H_{\rm ext} = i\hbar\frac{\gamma_0}{\tau}\varepsilon(a_0^\dagger - a_0). \tag{4.15}$$

The last term inside the parenthesis in the master equation 4.12 refers to the intracavity losses for each mode j:

$$\Lambda_j\,\rho = \frac{\gamma_j'}{\tau}(2a_j\rho a_j^\dagger - a_j^\dagger a_j\rho - \rho a_j^\dagger a_j). \tag{4.16}$$

We now use the Wigner function quasi-probability representation introduced in section 2.1.1 to convert the operator master equation 4.12 into a c-number Fokker-Plank equation. This operation results in the following expression:

$$\begin{aligned}\frac{\partial}{\partial t}W(\{\alpha_j\}) = &\sum_{j=1}^{3}\frac{\gamma_j'}{\tau}\left[i\Delta_j\left(\frac{\partial}{\partial\alpha_j^*}\alpha_j^* - \frac{\partial}{\partial\alpha_j}\alpha_j\right) + \left(\frac{\partial}{\partial\alpha_j^*}\alpha_j^* + \frac{\partial}{\partial\alpha_j}\alpha_j\right)\right]W(\{\alpha_j\})\\
&+\frac{2\chi}{\tau}\left(\alpha_1\alpha_2\frac{\partial}{\partial\alpha_0^*} + \alpha_1^*\alpha_2^*\frac{\partial}{\partial\alpha_0} - \alpha_0\alpha_1^*\frac{\partial}{\partial\alpha_2} - \alpha_0^*\alpha_1\frac{\partial}{\partial\alpha_2^*} - \alpha_0\alpha_2^*\frac{\partial}{\partial\alpha_1} - \alpha_0^*\alpha_2\frac{\partial}{\partial\alpha_1^*}\right)W(\{\alpha_j\})\\
&-\left[\frac{\gamma_0}{\tau}\varepsilon\left(\frac{\partial}{\partial\alpha_0^*} + \frac{\partial}{\partial\alpha_0}\right) - \sum_{j=1}^{3}\frac{\gamma_j'}{\tau}\frac{\partial^2}{\partial\alpha_j\partial\alpha_j^*}\right]W(\{\alpha_j\}) - \frac{\chi}{2\tau}\frac{\partial^3}{\partial\alpha_0^*\partial\alpha_1^*\partial\alpha_2^*}W(\{\alpha_j\}),\end{aligned} \tag{4.17}$$

where $\{\alpha_j\} = (\alpha_0, \alpha_0^*, \alpha_1, \alpha_1^*, \alpha_2, \alpha_2^*)$. The triple partial derivative in the last term can be neglected for Gaussian states and we can write the Fokker-Plank equation 4.17 in a more compact notation:

$$\frac{\partial}{\partial t}W(\{\alpha_j\}) = -\sum_j\frac{\partial}{\partial\alpha_j}A_j\;W(\{\alpha_j\}) + \frac{1}{2}\sum_{j,k}\frac{\partial}{\partial\alpha_j}\frac{\partial}{\partial\alpha_k}[\mathbf{B}\mathbf{B}^T]_{jk}\;W(\{\alpha_j\}), \tag{4.18}$$

where A_j is an element of the drift vector $\mathbf{A}$ and $\mathbf{B}\mathbf{B}^T$ is called the diffusion matrix.

Using the notation introduced in equation 4.18 we may promptly write the Fokker-Plank equation as a set of stochastic differential equations known as Langevin equations:

$$\frac{d}{dt}\alpha_j = A_j + [\mathbf{B}\sigma(t)]_j, \tag{4.19}$$

where $\sigma(t)$ is a vector of stochastic variables with the property that

$$\langle\sigma_i(t)\sigma_j(t')\rangle = \delta_{ij}\delta(t-t'). \tag{4.20}$$

It is convenient to introduce an approximation taking the fields as having a mean value with fluctuations around it, such that

$$\alpha_j = \bar{\alpha}_j + \delta\alpha_j. \tag{4.21}$$

Under this approximation, by taking

$$\frac{d}{dt}\bar{\alpha}_j = \langle A_j\rangle \tag{4.22}$$

in the steady state condition, we recover equations 4.3, which we already had from the classical description. The extra information we obtain from the quantum mechanical treatment of the OPO comes from the fluctuations $\delta\alpha_j$. For the treatment of these fluctuations, specifically regarding our experiment, we follow the work of Andrade (2018).

We are interested in describing the field fluctuations in terms of its quadratures in phase space and we can arbitrarily make α real by a local phase rotation. In this case the quadratures can be associated to the amplitude and phase fluctuations for the intense fields involved, as $\delta q_j = i(\delta\alpha_j^* - \delta\alpha_j)$ and $\delta p_j = \delta\alpha_j^* + \delta\alpha_j$. Equation 4.19, for the fluctuations in terms of these new quadratures, becomes

$$\frac{d}{dt}\delta\chi = \mathbf{M}\,\delta\chi + \mathbf{T}\,\delta\beta + \mathbf{T}'\,\delta\epsilon, \tag{4.23}$$

where $\delta\chi = (\delta p_0, \delta q_0, \delta p_1, \delta q_1, \delta p_2, \delta q_2)^T$ is a vector that holds the fluctuations in both the phase and amplitude quadratures for each field, $\delta\beta = (\delta p_0^{\text{in}}, \delta q_0^{\text{in}}, \delta u_{p_1}, \delta u_{q_1}, \delta u_{p_2}, \delta u_{q_2})^T$ a vector for the vacuum fluctuations from the coupling through the input mirror and $\delta\epsilon = (\delta v_{p_0}, \delta v_{q_0}, \delta v_{p_1}, \delta v_{q_1}, \delta v_{p_2}, \delta v_{q_2})^T$ a vector for vacuum fluctuations introduced due to spurious losses inside the cavity.

The matrix $\mathbf{T} = \text{diag}(\sqrt{2\gamma_0}, \sqrt{2\gamma_0}, \sqrt{2\gamma_1}, \sqrt{2\gamma_1}, \sqrt{2\gamma_2}, \sqrt{2\gamma_2})$ contains the transmission coefficients through the coupling mirror and $\mathbf{T}' = \text{diag}(\sqrt{2\mu_0}, \sqrt{2\mu_0}, \sqrt{2\mu_1}, \sqrt{2\mu_1}, \sqrt{2\mu_2}, \sqrt{2\mu_2})$ the spurious losses coefficients. The matrix $\mathbf{M}$ that holds the coefficients for the drift vector in this representation is given by

$$\mathbf{M} = \begin{pmatrix} -\gamma_0' & \gamma_0'\Delta_0 & -\eta & \eta\Delta & -\eta & \eta\Delta \\ \gamma_0\Delta_0 & -\gamma_0' & -\eta\Delta & -\eta & -\eta\Delta & -\eta \\ \eta & \eta\Delta & -\gamma' & \gamma'\Delta & \gamma' & -\gamma'\Delta \\ -\eta\Delta & \eta & -\gamma'\Delta & -\gamma' & -\gamma'\Delta & -\gamma' \\ \eta & \eta\Delta & -\gamma' & -\gamma'\Delta & -\gamma' & \gamma\Delta \\ -\eta\Delta & \eta & -\gamma'\Delta & -\gamma' & -\gamma'\Delta & -\gamma' \end{pmatrix}, \tag{4.24}$$

where we write

$$\eta = \frac{2\chi|\alpha|}{\sqrt{1+\Delta^2}}. \tag{4.25}$$

The solution of equation 4.23 can be performed in the frequency domain, for that we can take its Fourier transform to obtain

$$\delta\chi(\Omega) = -\frac{1}{\mathbf{M} + 2i\gamma'\Omega}[\mathbf{T}\,\delta\beta(\Omega) + \mathbf{T}'\,\delta\epsilon(\Omega)]. \tag{4.26}$$

From this solution we can obtain the spectral matrix for the fluctuations, much like in equation 2.43, such that

$$S(\Omega)\,2\pi\delta(\Omega - \Omega') = \langle\delta\chi(\Omega)\delta\chi(-\Omega')\rangle\,. \tag{4.27}$$

By performing this operation we arrive at:

$$S = \begin{pmatrix} Sp_0 & 0 & C^R_{p_0p_1} + iC^I_{p_0p_1} & 0 & C^R_{p_0p_2} + iC^I_{p_0p_2} & 0 \\ 0 & Sq_0 & 0 & C^R_{q_0q_1} + iC^I_{q_0q_1} & 0 & C^R_{q_0q_2} + iC^I_{q_0q_2} \\ C^R_{p_1p_0} + iC^I_{p_1p_0} & 0 & Sp_1 & 0 & C^R_{p_1p_2} + iC^I_{p_1p_2} & 0 \\ 0 & C^R_{q_1q_0} + iC^I_{q_1q_0} & 0 & Sq_1 & 0 & C^R_{q_1q_2} + iC^I_{q_1q_2} \\ C^R_{p_2p_0} + iC^I_{p_2p_0} & 0 & C^R_{p_2p_1} + iC^I_{p_2p_1} & 0 & Sp_2 & 0 \\ 0 & C^R_{q_2q_0} + iC^I_{q_2q_0} & 0 & C^R_{q_2q_1} + iC^I_{q_2q_1} & 0 & Sq_2 \end{pmatrix}. \tag{4.28}$$

The diagonal elements in the matrix $S(\Omega)$ represent the noise spectrum for the phase and amplitude quadratures for each field. The off-diagonal elements represent the two by two correlations between the three fields.

4.2 Phonon Noise

There is another element we must take into account when looking at the the noise spectrum of an OPO. When taking noise measurements on their system, Villar *et al.* (2007) observed excess noise that was independent of the parametric process. This led to the development of an *ad hoc* model that considers fluctuations in the refractive index of the crystal as a consequence of local changes on its density due to thermal vibrations in the crystal lattice. This phonon noise is also present in our system and we must, therefore, introduce the model used for its treatment.

To account for the extra noise in the system, we add a vector of stochastic forces for the phase of each of the three fields (César *et al.*, 2009)

$$\delta Q = (0, \delta q_0^{\mathrm{ex}}, 0, \delta q_1^{\mathrm{ex}}, 0, \delta q_2^{\mathrm{ex}})^T \tag{4.29}$$

to equation 4.26, which describes the OPO intracavity quadrature noise, such that

$$\delta\chi(\Omega) = -\frac{1}{\mathbf{M} + 2i\gamma'\Omega}[\mathbf{T}\,\delta\beta(\Omega) + \mathbf{T}'\,\delta\epsilon(\Omega) + \delta Q]. \tag{4.30}$$

We then obtain the noise spectrum from equation 4.27 just like in the previous case.

Since, as mentioned before, this noise is assumed to be independent of the parametric process, we expect the variance of the excess noise to be proportional to the power P_j of the associated field:

$$\Delta^2 \delta q_j^{\mathrm{ex}} = \eta_j P_j, \tag{4.31}$$

η_j is simply a proportionality constant. This dependence with the power is also extended to the coupling between two fields, whose correlations are proportional to their individual amplitudes

$$\langle \delta q_i^{\mathrm{ex}}(\Omega) \delta q_j^{\mathrm{ex}}(-\Omega) \rangle = \eta_{ij} \sqrt{P_i P_j}, \tag{4.32}$$

such that η_{ij} is a coupling constant that depends on the crystal length l and on the effective Rayleigh length for the cavity (Coelho, 2009).

Given the assumption that the excess noise described so far is a consequence of phonons due to vibrations in the crystal lattice, we can assume that it is proportional not only to the power, but to the average number of phonons $\langle n \rangle$. Since the average number of phonons in a solid depends on the temperature T_c we can say, to a first order approximation, that the excess phase noise S_q is also proportional to the temperature:

$$S_q \propto P \times T_c. \tag{4.33}$$

This indicates that lowering the temperature of the crystal can be an effective course of action into reducing the excess phase noise in our system and improving the correlations between the three fields.

According to Villar *et al.* (2004), extra noise in the pump can degrade the entanglement. This is true because the noise term in equation 4.29 can be seen as spurious losses that are responsible for reducing the level of squeezing in the phase quadratures. Since squeezing and entanglement are intimately related the system will experience a reduction on its level of entanglement. Mathematically, as we will see in the following sections, less squeezing in the quadratures of interest implies in higher values for their variances, eventually preventing the violation of the inequalities that are used to demonstrate the separability of the system.

4.3 Quantum Correlations

Now that we are able to build a matrix that contains the correlations between pump, signal and idler and are able to consider the effects of thermal noise in our OPO, we are interested in investigating what information can be extracted from these correlations under such experimental conditions.

4.3.1 Squeezing

We have seen from the quantum description of the parametric downconversion inside the OPO that correlations between the three fields are inherent to the process. However, we are interested in checking whether these correlations are stronger than the allowed by classical processes. For that we define new quadratures through the linear transformation:

$$\begin{aligned} \delta p_{\pm} &= \frac{\delta p_1 \pm \delta p_2}{\sqrt{2}}, \\ \delta q_{\pm} &= \frac{\delta q_1 \pm \delta q_2}{\sqrt{2}}, \end{aligned} \tag{4.34}$$

and calculate their noise spectrum from the Langevin Equations, like we did for the the phase and amplitude quadratures in equation 4.23. The pump quadratures remain the same.

In this space, the quadrature subtraction of the amplitudes δp_- and the quadrature subtraction of the phases δq_- are completely decoupled from the other quadratures. The calculation of their noise spectra results in (Fabre *et al.*, 1990):

$$\begin{aligned} S_{p_-} &= 1 - \frac{\gamma/\gamma'}{1+\Omega'^2}, \\ S_{q_-} &= 1 + \frac{\gamma/\gamma'}{\Omega'^2}. \end{aligned} \tag{4.35}$$

We can see from figure 4.2, which plots both noise spectra, that the parametric process introduces squeezing in the subtraction of the amplitudes given that its spectrum lies entirely below the shot noise limit. We can also see excess noise in the subtraction of the phases, which is expected since Heisenberg's uncertainty principle must be respected. The presence of squeezing indicates that quantum resources were used in the generation of these states.

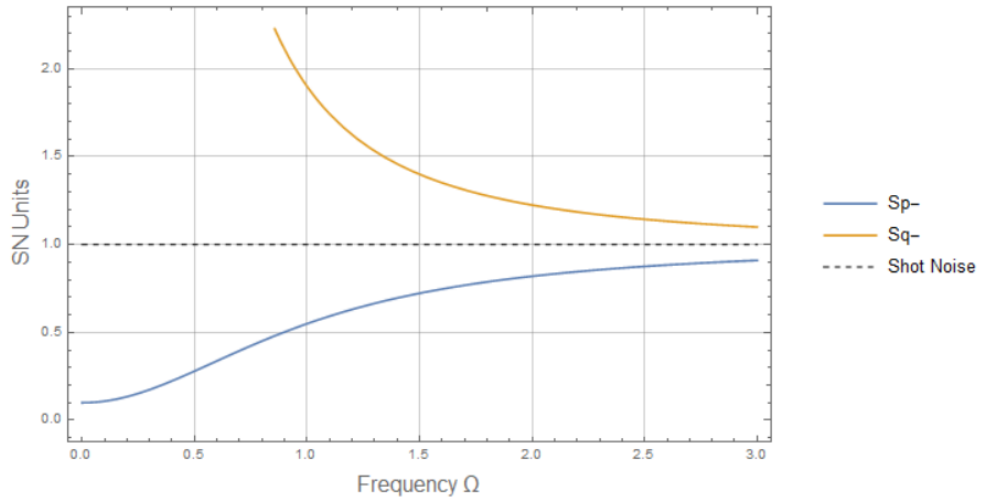

Figure 4.2: Noise spectrum for the subtraction of amplitudes S_{p_-} and subtraction of phases S_{q_-} at zero detuning. S_{p_-} presents noise compression below the shotnoise limit indicating squeezing while S_{q_-}'s noise is always greater than the shotnoise limit and assintotically tends to it as Ω increases.

4.3.2 Bipartite Entanglement

As we have shown for the spectra of the subtraction quadratures 4.35, when we calculate the noise spectrum for the sum of the phases S_{q_+} and amplitudes S_{p_+}, we find that S_{q_+} is squeezed while S_{p_+} has excess noise (Andrade, 2018). The existence of squeezing in the sum of the phases and in the

subtraction of the amplitudes of signal and idler indicates strong correlations between these quadratures. In fact they can be seen as a pair of EPR like operators and according to Duan *et al.* (2000) we can define an inseparability criterion based on their variances that provides a necessary and sufficient condition for entanglement between Gaussian states.

A quantum system is said to be entangled when its inseparable, meaning that it cannot be factored as a product of states of its local constituents. Duan *et al.* (2000) found that there is a lower bound to the total variance of separable states, which means that states that violate this lower bound are entangled. For the quadratures as defined in equation 4.34 this lower bound is given by

$$\Delta^2\left(\frac{p_1-p_2}{\sqrt{2}}\right)+\Delta^2\left(\frac{q_1+q_2}{\sqrt{2}}\right)\geq 2. \tag{4.36}$$

In fact, for the case of the signal and idler fields generated in an OPO we find that the inequality 4.36 is violated, demonstrating bipartite entanglement between them (Andrade, 2018; Coelho, 2009).

4.3.3 Tripartite Entanglement

Up to this point we have shown that signal and idler are expected to be entangled. Now we need to see how adding the pump to the problem influences the entanglement between the three fields. We have seen in the description of the OPO that the parametric process introduces phase correlations due to conservation of energy and amplitude correlations by the annihilation of a pump photon and the creation of signal and idler photons, we now need a way to characterize these correlations like we did for the bipartite scenario.

A demonstration of entanglement between pump signal and idler in above threshold OPO was first proposed in our group by Villar *et al.* (2006) and demonstrated by Coelho *et al.* (2009). As stated in these works, we can verify entanglement between the three fields by extending the bipartite separability criterion introduced by Duan *et al.* (2000) to account for the three subsystems as proposed by van Loock and Furusawa (2003). This results in a set of three inequalities that when violated are enough to determine genuine tripartite entanglement:

$$\begin{aligned}
V_0 &= \Delta^2\left(\frac{p_1-p_2}{\sqrt{2}}\right)+\Delta^2\left(\frac{q_1+q_2-g_0q_0}{\sqrt{2}}\right)\geq 2,\\
V_1 &= \Delta^2\left(\frac{p_0+p_2}{\sqrt{2}}\right)+\Delta^2\left(\frac{g_1q_1+q_2-q_0}{\sqrt{2}}\right)\geq 2,\\
V_2 &= \Delta^2\left(\frac{p_0+p_1}{\sqrt{2}}\right)+\Delta^2\left(\frac{q_1+g_2q_2-q_0}{\sqrt{2}}\right)\geq 2,
\end{aligned} \tag{4.37}$$

where g_j are parameters that minimize the left hand side of equations 4.37. These parameters can be calculated by differentiating each of the equations with respect to the relevant g_j and setting the result to equal zero. We then obtain:

$$g_0=\frac{C^R_{q_0q_1}+C^R_{q_0q_2}}{\Delta^2 q_0},\qquad g_1=\frac{C^R_{q_0q_1}-C^R_{q_1q_2}}{\Delta^2 q_1},\qquad g_2=\frac{C^R_{q_0q_2}-C^R_{q_1q_2}}{\Delta^2 q_2}. \tag{4.38}$$

Substituting them in equations 4.37 we obtain

$$\begin{aligned}
V_0 &= \Delta^2\left(\frac{p_1-p_2}{\sqrt{2}}\right)+\Delta^2\left(\frac{q_1+q_2}{\sqrt{2}}\right)-\beta_0\geq 2,\\
V_1 &= \Delta^2\left(\frac{p_0+p_2}{\sqrt{2}}\right)+\Delta^2\left(\frac{q_2-q_0}{\sqrt{2}}\right)-\beta_1\geq 2,\\
V_2 &= \Delta^2\left(\frac{p_0+p_1}{\sqrt{2}}\right)+\Delta^2\left(\frac{q_1-q_0}{\sqrt{2}}\right)-\beta_2\geq 2,
\end{aligned} \tag{4.39}$$

where

$$\beta_0=\frac{(C^R_{q_0q_1}+C^R_{q_0q_2})^2}{2\Delta^2 q_0},\qquad \beta_1=\frac{(C^R_{q_0q_1}-C^R_{q_1q_2})^2}{2\Delta^2 q_1},\qquad \beta_2=\frac{(C^R_{q_0q_2}-C^R_{q_1q_2})^2}{2\Delta^2 q_2}. \tag{4.40}$$

Relations 4.39, like equation 4.36, depend on the sum and subtraction of the bipartitions of the system with an added correlation with the third field given by β_j. Violation of two of the inequalities 4.39 is enough to determine that the three fields are entangled. Also from the same equations we see that phase noise added to the quadratures due to coupling with phonon noise will increase the variance of the sum and subtraction of the phases, making it more difficult to violate these inequalities.

4.4 Quantum Teleportation

In this section we will discuss the teleportation of quantum modes of light as presented by Furusawa and van Loock (2011). This was performed in an unconditional fashion for the first time by Furusawa *et al.* (1998) showing a fidelity in the teleportation larger than the classical limit of 0.5 for Gaussian states. Similar propositions for our system, where we use an above threshold OPO, were given by Andrade (2018), where she discusses for instance how to implement generalized quantum teleportation with two receivers, a type of quantum telecloning using the entanglement between the pump and the downconverted fields to perform teleportation between different wavelengths.

A continuous variable teleportation can be performed as displayed in figure 4.3. A pair of EPR beams $(\hat{x}_\mathrm{A}, \hat{p}_\mathrm{A})$ and $(\hat{x}_\mathrm{B}, \hat{p}_\mathrm{B})$ is generated by an OPO and each of them is sent to a different station, Alice (A) and Bob (B), respectively. A generic Gaussian state $(\hat{x}_\mathrm{in}, \hat{p}_\mathrm{in})$ is prepared in a station called Victor and sent to Alice. Alice then performs a Bell state measurement by mixing her part of the EPR pair with Victor's state and measuring $\hat{x}_\mathrm{u}$ and $\hat{p}_\mathrm{v}$ such that:

$$\hat{x}_\mathrm{u} = \frac{\hat{x}_\mathrm{in} - \hat{x}_\mathrm{A}}{\sqrt{2}}, \qquad \hat{p}_\mathrm{v} = \frac{\hat{p}_\mathrm{in} + \hat{p}_\mathrm{A}}{\sqrt{2}}, \tag{4.41}$$

where

$$\begin{aligned} \hat{x}_\mathrm{A} &= \frac{\mathrm{e}^{+r}\,\hat{x}_\mathrm{i}^{(0)} + \mathrm{e}^{-r}\,\hat{x}_\mathrm{ii}^{(0)}}{\sqrt{2}}, \qquad \hat{p}_\mathrm{A} = \frac{\mathrm{e}^{-r}\,\hat{p}_\mathrm{i}^{(0)} + \mathrm{e}^{+r}\,\hat{p}_\mathrm{ii}^{(0)}}{\sqrt{2}}, \\ \hat{x}_\mathrm{B} &= \frac{\mathrm{e}^{+r}\,\hat{x}_\mathrm{i}^{(0)} - \mathrm{e}^{-r}\,\hat{x}_\mathrm{ii}^{(0)}}{\sqrt{2}}, \qquad \hat{p}_\mathrm{B} = \frac{\mathrm{e}^{-r}\,\hat{p}_\mathrm{i}^{(0)} - \mathrm{e}^{+r}\,\hat{p}_\mathrm{ii}^{(0)}}{\sqrt{2}}. \end{aligned} \tag{4.42}$$

Here $(\hat{x}_\mathrm{i}^{(0)}, \hat{p}_\mathrm{i}^{(0)})$ and $(\hat{x}_\mathrm{ii}^{(0)}, \hat{p}_\mathrm{ii}^{(0)})$ are vacuum modes and r is the squeezing parameter. Depending on the efficiency η of the homodyne measurements performed by Alice, $\hat{x}_\mathrm{u}$ and $\hat{p}_\mathrm{v}$ will fluctuate due to the addition of vacuum noise.

Alice electronically sends the results x_u and p_v of her homodyne measurements to Bob. These are now classical variables, therefore the hat notation has been dropped in this situation. Bob after receiving this information uses it to modulate the phase and amplitude of a coherent beam with an overall gain g. By interfering this beam with his branch of the EPR pair in a high reflectivity mirror he creates the teleported output state

$$\begin{aligned} \hat{x}_\mathrm{tel} &= \hat{x}_\mathrm{B} + g\sqrt{2}\,x_\mathrm{u}, \\ \hat{p}_\mathrm{tel} &= \hat{p}_\mathrm{B} + g\sqrt{2}\,p_\mathrm{v}. \end{aligned} \tag{4.43}$$

The entangled state share between Alice and Bob allows us to use equations 4.41 and 4.42 to write Bob's part of the EPR pair as

$$\begin{aligned} \hat{x}_\mathrm{B} &= \hat{x}_\mathrm{in} - \sqrt{2}\,\mathrm{e}^{-r}\,\hat{x}_\mathrm{ii}^{(0)} - \sqrt{2}\,\hat{x}_\mathrm{u}, \\ \hat{p}_\mathrm{B} &= \hat{p}_\mathrm{in} + \sqrt{2}\,\mathrm{e}^{-r}\,\hat{p}_\mathrm{i}^{(0)} - \sqrt{2}\,\hat{p}_\mathrm{v}. \end{aligned} \tag{4.44}$$

Using this result and considering a system with high detection efficiency ($\eta \approx 1$) and unit gain ($g = 1$) the teleported state becomes:

$$\begin{aligned} \hat{x}_\mathrm{tel} &= \hat{x}_\mathrm{in} - \sqrt{2}\,\mathrm{e}^{-r}\,\hat{x}_\mathrm{ii}^{(0)}, \\ \hat{p}_\mathrm{tel} &= \hat{p}_\mathrm{in} + \sqrt{2}\,\mathrm{e}^{-r}\,\hat{p}_\mathrm{i}^{(0)}. \end{aligned} \tag{4.45}$$

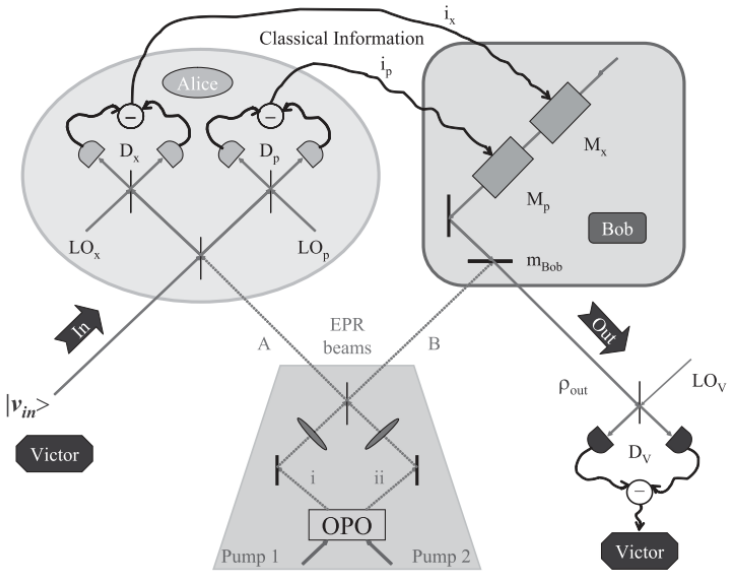

Figure 4.3: Schematic representation of a teleportation protocol. *Reprinted from* Furusawa and van Loock (2011).

We see that for the ideal case of infinite squeezing ($r \to \infty$) we completely recover the initial state prepared by Victor.

So, the quality of the teleported state depends not only on the level of squeezing generated by the OPO but also on the detection efficiency η and on the gain (g), which can be determined operationally and made very close to unity. Also recent detectors allow for very high detection efficiencies making the quality of the squeezing the most determinant parameter in the teleportation fidelity.

4.4.1 Teleportation Fidelity

The usual way to quantify the quality of the teleported state is through the fidelity. It uses the overlap between the original state and the output state to determine their degree of similarity. This can be expressed by

$$F \equiv \langle \psi_{\text{in}} | \, \hat{\rho}_{\text{out}} \, | \psi_{\text{in}} \rangle \, , \tag{4.46}$$

where $|\psi_{\text{in}}\rangle$ is the initial pure state and $\hat{\rho}_{\text{out}}$ the density operator for the output state. Without a shared entangled state, the best possible value for fidelity in the teleportation of a coherent state is 0.5.

The general expression for the fidelity in the teleportation of a coherent state can given by (Furusawa and van Loock, 2011)

$$F = \frac{1}{2\sqrt{\sigma_Q^x \, \sigma_Q^p}} \exp\left[-(1-g)^2 \left(\frac{x_{\text{in}}^2}{2\sigma_Q^x} + \frac{p_{\text{in}}^2}{2\sigma_Q^p} \right) \right] , \tag{4.47}$$

where the variances σ_Q^x and σ_Q^p are calculated as follows

$$\sigma_Q^{x,p} = \frac{1}{4}(1+g^2) + \frac{\mathrm{e}^{2r_{x,p}}}{8}(g\xi_A - \xi_B)^2 + \frac{\mathrm{e}^{-2r_{x,p}}}{8}(g\xi_A + \xi_B)^2 + \frac{1}{4}(1-\xi_A^2)g^2 + \frac{1}{4}(1-\xi_B^2) + \frac{g^2}{2}\left(\frac{1}{\eta^2} - 1\right) , \tag{4.48}$$

where $r_{x,p}$ refers to the squeezing parameters for each quadrature, $\xi_{A,B}$ the efficiency with which the EPR beams propagate (in the presence of losses $\xi_{A,B} < 1$).

Phonon noise degrades squeezing and since higher fidelity requires more squeezing, we see from equations 4.47 and 4.48 that high levels of phonon noise can make it very unlikely to perform a teleportation protocol with fidelity higher than the classical limit.

5 EXPERIMENTAL IMPLEMENTATION AND METHODS

In this chapter we describe the experiment for the generation of tripartite entanglement. We begin by introducing a Titanium Sapphire (Ti:Sapph) laser and the saturated absorption scheme we use to lock its frequency to the D2 transition of the Rubidium (Rb) atom. Then we proceed to the OPO description and the different configurations proposed to reduce the influence of phonon noise. Finally we conclude with a description of the photodetectors and the analysis cavities used to rotate the noise ellipse and convert phase noise into amplitude noise, as described in section 2.3.2.

5.1 Pump Laser: Ti:Sapph

The pump laser for our OPO is a homemade tunable Titanium Sapphire (Ti:Sapph) laser built by Moraes (2013) as part of his Master's thesis. The advantages of using Ti:Sapph lasers is that besides their high tunability, typically allowing for operating wavelengths between 650 nm and 1100 nm, they are able to produce extremely narrow linewidth coherent Gaussian beams. The linewidth of our laser is less than 0.2 MHz and, as showed by Andrade (2018), can be considered coherent for analysis frequencies above 9 MHz.

As shown in figure 5.1, the laser itself consists of a Ti:Sapph crystal inside a bow tie propagating wave cavity pumped by a Lighthouse Sprout-D 532 nm diode-pumped solid-state laser. The pump laser goes through the coupling lens $L1$ to match the cavity's modes and enters it through the coupling mirror $M1$. The Lyot filter LF is used as narrow optical pass-band filter to reduce the frequency modes allowed in the cavity and the etalon reduces even further the frequency modes, allowing our laser to operate in the single mode regime.

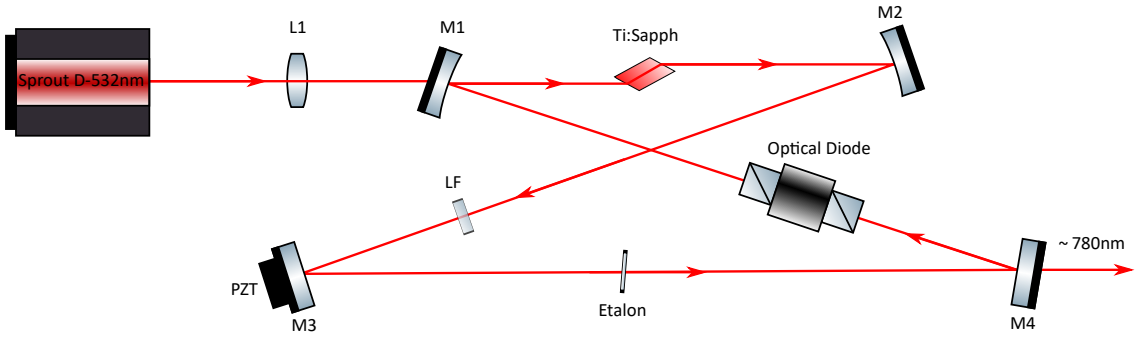

Figure 5.1: Schematic representation of the homemade Titatnium Sapphire laser used in our experiment. $L1$ is the coupling lens, $M1$ is the input mirror, mirror $M3$ has a PZT attached to control cavity length, $M4$ is the output mirror and LF is a Lyot Filter.

Essentially, by tuning the Lyot filter we select a range of frequencies for our laser to operate and by adjusting the etalon angle we select a specific frequency mode. The PZT attached to mirror $M3$ uses the piezoelectric effect to change its size and on doing so changing the size of the cavity and consequently its resonance frequency. This allows us to precisely select a frequency of operation for our laser. The optical diode is used to prevent light from propagating in the opposite direction, increasing the laser efficiency.

Because we are interested in using this system to interact with Rubidium atoms and also to provide a stable frequency reference to lock the laser, we decided to use a saturated absorption scheme to frequency lock the laser at the Rb D2 atomic transition, yielding an operation wavelength of roughly 780 nm. This is done by generating an error signal from the saturated absorption spectrum and using it

to lock the size of the cavity using the PZT at mirror $M3$. Upon doing so we are making sure that the peak of the transmitted mode matches the selected hyperfine atomic transition.

5.1.1 Frequency Locking: Saturated absorption of Rubidium

The experimental setup used to obtain the saturated absorption spectrum of Rb is depicted in figure 5.2. The incoming beam gets partially transmitted and partially reflected at the first interface of a thick glass slab. The transmitted beam then gets partial transmission (solid line) and reflection (dashed line) at the second interface. The path represented by the dashed line passes the Rb cell in a single direction and is picked-up by photodetector $PD2$. The path represented by the solid line passes the Rb cell in both directions and is picked-up at detector $PD1$, the reflected beam is called probe and the transmitted is called pump.

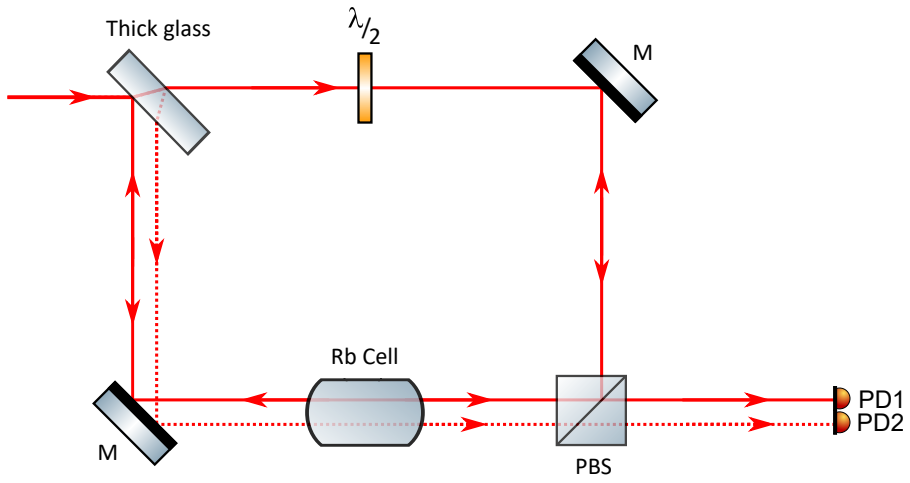

Figure 5.2: Schematic representation of the experimental setup used to obtain the saturated absorption spectrum of Rb. The mirrors are represented by M, $\lambda/2$ is a half waveplate and $PD1$ and $PD2$ are photodetectors 1 and 2 for the detection of the Doppler free and Doppler broadened spectra respectively.

By sending a voltage ramp to the PZT attached to mirror $M3$ in the Ti:Sapph cavity (figure 5.1), we set the laser to scanning mode, varying its frequency around the Rb D2 transition. Upon doing so, the signal observed by photodetector $PD2$ generated by the single pass path (dashed line in figure 5.2) cannot resolve the hyperfine transitions due to the Doppler broadening. This signal is depicted by the red curve in figure 5.3.

However, the double pass path (solid line) can resolve the hyperfine lines. This is because, near resonance, the pump beam and the probe beam address the same atoms, those with velocities orthogonal to the direction of laser propagation. This means that the strong pump saturates the atomic transitions reducing the absorption of the probe for those atoms and resolving the blue peaks in figure 5.3.

Now that we have the setup to generate the generate signals that can resolve peaks at the hyperfine transitions, we use a lock-in amplifier to generate the error signal. The lock-in amplifier sends a dither (sine wave) signal to the PZT inside the Ti:Sapph cavity scanning the laser frequency. The dithered Doppler free saturated absorption spectrum is picked up at detector $PD1$ and sent back as an input to the lock-in amplifier. Both signals are then electronically mixed forming a beat signal and higher frequency components are removed by built-in low pass filters. The error signal obtained is displayed in figure 5.4 (b) and each error signal is matched to its respective hyperfine peak in figure 5.4 (a).

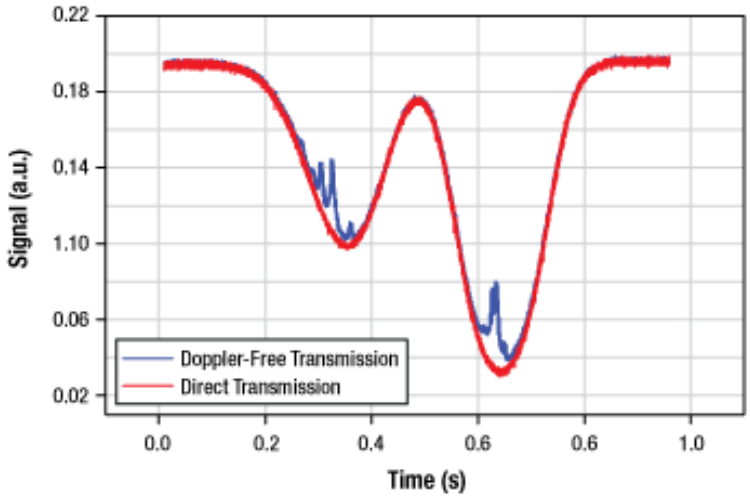

Figure 5.3: Absorption spectrum of rubidium atoms around the D2 transition line. The red line represents the direct transmission and the blue line the Doppler free transmission.

The error signal of figure 5.4 (b) is then fed to a PID[1] controller that is responsible for adjusting the PZT voltage to keep the size of the cavity such that the sharp slope signal intercepts zero. We see from the dashed line in the figure that the peaks in part (a) exactly match the zero intercepts in part (b). If the laser frequency drifts away from the frequency of the atomic reference, the error signal is no longer zero and the cavity size is increased or decreased to correct the drift.

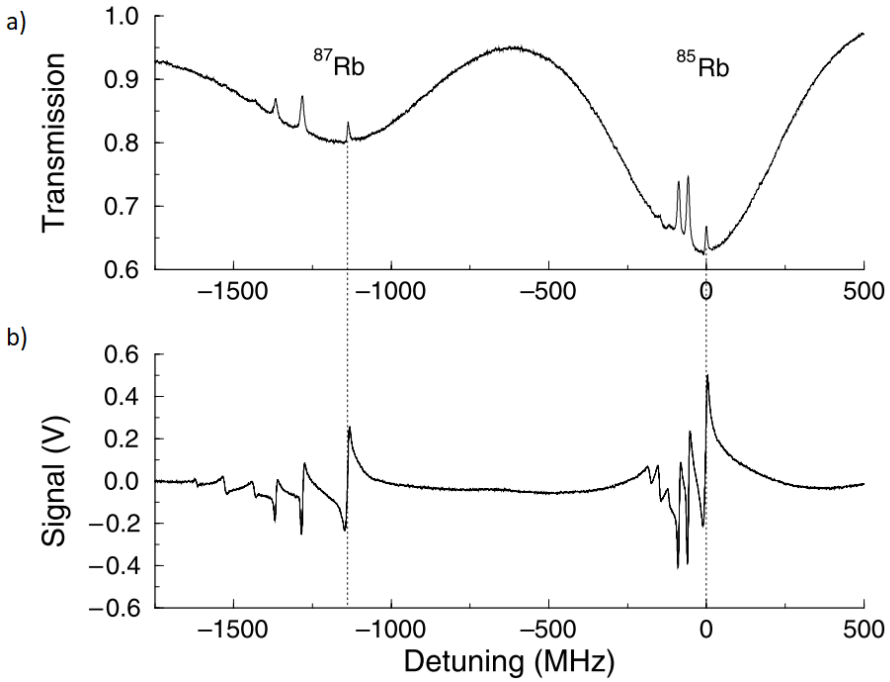

Figure 5.4: (a) Doppler free saturated absorption spectrum of Rb. (b) Error signal obtained through the dither locking technique. The sharp slope in the error signal intercepts zero exactly at the central frequency of its corresponding hyperfine peak.

[1] proportional–integral–derivative.

5.2 The OPO Cavity

Our OPO consists essentially in a linear cavity with a periodically poled potassium titanyl phosphate (PPKTP) crystal as the gain medium responsible for the parametric downconversion and a peltier module to provide temperature control and stability, as depicted in figure 5.5a. The coupling mirror $M1$ is partially transmissible for the pump ($T_1 = 29.6(4)\,\%$ at 780 nm) and has high reflectivity for signal and idler (HR at 1560 nm). Mirror $M2$ on the other hand has high reflectivity for the pump (HR at 780 nm) and partial tranmissivity for signal and idler ($T_2 = 3.84(4)\,\%$ at 1560 nm). Both mirrors have the same radius of curvature $R_c = 25$ mm and were manufactured by ATFilms.

The cavity has its finesse F calculated based on the transmissivity of the mirrors and has values $F = 18$ at 780 nm and $F = 160$ at 1560 nm. Mirrors $M1$ and $M2$ are separated by 56 mm, forming a near concentric cavity, to obtain the optimum value of 19 µm for the beam waist in the center of the crystal (Andrade, 2018). A set of lenses are used to match the waist of the pump coming from the Ti:Sapph cavity and the waist inside the OPO cavity, making sure that near optimal mode matching is achieved for the best OPO performance. This configuration yields a bandwidth of roughly 15 MHz for the OPO. The actual OPO cavity is shown in figure 5.5b.

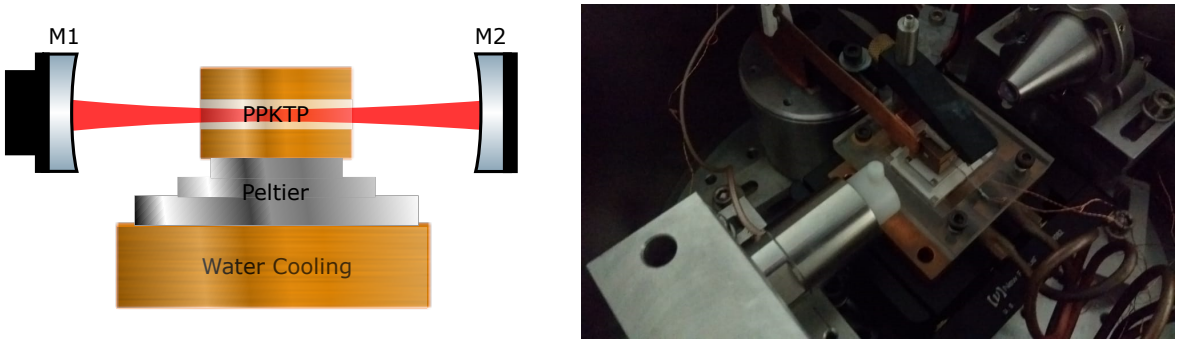

(a) (b)

Figure 5.5: (a) Schematic representation of our OPO. The PPKTP crystal is placed inside the cavity and cooled by a peltier module whose bottom face is in contact with a water cooling system at 15 °C. (b) Actual picture of the OPO inside the vacuum chamber. The crystal is held by a copper casing and clamped on top of the peltier module, a copper fork is attached to another peltier and held close to the crystal surface to function as a cold trap.

The PPKTP crystal itself is held by a copper casing and clamped on top of a Peltier module. It has type-II phase matching, 15 mm of length, degeneracy temperature between −25 °C and −75 °C and anti-reflective coatings for both 780 nm and 1560 nm. The need for stability requires active control of the temperature of the crystal to avoid drifts in the cavity size due to thermal expansion. This is performed via a temperature control circuit that stabilizes the crystal temperature by controlling the electric current being fed to the peltier. The peltier is a ceramic module that uses the Peltier effect to generate a gradient of temperature between the upper and lower surfaces given an electric current. The bottom surface is attached to a water cooling system controlled by a chiller that keeps the water temperature at 15 °C, the upper surface is in contact with the crystal's copper casing.

Our initial attempts to measure tripartite entanglement were performed at room temperature. Although we were able to measure entanglement between signal and idler under these conditions, entanglement with the pump was being degraded due to phase noise introduced by the coupling with thermal fluctuations in the crystal (César *et al.*, 2009). This led us to pursue lower temperatures of operation. However, we found, as we will show in chapter 6, that the optimal temperature of operation is below 0 °C, which means that lowering the temperature to the optimal limit will introduce condensation in the crystal and significantly increase cavity losses due to scattered light, again degrading correlations.

5.2.1 Different OPO Configurations

The initial attempt to reduce losses introduced by condensation was to simply work at a low pressure environment. However, even at pressures lower than 10^{-3} Torr (lowest possible value for our pressure gauge) we realized that there was condensation in the crystal as the temperature becomes negative. We then decided to rework the cooling system.

This new attempt at a design for cooling the crystal without condensation is shown in figure 5.6. The idea behind this scheme is that by lowering the temperature on the surface of peltier 2 as much as possible, the copper mask between peltiers 1 and 2 would function as a large cold trap for humidity, while peltier 1 would keep the crystal at slightly higher temperatures, but still negative. We hypothesized that this large cold surface area, combined with the low pressure environment, would be enough to keep the crystal at lower temperatures with no significant condensation for a period long enough for a full set of measurements.

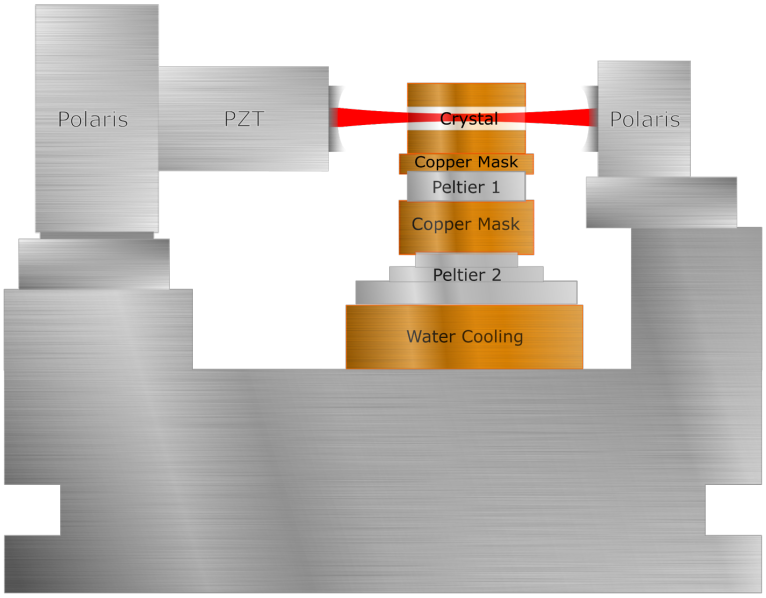

Figure 5.6: Schematic representation of an alternative cooling scheme to improve the OPO operation.

Once we had the new structure manufactured, we reassembled the OPO and started trying to lower the temperature of the upper surface of peltier 2 as much as possible. However, the copper mask would not achieve negative values in a low pressure environment, while it would at standard room pressures. This indicated that the peltier was losing efficiency at lower pressure levels.

To investigate the peltier efficiency we cleaned the vacuum chamber and removed all the extra load from it, as seen in figure 5.7, leaving only the water cooling system at 15 °C at the lower surface and measuring the upper surface temperature with a thermocouple connected to a multimeter. We then applied a safe current of 2 A (higher values would risk damaging the module due to thermal effects) and measured a difference in temperature of 26 °C between the upper and lower surfaces, way below the optimum performance of 80 °C under ideal conditions specified in the manufacturer's datasheet.

Our tests indicate that at low pressures the module operates as if it had an extra load of 3 W, rendering its use irrelevant for our purposes under these conditions. For this reason we decided to fall back to the original cooling configuration in figure 5.5a and stop working at lower pressures. Instead we decided to work with synthetic air composed of 21 % oxygen, 79 % nitrogen and very low levels of humidity. The adopted procedure was to pump the atmospheric air off the vacuum chamber for a couple

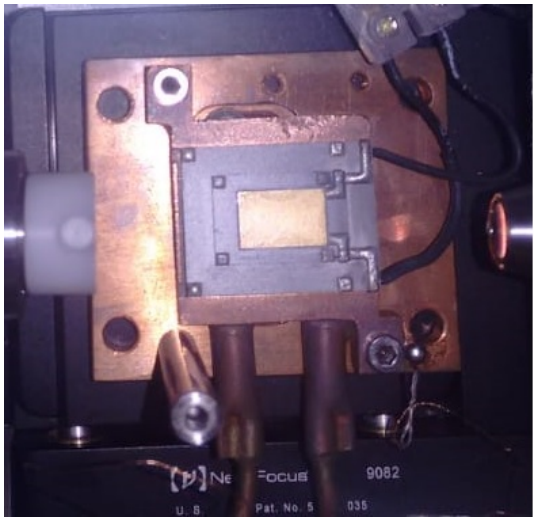

Figure 5.7: Peltier inside an empty vacuum chamber for performance testing with both synthetic air and low pressures.

of hours and then fill it with synthetic air. This substantially increased the peltier efficiency. To avoid any remaining condensation we added the fork displayed in figure 5.5b which was attached to another peltier keeping it at negative temperatures to function as a cold trap for humidity.

With this configuration we were able to reach the temperature of $-21\,°C$ with no visible degradation of the cavity finesse, or the oscillation threshold, for a period of time long enough to perform our measurements. We then decided to proceed to realign the system and verify if this temperature would be enough to reduce the phonon noise to acceptable levels to measure tripartite entanglement.

5.2.2 OPO Locking

With the pump beam frequency locked at the Rb D2 line and with the crystal's temperature stabilized at the desired levels, we need to lock the OPO cavity to maximize the output intensity of the downconverted fields and minimize amplitude fluctuations. This is done, as in the frequency locking of the Ti:Sapph, by using a dither signal to vary the cavity size to generate the output signal seen as the blue line of figure 5.8(a).

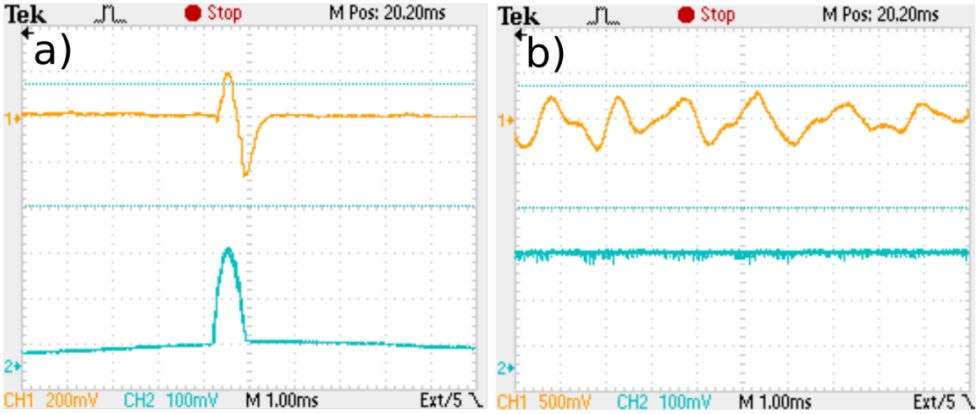

Figure 5.8: (a) Blue line: OPO output signal for the pump beam (780 nm) with the cavity in scanning mode. Yellow line: error signal. (b) Blue line: output signal for a locked OPO cavity. Yellow line: PID feedback signal sent to the PZT for locking. *Reprinted from* Andrade (2018).

To generate the error signal, instead of using a lock-in amplifier, we use homemade electronics

and a function generator that together generate the error signal pictured in yellow in figure 5.8(a), using the same principle explained for the error signal generated with the lock-in amplifier. In figure 5.8(b) the OPO is locked and we can see from the blue line that the output amplitude is stabilized at the maximum value of the blue peak in figure 5.8(a). The yellow line in 5.8(b) is the feedback signal sent by the PID to the PZT to lock the cavity.

5.3 Detection System

The last link in the experimental setup is the detection system. This is a critical step, responsible for conveying the information from the beam quadratures into electric signals we can analyze. The theory behind how the field quadratures relate to the photocurrent was explained in section 2.3. For the balanced detection scheme we use one pair of FND-100 photodiodes with measured detection efficiency of 70 % at 780 nm, these are used in the measurement of the reflected pump. For signal and idler we use two pairs of ETX-500 photodiodes with measured detection efficiency of 95 % at 1560 nm.

The photocurrent is split in two components by built in electronic circuits. The low frequency component, called DC component, is related to the intensity of the carrier. The high frequency component, called HF, carries the information contained in the sidebands of the detected field. The signal then carries on to a demodulation chain where we select a specific analysis frequency, typically between 7 MHz and 9 MHz in our system. After demodulation we send it to acquisition boards that are controlled by a National Instruments Labview program where we can visualize and store the measured data. More information about the data acquisition chain can be found in Andrade (2018).

However, as discussed earlier, photodiodes can only detect the amplitude of the electromagnetic field. To obtain phase information we use three triangular analysis cavities, one for each beam. Each of them is responsible for the rotation of the noise ellipse in phase space to convert phase fluctuations into amplitude fluctuations as described by the self homodyne detection explained in section 2.3.2.

5.3.1 Triangular Cavities: Reflected Pump, Signal and Idler

We have three triangular travelling wave cavities in our experiment, each of them function as an analysis cavity for a specific beam (pump, signal and idler) and their configuration can be seen in figure 5.9. All of them have the same length $L = 400$ mm for a round trip. $M1$ is a plane mirror with transmissivity of roughly 4 %, $M2$ is a high reflectivity plane mirror and $M3$ a high reflectivity curved mirror with a radius of curvature of 200 mm.

The cavity for the pump has an estimated finesse $F = 160$ and bandwidth $\Gamma = 4.3$ MHz. The signal and idler cavities are identical, their finesse is $F = 200$ and bandwidth $\Gamma = 4$ MHz. The PZT attached to mirror $M3$ is used to either hold the cavity size in place or set it to scanning mode to perform the rotation of the noise ellipse.

5.4 The Setup

When the elements described in the previous sections are put together, we arrive at our experimental setup for the generation and measurement of tripartite entanglement in an above threshold optical parametric oscillator, depicted in figure 5.10. The polarization of the pump beam leaving the Ti:Sapph laser is set such that it is completely transmitted through the first PBS and reaches the OPO. The reflected pump has its polarization rotated in the Faraday Rotator (FR) and is completely transmitted by the PBS into Analysis Cavity 0. Given that the OPO crystal is built with type-II phase matching, signal and idler leave the OPO cavity following the same optical path but with orthogonal polarization. They are then separated by polarization and each sent to a different analysis cavity.

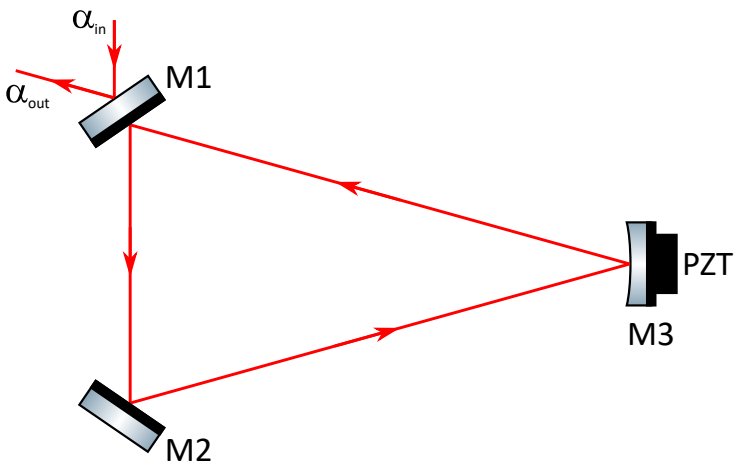

Figure 5.9: Analysis cavity for pump signal and idler. The cavity length is $L = 400\,\text{mm}$, mirror $M1$ has a transmissivity of $4\,\%$ and mirrors $M2$ and $M3$ are HR. Mirror $M3$ has a radius of curvature of $200\,\text{mm}$ and a PZT attached to scan and control cavity length.

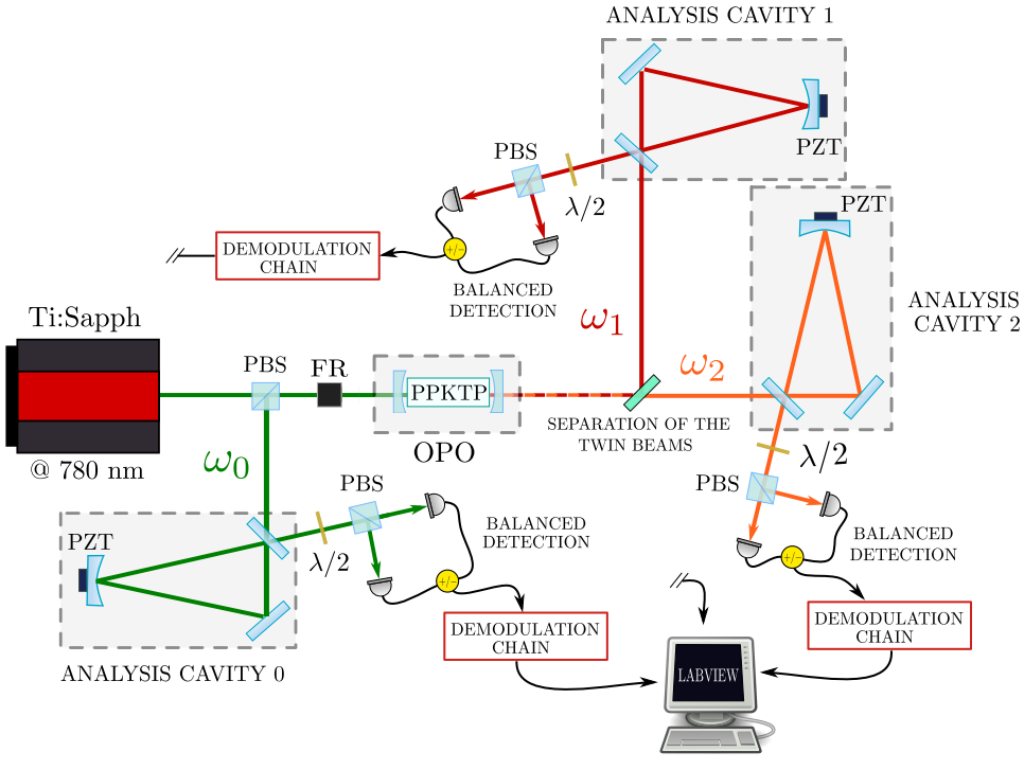

Figure 5.10: Schematic representation of our experimental setup for the generation and measurement of tripartite entanglement. *Reprinted from* Andrade (2018).

Each set of measurements consist of 4 synchronous slow sweeps of the analysis cavities through resonance for a complete noise ellipse rotation. In the first set of measurements we sweep the three cavities to obtain amplitude and phase correlations between the three fields. In the last three sets we hold one cavity detuned for amplitude fluctuations and sweep the other two. This allows us to obtain the cross correlation terms between phase and amplitude of each cavity. With the full set of measurements we have a complete tomography of our system.

6 RESULTS AND MEASUREMENTS

In this chapter we will present the measurements performed and discuss the results obtained. We will split this chapter in essentially two parts. The first part refers to our early OPO measurements, prior to the disassembly of the cavity for the attempts to reduce the crystal temperature. The second part refers to the preliminary measurements at room temperature performed in the system after the configuration that allowed us to achieve $-21\,^{\circ}\mathrm{C}$ with a stable OPO.

6.1 Early Results

Our first measurements were taken as part of the work of Andrade (2018). We started by measuring the squeezing in the amplitude difference between signal and idler $\Delta^2 p_-$ and then looking for bipartite entanglement between this quadrature and the sum of the phases $\Delta^2 q_+$. Afterwards we investigated the tripartite correlations. We verified that excess phase noise was preventing the achievement of tripartite entanglement and, after a measurement of the coupling coefficient between the pump and phonon noise, determined the optimal temperature for it to work.

6.1.1 Squeezing

The measurement of amplitude squeezing is pretty straight forward in our system. We simply look at the fluctuations of the subtraction of the photocurrents of signal and idler and compare with the shotnoise. This is what is shown in figure 6.1. There, the variance $\Delta^2 p_-$ is measured for different transmission values of a variable optical filter. This filter's function in this setup is to introduce losses for us to see the linear degradation of the squeezing towards the shotnoise level. These measurements were taken at an analysis frequency of 7 MHz where we verified 2.4 dB of squeezing.

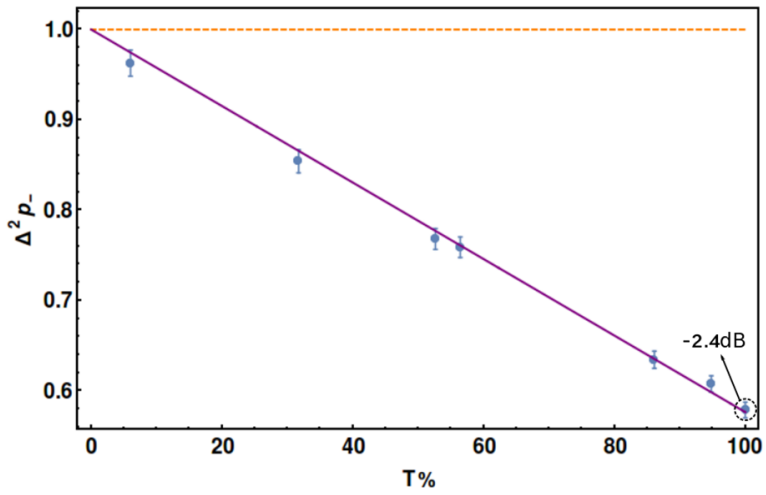

Figure 6.1: Measurement of 2.4 dB of squeezing for the quadrature subtraction of the amplitudes of signal and idler at an analysis frequency of 7 MHz. The variance $\Delta^2 p_-$ is plotted against different transmission coefficients simulating losses. The smaller the transmission coefficient the closer the variance gets to shotnoise, a clear indication of how squeezing is degraded by losses.

6.1.2 Duan Violation: Entanglement between the quadratures of the twin beams

We are now interested in verifying the entanglement between signal and idler. For that we need to define a pair of EPR like operators where we can apply the criterion developed by Duan *et al.* (2000). That is why we look at the variances $\Delta^2 p_-$ and $\Delta^2 q_+$ as explained in section 4.3.2. To obtain

the variances for these quadratures we rotate the noise ellipse for signal and idler and look at their sum and subtraction.

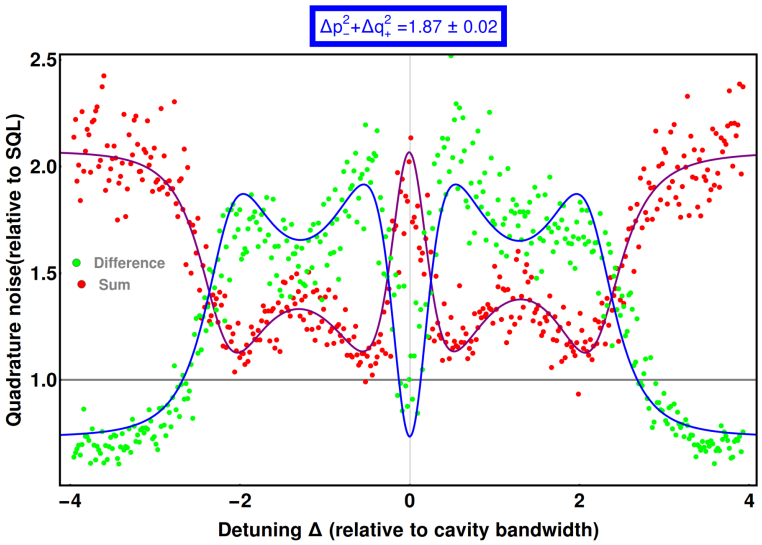

Figure 6.2: Noise ellipse rotation for the sum (red dots) and subtraction (green dots) of signal and idler. The fitting curves give us the parameters to build the covariance matrix. $\Delta^2 p_- + \Delta^2 q_+ = 1.87(2)$ indicates entanglement between signal and idler.

In the plot in figure 6.2 the green dots refer to the rotation of the noise ellipse for the difference between signal and idler and the red dots to the rotation of the noise ellipse for their sum. We can also see the squeezing for the subtraction of the amplitudes, represented by the fact the the tails of the green plot are below the shotnoise level. Although the sum of the phases (in the red plot) never drops below shotnoise, indicating excess noise for $\Delta^2 q_+$, we verify a violation of the inequality 4.36 with the value $\Delta^2 p_- + \Delta^2 q_+ = 1.87(2)$, indicating that there is in fact bipartite entanglement between signal and idler.

6.1.3 Tripartite results

These early tripartite measurements we have are thoroughly discussed as the main results in Andrade (2018). There, she analyses the symmetric and antisymmetric correlations between the quadratures of the three fields in our experiment. These measurements were performed for different pump powers, at an analysis frequency of 7 MHz and two different crystal temperatures, $T = 18\,°\mathrm{C}$ and $T = 0\,°\mathrm{C}$. With that, the spectral matrix of the system was built for each set of measurements.

To study the entanglement of the system, the Positive Partial Transpose (PPT) criterion was employed as proposed in Simon (2000). This method consists in taking the partial transposition of a subsystem of the covariance matrix. By looking at the eigenvalues of the associated symplectic matrix it can be determined if the quantum system is separable or not. The criterion states that the symplectic eigenvalues must satisfy $\nu_k \geq 1$ for the system to be considered separable. The minimum symplectic eigenvalues for the partial transposition of the pump, signal and idler are plotted in figure 6.3 as a function of the pump power. The dashed lines represent the theoretical predictions for each bipartition given the estimated losses and the dots the experimental data. In figure 6.3 (a) we have the measurements at $T = 18\,°\mathrm{C}$ and in figure 6.3 (b) at $T = 0\,°\mathrm{C}$.

These results show a clear improvement in the entanglement for the signal and idler beams, represented by ν_1 and ν_2, at $T = 0\,°\mathrm{C}$. At this temperature we see that the PPT criterion is violated for values of the pump power as high as 1.2σ, while at $T = 18\,°\mathrm{C}$ we expect no entanglement for values of the pump higher than 1.1σ. We also see a reduction in the symplectic eigenvalues ν_0 at lower temperatures

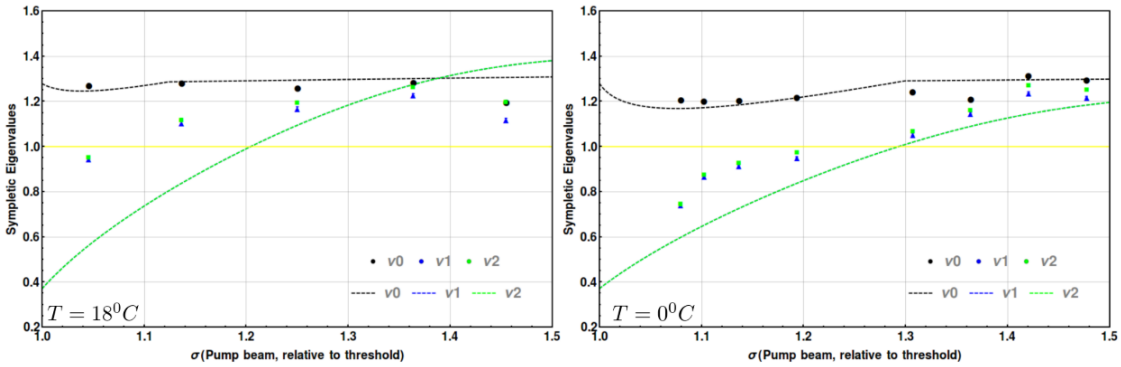

Figure 6.3: Minimum symplectic eigenvalues for the partial transposition of the pump (v_0), signal and idler (v_1 and v_2) as a function of the normalized pumping power σ. The dashed lines represent the theoretical predictions for each bipartition given the estimated losses and the dots the experimental data. The measurements were taken at (a) T=18 °C and (b) T=0 °C. *Reprinted from* Andrade (2018).

for the partial transposition of the pump, but no violation of the criterion in either case. Although we were not able to measure tripartite entanglement, these results hint that lowering the crystal temperature is the way to go to improve the system and achieve this goal.

6.1.3.1 No tripartite entanglement due to phonon noise

The justification for pursuing lower temperatures of operation in our OPO lies on the hypothesis that the coupling with the thermal vibration modes in the crystal can be seen as an extra source of spurious losses that affect the phase quadrature of the three fields, as explained in section 4.2. We then decided to look for the optimal operation temperature for our system. As explained by Andrade (2018), we measure the coupling coefficient η_{00} as a function of the temperature in the crystal, the result is shown in the plot in figure 6.4. This measurement is performed by measuring the variance of the phase quadrature of the pump beam $\delta\hat{q}_0$ and the pump power P_0 and plugging into equation 4.32 to obtain the coefficient η_{00} for different values of temperature.

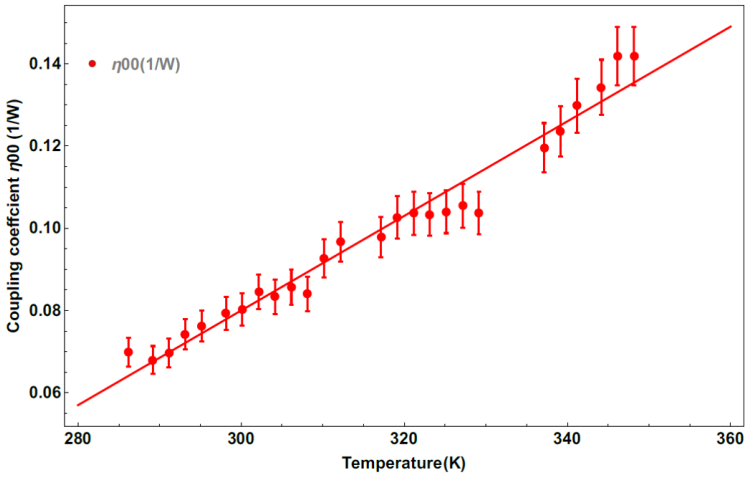

Figure 6.4: Coupling coefficient η_{00} as a function of the temperature T. For the linear regression we assume that the coupling coefficient remains linear at lower temperatures.

We then admit that the coupling coefficient varies linearly with the temperature and by linear regression we find that $\eta_{00} = 0.002059T - 0.477953$. This means that η_{00} is practically zero at around

−40 °C, rendering this the optimal temperature to measure tripartite entanglement in our system.

6.2 Recent results

As a consequence of the previous measurements we decided to rework the cooling system of the OPO to be able to stabilize it at negative temperatures. The description of how this was achieved is detailed in chapter 5. After the alignment of the system was complete we started some preliminary measurements that were performed to check if the laser, the OPO, the analysis cavities, the detection system and the demodulation and acquisition chains were all functioning properly and simultaneously.

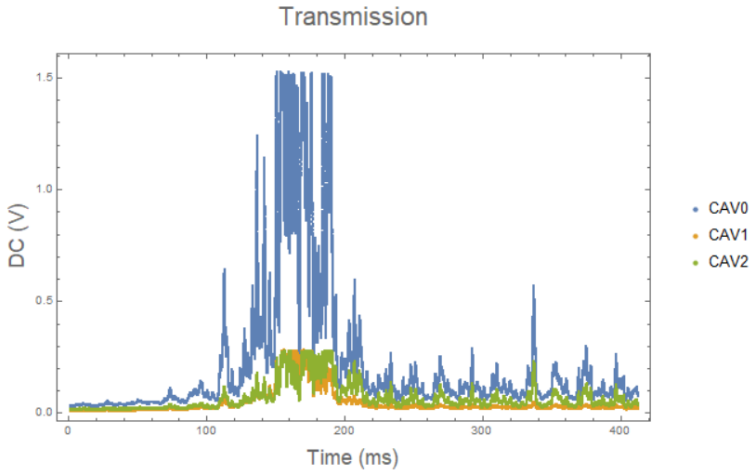

Figure 6.5: Raw data for the DC signal of the field transmitted by each of the tree analysis cavities: CAV0 (for the pump), CAV1 and CAV2 (for signal and idler).

For the measurements presented in this section we had all our systems locked. The Ti:Sapph was frequency locked at the Rb D2 line, the OPO had a 95 mW threshold and was locked at a pumping power of $\sigma \approx 1.16$. Because these were preliminary measurements for a system test, they were taken at the room temperature of 19 °C. Figure 6.5 displays the raw data for the DC signal of the field transmitted by each of the tree analysis cavities as they are scanned through resonance.

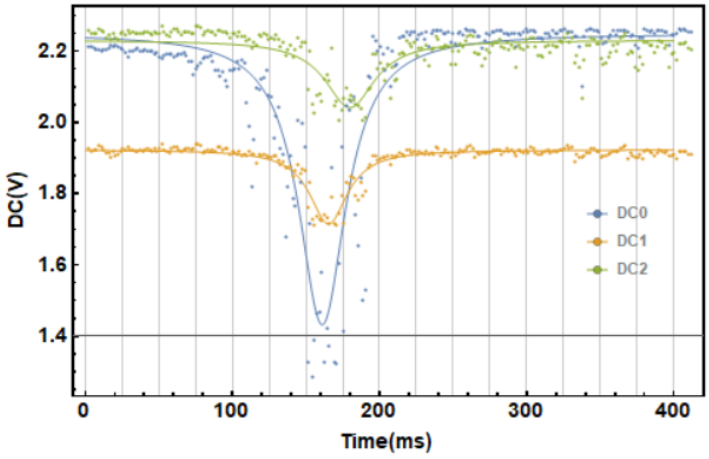

Figure 6.6: The dots in the plot show the measured value of DC in terms of the measurement time for the fields reflected by each of the analysis cavities: blue for the pump (DC0), orange and green for signal and idler (DC1 and DC2). The solid lines are the lorentzian fit to each data set.

We can clearly see from the data shown in figure 6.5 that the three signals are extremely noisy,

with many peaks even when looking far from resonance. This indicates an excessive intensity noise in the pump that can be corrected with fine tuning of the Ti:Sapph parameters of by the introduction of a noise eater to stabilize it. In figure 6.6 we have the DC signal of the beams reflected from the analysis cavities. The Lorentzian fit indicates that the cavities are slightly out of sync, a consequence of the excessive amplitude noise that makes it harder to synchronize the three peaks. Out of sync measurements will result in wrong values for the phase and amplitude correlations.

Even though the pump was too noisy for any type of correlation analysis, we could verify that the detection system and the demodulation and data acquisition chains were functioning properly. Even with a low signal to noise ratio (SNR) we were able to see the rotation of the noise ellipse in our cavities, as shown in figure 6.7 for the pump, which would allow us to obtain information about the fluctuations of the phase and amplitude quadratures.

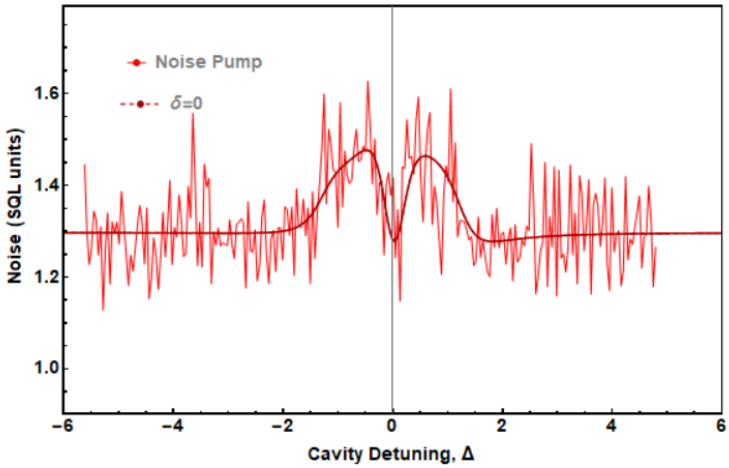

Figure 6.7: Noise ellipse rotation for the pump (analysis cavity 0).

Essentially we need to carefully control our system to reduce any sources of noise that may interfere with the correlations between the three fields, such as thermal noise in the crystal, amplitude fluctuations in the pump and spurious losses due to scattering in optical elements. With the results presented in this section we would proceed to fine tune the system, stabilize the intensity of the pump beam and drop the OPO temperature to $-21\,^{\circ}\mathrm{C}$ for better data.

7 CONCLUSION

In this first part of our work, we set out to build an optical parametric oscillator to be used as a source of entangled states of light in the implementation of quantum information protocols. We realized that, although this system is capable of generating entanglement between signal and idler, the subtraction of the amplitudes is the only squeezed quadrature, since $\Delta^2 p_- < 1$. The sum of the phases, although close to the shotnoise limit, still present excess noise with $\Delta^2 q_+ > 1$, indicating that phase correlations are being degraded and with good indication that the reason are thermal vibrations in the crystal lattice.

The analysis of the tripartite correlations indicated that indeed an improvement is obtained by lowering the crystal temperature and investigations of the coupling of the pump with phonon noise indicated that an optimal temperature of operation for our OPO is around $-40\,°\mathrm{C}$. These results led us to drive our efforts into improving the cooling system. Several attempts were made until we finally arrived at a configuration that used synthetic air, with very low levels of humidity, and a cooled copper fork that is used as cold trap for the particles approaching the crystal surface. This solution allowed us to have a stable OPO at $-21\,°\mathrm{C}$.

With the cooling system working we prepared the rest of the system and took some preliminary measurements that were presented in the last chapter. Those measurements were supposed to function simply as a sanity test for the system, to check if all of its components were functioning properly after the long idle period and after the continuous reassembly of the OPO cavity. Those results were not very good, but they showed us that the system was ready for taking measurements. They also showed us that we needed to work on the amplitude stabilization of the pump beam, either by improving the parameters of the Ti:Sapph laser or by introducing a noise eater. These were supposed to be our next steps, and after that, taking measurements at negative temperatures.

For the next part of this work will focus on the coupling between light and an atomic ensemble. There we describe how we can use light in the preparation and characterization of an atomic polarization state that can be used in quantum information protocols. All the experiments and measurements regarding part III were performed at the Niels Bohr Institute in Denmark.

Part III

Preparing and Characterizing an Atomic Polarization State

8 INTRODUCTION

We wanted to get an understanding on how to prepare and measure an atomic polarization state so that we would be able to interact the entangled fields generated in our OPO with an atomic cloud at room temperature. The final goal would be the implementation of quantum information protocols, such as teleportation, between systems that interact with light at different wavelengths.

To achieve this purpose, we took part on a project to develop an atomic system to be used as a negative mass reference frame in an experiment to overcome the standard quantum limit in gravitational wave detectors through backaction cancellation (Khalili and Polzik, 2018; Zeuthen *et al.*, 2019). This project was implemented at the Niels Bohr Institute under the supervision of professor Eugene Polzik.

In this chapter we begin by creating context in explaining the importance of gravitational-wave astronomy to physics and especially to cosmology. We then proceed to point out the relevance of increasing the detection efficiency of these waves and how it is becoming limited by quantum effects. We then introduce the proposal to overcome this limit presented in Khalili and Polzik (2018), which sets the main motivation for the project.

8.1 Motivation

The detection of gravitational waves by the LIGO and Virgo observatories opened a new range of research possibilities in the areas of astrophysics and cosmology (The LIGO Scientific Collaboration and the Virgo Collaboration, 2016). The measurements performed by these observatories made possible to detect the collisions between two black holes and two neutron stars and realize that these phenomena are not as rare as imagined.

The sensitivity required to detect gravitational waves was only achieved by exploiting the fact that interferometric processes are extremely sensitive to small variations in the lengths of the interferometer arms. When a gravitational wave passes, one arm stretches and the other arm contracts because of the space-time fluctuations caused by its passage. This change in arm length results in a small change in the signal strength at the interferometer output.

The sensitivity of these detectors is limited by the noise of a variety of sources. Mechanical noise, such as seismic noise, and thermal noise, are circumvented by extremely advanced stabilization systems. Thus, these detectors are limited by quantum effects and shot noise becomes relevant.

The effect of shot noise on the detected photocurrent decreases with the increase in laser power (Pitkin *et al.*, 2011). However, increasing laser power means increasing the noise due to radiation pressure, also called Quantum Backaction (QBA). This noise arises because of the uncertainty on the amplitude quadrature of the field inside the interferometer and is propagated to the mirror due to the transfer of momentum between the laser and the mirror.

There is an optimal laser power that minimizes the effect of these two uncorrelated sources of noise. This limit of sensitivity is known as the Standard Quantum Limit and is analogous to the Heisenberg Uncertainty Principle for the phase and amplitude quadratures of the field.

The measurement sensitivity of the motion of a free mass in a quantum reference system with negative effective mass is not limited by the noise introduced by the QBA. This is so because in such a reference frame it is possible to perform the measurement in terms of two commuting quadratures, the relative position $(\hat{q} - \hat{q}_0)$ and the sum of momenta $(\hat{p} + \hat{p}_0)$. To do so, it is possible to use an atomic ensemble with their spin prepared in a way to simulate a harmonic oscillator with negative mass and then carry out the desired measurement with respect to that reference frame (Møller, 2018).

With that in mind, Khalili and Polzik (2018) propose a measurement capable of overcoming the effects of QBA on the mirrors of gravitational wave detectors. According to them, the mirrors of

these detectors have technical parameters that allow them to be considered free masses in the analysis frequencies of interest. They suggest the use of a Cesium cell with well-defined global spin to be used as reference frame in the measurement of the motion of the mirrors of the gravitational wave detectors.

In order to achieve this objective, the proposed system will use frequency sum generation and parametric down conversion in an optical parametric oscillator (OPO) to generate entangled fields that will be used to interact an atomic ensemble and the mirror of the gravitational wave detector. The entanglement between the two fields, and an adjustment in the frequency of these oscillators, allows the cancellation of the shot noise and QBA terms in the joint measurement. In this way the detector can reach sensitivities beyond the standard quantum limit.

Next we will give a brief overview of some of the concepts in Khalili and Polzik (2018) that, we understand, motivate the current project.

8.1.1 Negative mass reference frame

It has been shown that that negative mass oscillators can be used in noise cancellation schemes that allow measurements with precision beyond the standard quantum limit (Tsang and Caves, 2010, 2012). In a negative mass oscillator, creating a quantum of energy involves the extraction of energy by an amount $\hbar\omega$. Essentially, it works the same way as a positive mass oscillator, but the ladder of energy levels runs down instead of up.

To understand why to use these oscillators as a reference frame, let us start by considering a harmonic oscillator with frequency ω:

$$\hat{q}(t) = \hat{q}(0)\cos\omega t + \hat{p}(0)\frac{1}{m\omega}\sin\omega t, \tag{8.1}$$

where $\hat{q}(t)$ is the position of the mass m in an arbitrary time t and $\hat{q}(0)$ and $\hat{p}(0)$ its initial position and momentum respectively. Since the operators $\hat{q}(0)$ and $\hat{p}(0)$ do not commute, it is not possible to accurately describe the position of the mass in an arbitrary time.

We can, however, work around this problem by considering a second quantum oscillator with mass m_0, position $\hat{q}_0(t)$ and momentum $\hat{p}_0(t)$, with the same natural frequency ω. In the case where we consider a negative mass, as exotic as it can be, we may arrive at an interesting condition:

$$\hat{q}(t) - \hat{q}_0(t) = [\hat{q}(0) - \hat{q}_0(0)]\cos\omega t + [\hat{p}(0) + \hat{p}_0(0)]\frac{1}{m\omega}\sin\omega t. \tag{8.2}$$

Since the quadratures $\hat{q}(0)-\hat{q}_0(0)$ and $\hat{p}(0)+\hat{p}_0(0)$ commute, the precision of a simultaneous measurement in that reference frame is not limited by the uncertainty principle, and therefore the relative measurement of these quantities can be as precise as desired. These two quadratures form a typical EPR pair, which already gives a glimpse that to avoid QBA one can use two entangled oscillators.

Now that we know why to use a negative mass oscillator as a reference frame, we go back to the question about how an atomic spin system can be used for such purposes.

8.1.2 Atomic spin as negative mass reference frame

Consider an atomic ensemble in the presence of optical pumping and a magnetic field. An atomic spin state in the presence of a magnetic field undergoes the separation of its energy levels due to the Zeeman effect, and in the present case, the optical pumping has the role of keeping the system at highest Zeeman sub-level. The system is prepared in such a way that the total spin is polarized in the negative x direction, while the magnetic field $\mathbf{B}$ is oriented in the positive x direction (Figure 8.1(a)).

Another effect that rises from the interaction of the total spin with the magnetic field is the Larmor precession. In this configuration the Hamiltonian of the system is given by (Khalili and Polzik,

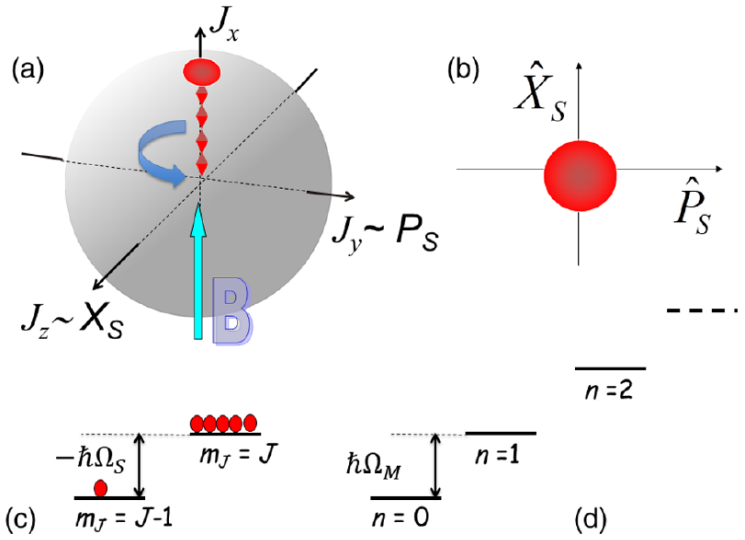

Figure 8.1: Macroscopic spin oscillator. (a) Total spin of an atomic ensemble in a magnetic field represented as a vector in the Bloch sphere. (b) Normalized spin components orthogonal to the mean direction and equivalent to canonical operators. (c) For the geometry presented in (a), the first excited state of a spin oscillator has lower energy than the non-excited state, corresponding to a negative mass oscillator. (d) Spectrum of a mechanical oscillator. *Reprinted from* Khalili and Polzik (2018).

2018):

$$\hat{H}_S = \hbar\Omega_S J_x - \frac{\hbar\Omega_S}{2}\left(\hat{X}_S^2 + \hat{P}_S^2\right), \tag{8.3}$$

where Ω_S is the Larmor frequency associated with the precession of the total spin around the x direction, $J_x = |\langle \hat{J}_X \rangle|/\hbar \gg 1$ is the average projection of that spin in the same direction, and $\hat{X}_S = \hat{J}_z/\hbar\sqrt{J}_X$ and $\hat{P}_S = -\hat{J}_y/\hbar\sqrt{J}_X$ canonical variables written in terms of the other two projections (Figure 8.1(b)), such that $[\hat{X}_S, \hat{P}_S] = i$.

We can see that the second term of the Hamiltonian in Equation (8.3) is equivalent to a mechanical oscillator with negative effective mass, since the first excited state of the spin oscillator would correspond to an energy smaller than the energy of the non-excited state (Figure 8.1(c)). Under these conditions an atomic spin can be considered an oscillator with negative mass.

8.1.3 Avoiding the effects of QBA

We will now see how in this reference frame one can make the effects of QBA and shot noise cancel out in the combined measurement. Consider a lossless system such that the frequency Ω is much smaller than the bandwidth of the interferometer $\Gamma_I = 2\kappa_I$[1]. The phase quadrature $\hat{b}_I^s$ of the interferometer's output field, measured in the homodyne detector D_I (blue arm in Figure 8.2), is given by (Khalili and Polzik, 2018):

$$\hat{b}_I^s = \hat{a}_I^s + \frac{2\Theta\chi}{\kappa_I}\hat{a}_I^c + \sqrt{\frac{2\Theta}{\kappa_I}}\chi\frac{F_S + F_T}{\sqrt{\hbar m}}, \tag{8.4}$$

where $\hat{a}_I^s$ and $\hat{a}_I^c$ represent the phase and amplitude quadratures, respectively, of the field operator in the interferometer, Θ the normalized optical power[2], χ the mechanical susceptibility of the mirrors of the gravitational wave detector, F_S the gravitational wave signal strength, and F_T the sum of the other sources of noise (thermal, seismic, etc.). Note that in Equation 8.4, the second term is proportional to

[1] For the Advanced LIGO inteferometer: $\kappa_I = 2\pi \times 500\,\text{Hz}$ (Khalili and Polzik, 2018).

[2] $\Theta = 8\omega_0 I_c/mcL$, where I_c is the optical power circulating in each of the arms of the interferometer, L the arm length and c the speed of light.

the optical power Θ, which means that an increase in light intensity translates into an increase in noise associated with the amplitude of the field in the interferometer, in other words QBA.

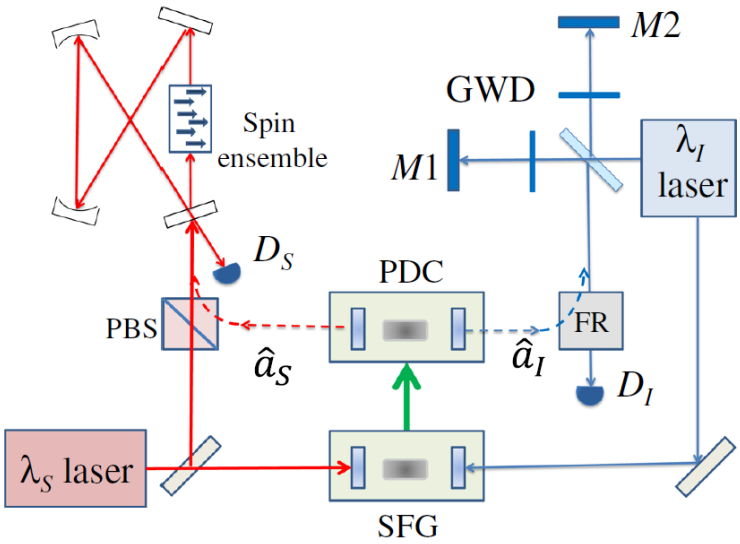

Figure 8.2: Schematic representation of the setup. Sum-Frequency Generation (SFG) and Parametric Down Conversion (PDC) are responsible for entangling the fields $\hat{a}_S$ and $\hat{a}_I$ that will interact respectively with the atomic ensemble and the mirror of the gravitational-wave detector. *Reprinted from* Khalili and Polzik (2018).

However, the phase quadrature of the field coming from the interaction between light and spin and measured in homodyne detection D_S (red arm of Figure 8.2) can be described as:

$$\hat{b}_S^s = \hat{a}_S^s + 2\Omega_S\Gamma_S\chi_S\hat{a}_S^c + \sqrt{2\Omega_S\Gamma_S}\chi_S\hat{f}_S, \tag{8.5}$$

where $\hat{a}_S^s$ and $\hat{a}_S^c$ represent, respectively, the phase and amplitude quadratures of the light modes after interacting with the atomic spin, Γ_S the spin oscillator readout rate, χ_S its effective susceptibility, and $\hat{f}_S$ the normalized thermal force acting on the spin.

The second term of Equation 8.5 can be adjusted by controlling the intensity of the magnetic field $\mathbf{B}$, since the value of Ω_S depends on the amplitude of that field. This ability to adjust the Larmor frequency along with the entanglement between the fields is what allows to overcome the Standard Quantum Limit.

Consider the case where the fields are perfectly entangled, $\hat{a}_I^s = -\hat{a}_S^s$ and $\hat{a}_I^c = \hat{a}_S^c$. If the response of the spin system with negative effective mass equals the interferometer response

$$\frac{\Theta\chi}{\kappa_I} = -\Omega_S\Gamma_S\chi_S, \tag{8.6}$$

the effects of shot noise and QBA on the joint measurement $(\hat{b}_I^s + \hat{b}_S^s)$ cancel out, resulting in a response that is no longer limited by these quantum sources of noises. This can only be achieved because, as already mentioned, it is possible to adjust the Larmor frequency by tuning the amplitude of the magnetic field.

The example presented above is ideal, since it disregards losses and considers that the fields are perfectly entangled. Under realistic conditions the proposed system should be capable of improving the sensitivity of gravitational wave detectors by 6 dB within the frequency spectrum of interest (Khalili and Polzik, 2018).

9 THEORETICAL DESCRIPTION

In this chapter we describe how we can use lasers to optically pump an atomic ensemble in order to prepare an atomic spin polarization state. We begin it with a brief review of the level structure of Cesium 133, to set a starting point for the theory of optical pumping. The chapter ends with the theory of the Magneto-Optical Resonance Signal (MORS), the technique used to characterize an atomic polarization state.

9.1 Atomic Structure of Cs 133

The choice of Cesium 133 (^{133}Cs) as our atomic ensemble is for the most part a practical one. Cesium has the advantage of having a single stable isotope while rubidium has two (^{85}Rb and ^{87}Rb). Also, a high atomic density combined with the quality of the anti-reflective coatings at the relevant wavelengths and paraffin coatings to preserve spin polarization allow the fabrication of high quality cesium cells. Narrow band diode lasers compatible with D1 and D2 transitions of Cs have been readily available for a while now and the group at the NBI has a long history of working with Cs atoms (Julsgaard *et al.*, 2001, 2004; Krauter *et al.*, 2011, 2013).

Before we take a closer look at the Cesium atom we are going to present a brief theoretical review. We have no intention, however, to be comprehensive in this review. The idea is to introduce the formalism and some key concepts to better understand the discussions that follow (for a more in depth description we recommend Cohen-Tannoudji *et al.* (1991)).

We begin by considering the observables L_x, L_y and L_z, components of the angular momentum $\mathbf{L}$ which satisfy the following commutation relations:

$$\begin{aligned} [L_x, L_y] &= i\hbar L_z, \\ [L_y, L_z] &= i\hbar L_x, \\ [L_z, L_x] &= i\hbar L_y, \end{aligned} \tag{9.1}$$

and the observable $\mathbf{L}^2 = L_x^2 + L_y^2 + L_z^2$, such that:

$$\left[\mathbf{L}^2, L_i\right] = 0, \quad i = \{x, y, z\}. \tag{9.2}$$

We are interested in writing a basis formed by simultaneous eigenkets of $\mathbf{L}^2$ and L_z. It can be shown that the set $\{|l, m_l\rangle\}$ can be found to be such a basis. Let us consider how $\mathbf{L}^2$ and L_z operate on the elements of this set:

$$\begin{aligned} \mathbf{L}^2 |l, m_l\rangle &= \hbar^2 l(l+1) |l, m_l\rangle , \\ L_z |l, m_l\rangle &= \hbar m_l |l, m_l\rangle , \end{aligned} \tag{9.3}$$

where l can only be positive integers, half-integers or zero; and for a given value of l the allowed values of m_l are the $2l+1$ numbers such that $-l \leq m_l \leq l$ and m_l varies in increments of 1 $(-l, -l+1, \ldots, l-1, l)$. Since the kets $\{|l, m_l\rangle\}$ span the entire spectrum of the observables $\mathbf{L}^2$ and L_z and since they obey the orthogonality and closure relations:

$$\langle l, m_l | l', m_l' \rangle = \delta_{ll'} \delta_{m_l m_l'} \tag{9.4}$$

$$\sum_l \sum_{m_l=-l}^{l} |l, m_l\rangle \langle l, m_l| = \mathbb{1} \tag{9.5}$$

we can say that $\{|l, m_l\rangle\}$ form a basis for the state space.

However, in physics, and specially in atomic physics, we usually need to consider the effect of more than one angular momentum at the same time. This is what happens for instance when we want to consider simultaneously the effect of the orbital angular momentum and the electron spin in the atomic energy levels.

9.1.1 Addition of angular momentum

We now consider two angular momenta $\mathbf{J_1}$ and $\mathbf{J_2}$ such that

$$\mathbf{J_i}^2 |j_i, m_i\rangle = \hbar^2 j_i(j_i+1) |j_i, m_i\rangle , \quad i = \{1, 2\} \tag{9.6}$$

$$J_{iz} |j_i, m_i\rangle = \hbar m_i |j_i, m_i\rangle , \quad i = \{1, 2\}, \tag{9.7}$$

give the eigenvalues of each individual observable.

A global basis for the system is obtained from the tensor product between the basis kets of each individual subsystem

$$|j_1, m_1, j_2, m_2\rangle = |j_1, m_1\rangle \otimes |j_2, m_2\rangle . \tag{9.8}$$

This is usually referred to as the uncoupled basis, since it is an eigenbasis of the individual observables $\mathbf{J_1}^2$, J_{1z}, $\mathbf{J_2}^2$, J_{2z}. But we can also write what is known as the coupled basis, by defining the operator $\mathbf{J} = \mathbf{J_1} + \mathbf{J_2}$:

$$|J, M\rangle \equiv |j_1, j_2, J, M\rangle , \tag{9.9}$$

which is an eigenbasis of the coupled observables $\mathbf{J_1}^2$, $\mathbf{J_2}^2$, $\mathbf{J}^2$, J_z, where $\mathbf{J}^2 = \mathbf{J_1}^2 + \mathbf{J_2}^2 + 2\mathbf{J_1} \cdot \mathbf{J_2}$ and $J_z = J_{1z} + J_{2z}$.

In the coupled basis the spectra of $\mathbf{J}^2$ and J_z are:

$$\mathbf{J}^2 |J, M\rangle = \hbar^2 J(J+1) |J, M\rangle , \tag{9.10}$$

$$J_z |J, M\rangle = \hbar M |J, M\rangle , \tag{9.11}$$

where $M \in \{-J, -J+1, \ldots, J-1, J\}$ and the total angular momentum quantum number J must satisfy

$$|j_1 - j_2| \leq J \leq j_1 + j_2. \tag{9.12}$$

This new basis is convenient for the description of systems where there is coupling between the angular momenta J_1 and J_2 in the Hamiltonian, which is the case of atomic systems.

9.1.2 Clebsch-Gordan Coefficients

Now let us consider how to represent elements of the coupled basis in the uncoupled basis. To do that we start with the elementary statement that the operation of the identity on a ket results in the ket itself:

$$|J, M\rangle = \mathbb{1} |J, M\rangle . \tag{9.13}$$

Since the eigenkets in equation 9.8 form a basis for the state space it must also have a closure relation similar to the one in equation 9.5. Hence, we find that

$$|J, M\rangle = \sum_{m_1=-j_1}^{j_1} \sum_{m_2=-j_2}^{j_2} |j_1, m_1, j_2, m_2\rangle \langle j_1, m_1, j_2, m_2 | J, M\rangle . \tag{9.14}$$

The matrix elements $\langle j_1, m_1, j_2, m_2 | J, M\rangle$ are called Clebsch-Gordan Coefficients and they are non-zero only if the triangular relation 9.12 is satisfied and

$$M = m_1 + m_2. \tag{9.15}$$

These are going to be relevant because we will be able to establish selection rules when we discuss the dipole interaction and atomic transitions.

9.1.3 Selection rules and allowed transitions

We want to describe the dipole transition from the ground state to the excited state $F \rightarrow F'$, where we define the primed notation to refer to the exited state. Let us consider specifically the matrix elements that couple the energy levels, in the basis of total angular momentum, through the dipole interaction: $\langle F, m_F|\epsilon \cdot \mathbf{r}|F', m_{F'}\rangle$, where ϵ is the polarization of the incident light and $\mathbf{r}$ the dipole moment of the atom Seltzer (2008).

Using the Wigner-Eckart theorem (Cohen-Tannoudji *et al.*, 1991) we can write these matrix elements as a product of a reduced matrix element (which is independent of the angular momentum orientation m_F) and a Clebsch-Gordan coefficient:

$$\langle F, m_F|\epsilon\, r_q|F', m_{F'}\rangle = \langle F||\epsilon \cdot \mathbf{r}||F'\rangle \, \langle F, m_F|F', m_{F'}, 1, q\rangle \,, \tag{9.16}$$

where $\epsilon\, r_q$ designates the q-th component of the operator $\epsilon \cdot \mathbf{r}$. If the Clebsch-Gordan coefficients do not satisfy the triangular relation 9.12 and equation 9.15, their value is zero. This implies the following selection rules for the dipole transition in equation 9.16:

$$\begin{cases} F - F' = \{-1, 0, +1\}, \\ q = m_F - m_{F'}. \end{cases} \tag{9.17}$$

With these selection rules we can easily determine the allowed dipole transitions when we consider the optical pumping of our atomic sample.

9.1.4 Fine structure and hyperfine structure of Cesium 133

Now we have the fundamental tools required to describe the atomic structure of Cs 133. Being an alkali atom, Cs has a single electron in the valence band and its ground state is represented in the spectroscopic notation as $6\,^2S_{1/2}$. When considering only the fine structure ($J = L + \mathcal{S}$) for the ground state, the coupling between the orbital angular momentum $L = 0$ and the electron spin $\mathcal{S} = 1/2$ results in a total angular momentum $J = 1/2$. The fine structure of the excited state $6P$ ($L = 1$) leads to two possibilities, the first $6\,^2P_{1/2}$ is associated with the $D1$ transition from the ground state and the second $6\,^2P_{3/2}$ with the $D2$ transition, as shown in figure 9.1.

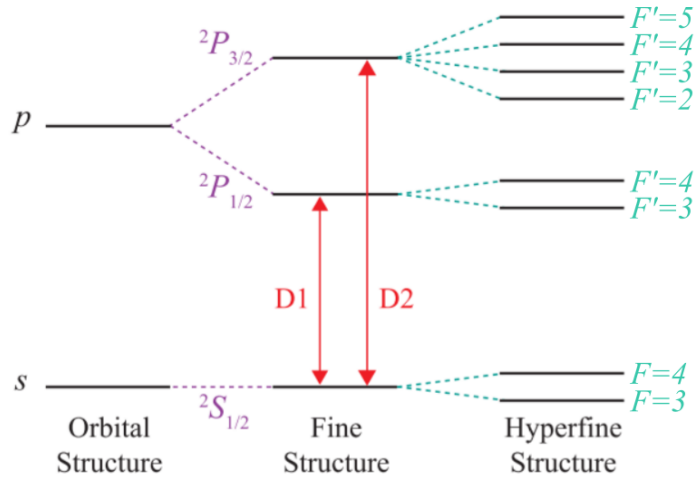

Figure 9.1: Fine structure and hyperfine structure of Cesium 133. The D1 line indicates the $6S_{1/2} \longrightarrow 6P_{1/2}$ transition and the D2 line indicates the $6S_{1/2} \longrightarrow 6P_{3/2}$ transition. *Adapted from* Seltzer (2008).

The hyperfine structure ($F = I + J$) comes into play when we in addition consider the coupling with the nuclear spin ($I = 7/2$ for Cs 133), giving rise to the hyperfine splitting of the energy levels both in the exited state and in the ground state. For the ground state $6\,^2S_{1/2}$, the energy levels split into $F = \{3, 4\}$ and for the exited state, $6\,^2P_{1/2}$ splits into $F' = \{3, 4\}$ and $6\,^2P_{3/2}$ splits into $F' = \{2, 3, 4, 5\}$. The hyperfine structure of Cs is also presented in figure 9.1.

As already stated in section 8.1.2, the presence of a magnetic field $\mathbf{B}$ will break the degeneracy of the m_F sublevels and split the energy levels even further along the quantization axis due to the Zeeman effect. The energy of the splitting is proportional to the magnetic field and since the contribution of $\mathbf{B}$ to the Hamiltonian can be written to be $\hbar\Omega_s J_x$, we find that the energy splitting is proportional to the Larmor frequency Ω_s. The sign of the splitting depends on the hyperfine level, the Zeeman sublevel and also on the strength of the magnetic field. This behavior is depicted for the ground state of Cesium ($I = 7/2$) in figure 9.2, where we can see the splitting of the Zeeman sublevels as a function of the magnetic field intensity.

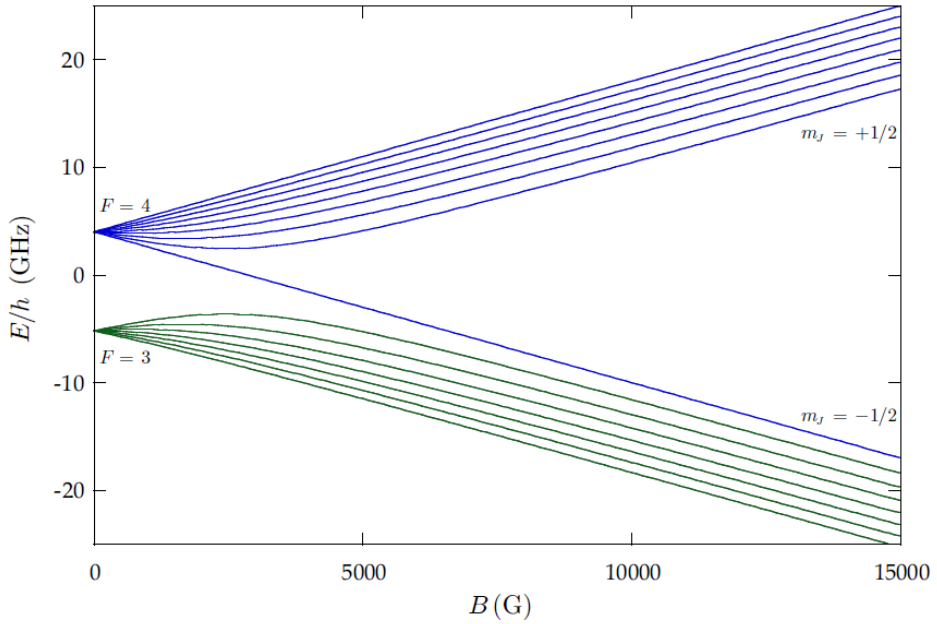

Figure 9.2: Zeeman splitting of the m_F sublevels for the ground state of Cesium 133 as a function of the intensity of the magnetic field. *Reprinted from* Steck (2019).

9.2 Preparing an Atomic Polarization State: Optical Pumping

In this section we will not focus on the theory of optical pumping but rather briefly explain its consequences in our system and what we hope to achieve with it. A review on the subject can be found in Happer and Van Wijngaarden (1987) and in more detail in HAPPER (1972).

For the reasons given in section 8.1, we want to prepare a polarization state such that almost all the population lies in a specific Zeeman level, and optical pumping is the tool for the job. The idea behind it is to use resonant scattering of photons to transfer some order to an atomic sample, in our case, to make sure almost all atoms are in the $|F = 4, m_F = 4\rangle$ state.

The pumping method used in our system is called *depopulation pumping* and it consists on reducing the population of one or more sublevels through selective excitation. Circularly polarized photons (σ_+), for instance in the D1 line, propagating along the $\hat{z}$ axis have angular momentum $+1$ in units of the electro-spin angular momentum $\hbar$. If an atom in the $m_s = -1/2$ sublevel of the $^2S_{1/2}$ ground state

absorbs one of these photons, conservation of angular momentum will require the atom to absorb the photon's angular momentum exiting it to the $m_s = +1/2$ sublevel of the $^2P_{1/2}$ state. Nonetheless, if the atom in the $m_s = +1/2$ of the ground state, it is forbidden to absorb the photon because there is no level with an additional unit of angular momentum in the excited state ($m_s = +3/2$).

In our case we want to completely deplete the $F = 3$ state and all the m_F sublevels in $F = 4$, with the exception of $m_F = 4$. To do that we use a pump laser with σ_+ polarization tuned at the D1 transition. This laser will excite the atom from $|F = 4, m_F\rangle$ to $|F' = 4, m_{F'} + 1\rangle$. Once it decays, selection rules only allow decay to m_F sublevels such that $m_{F'} - m_F = 0, \pm 1$. Therefore it can decay at worst back to $|F = 4, m_F\rangle$ but most of the time it will decay to $m_F + 1$ or $m_F + 2$, making it more likely to transition to higher levels. Once the atom is at $|F = 4, m_F = 4\rangle$ it does not move further, since this is a dark state, as shown in the $D1$ line (left part) of figure 9.3.

The repump is used to deplete the $F = 3$ hyperfine level. It does it by exciting the atoms from $F = 3$ to, for example, $F' = 4$ and upon decaying the atom can go back to $F = 3$ or it can go to $F = 4$ where it gets under the effect of the pump. If it goes back to $F = 3$ it is re-excited, even if it as at the highest level $|F = 3, m_F = 3\rangle$, since this is not a dark state and can transition to $|F' = 4, m_{F'} = 4\rangle$, through a σ_+ excitation, as seen in the $D2$ line (right part) of figure 9.3. Using a σ_+ polarization in the repump also increases the probabilities of preparing $|F = 4, m_F = 4\rangle$ by the same mechanism described for the pump.

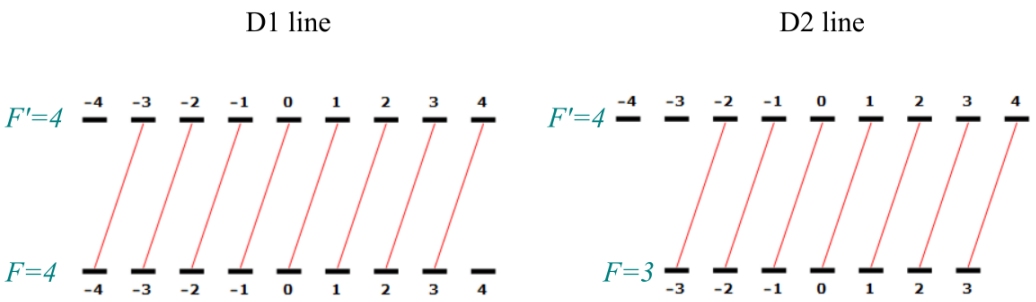

Figure 9.3: Transitions from the ground state to the exited state for a laser with σ_+ polarization. Selection rules only allow decay to m_F sublevels such that $m_{F'} - m_F = 0, \pm 1$. Since $m_F = 4$ is a dark state the pump laser makes sure the atoms stay in this state. The repump laser uses the $D2$ transition to transfer atoms from $F = 3$ to $F = 4$. Pump @ 894 nm (left) and repump @ 852 nm (right).

9.3 Spin Characterization

9.3.1 The Magneto-Optical Resonance Signal: MORS

An atomic ensemble in a constant magnetic field ($\mathbf{B}_{bias}$) will have the degeneracy of the m_F Zeeman sublevels broken by a factor that is proportional to the Larmor precession frequency (to first order). It is possible to obtain information about spin orientation, coherence time and number of atoms in the ensemble, by inducing weak transitions among the Zeeman sublevels using a radio frequency magnetic field ($\mathbf{B}_{RF}$). The technique used to do that is called the *magneto-optical resonance signal* or *MORS* and our description of it will follow Julsgaard (2003).

The contribution to the Hamiltonian of the system introduced by the coupling of the magnetic field ($\mathbf{B}$) with the atomic total angular momentum ($\mathbf{F}$) is given by:

$$\hat{H} = g_F \, \mu_B \, \mathbf{F} \cdot \mathbf{B} + \mathcal{O}(B^2), \tag{9.18}$$

where g_F is the total angular momentum g-factor, μ_B is the Bohr magneton and we have added a second order correction in the magnetic field due to the quadratic Zeeman Effect (Julsgaard, 2003) that will be taken into account further ahead.

We can describe the spin state of the k-th Cesium atom in the ground state F by the density operator $\hat{\sigma}^{(k)}$ whose matrix elements are given by:

$$\hat{\sigma}_{ij}^{(k)} = |i\rangle_k \langle j|_k \,, \tag{9.19}$$

where $i, j = \{-F, -F+1, \ldots, F-1, F\}$. For the atomic ensemble we sum over the N atoms:

$$\hat{\sigma}_{ij} = \frac{1}{N} \sum_k \hat{\sigma}_{ij}^{(k)} = \frac{1}{N} \sum_{k=1}^{N} |i\rangle_k \langle j|_k \,. \tag{9.20}$$

Choosing the x-axis as the quantization axis (as in fig 8.1), the components of the angular momentum operator can be written in terms of the density operator as:

$$\hat{F}_x = N \sum_{m=-F}^{F} m\, \hat{\sigma}_{m,m}, \tag{9.21}$$

$$\hat{F}_y = N \sum_{m=-F}^{F-1} \frac{C(F,m)}{2} \left\{\hat{\sigma}_{m+1,m} + \hat{\sigma}_{m,m+1}\right\}, \tag{9.22}$$

$$\hat{F}_z = N \sum_{m=-F}^{F-1} \frac{C(F,m)}{2i} \left\{\hat{\sigma}_{m+1,m} - \hat{\sigma}_{m,m+1}\right\}, \tag{9.23}$$

where we define $m \equiv m_F$ to simplify the notation and $C(F,m) = \sqrt{F(F+1) - m(m+1)}$.

If we consider, as in figure 9.4, the bias magnetic field B_{bias} in the x direction and the radio frequency magnetic field B_{RF} in the y direction with frequency ω, the contribution of both fields to Hamiltonian 9.18 is given by:

$$\hat{H} = g_F\, \mu_B\, \hat{F}_x\, B_{bias} + \mathcal{O}(B_{bias}^2) + g_F\, \mu_B\, \hat{F}_y\, |B_{RF}| \cos(\omega t + \phi). \tag{9.24}$$

Substituting the components of angular momentum in equations 9.21 to 9.23, and using the rotating wave approximation, we may write the Hamiltonian entirely in terms of the density operator:

$$\hat{H} = \sum_{m=-F}^{F} \hbar\omega_m \hat{\sigma}_{m,m} + \frac{g_F \mu_B}{4} \sum_{m=-F}^{F-1} C(F,m) \left\{B_{RF}\, \mathrm{e}^{-i\omega t}\, \hat{\sigma}_{m+1,m} + B_{RF}^{*}\, \mathrm{e}^{i\omega t}\, \hat{\sigma}_{m,m+1}\right\}, \tag{9.25}$$

where $\hbar\omega_m = g_F \mu_B\, m\, B_{bias}$ indicates the contribution of the bias magnetic field since, by distinguishing the energy of each sublevel, we are taking into account the second order correction responsible for making the separation of the Zeeman sublevels unequal. The separation between two adjacent lines ν_{QZ} caused by the quadratic Zeeman effect is given by (Julsgaard *et al.*, 2004):

$$\nu_{QZ} = \frac{2\nu_L^2}{\nu_{\mathrm{hfs}}}, \tag{9.26}$$

where ν_L is the first order correction given by

$$h\nu_L \equiv \frac{-\mu_J/J}{2I+1} \tag{9.27}$$

such that μ_J is the magnetic moment of the electron, J is the angular momentum of the outer most electron, I is the nuclear spin. Also, the hyperfine splitting ν_{hfs} is related to the strength of the magnetic dipole interaction between the electronic and nuclear spin (a) as $h\nu_{\mathrm{hfs}} = (ha/2)(2I+1)$.

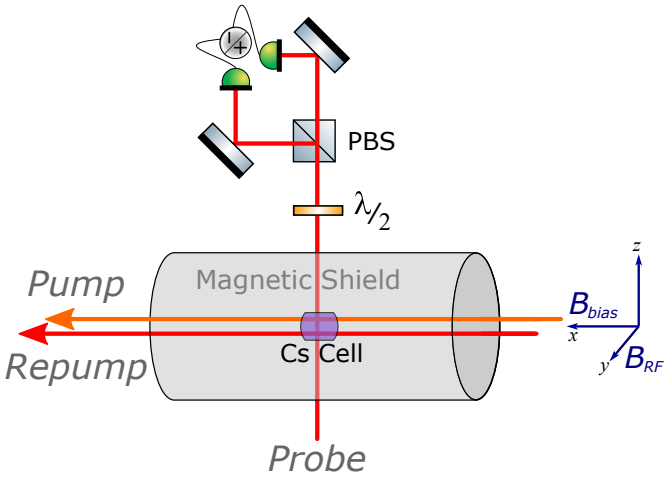

Figure 9.4: Schematic representation of the setup for the experiments with a 5mm cubic Cs cell inside the magnetic shield.

With the Hamiltonian 9.25 we can calculate the time evolution of the of the matrix elements of the density operator:

$$\frac{\partial}{\partial t}\hat{\sigma}_{ij} = \frac{1}{i\hbar}\left[\hat{\sigma}_{ij}, \hat{H}\right] + \text{decay terms.} \tag{9.28}$$

Assuming the difference between the populations $\hat{\sigma}_{i,i}$, and $\hat{\sigma}_{i+1,i+1}$ to be approximately constant in time and decay processes in the populations to be compensated by external pumping, we can allow for the transient solutions to vanish. With these assumptions we can find the steady state solution and write the the angular momentum components $\hat{F}_y$ and $\hat{F}_z$ not in terms of the coherences as in equations 9.22 and 9.23 but in terms of the differences of the populations between two consecutive Zeeman levels (Julsgaard *et al.*, 2004):

$$\hat{F}_y = \text{Re}\left\{\frac{ig_F\mu_B B_{RF} N}{4\hbar}\sum_{m=-F}^{F-1}\frac{[F(F+1)-m(m+1)]\,e^{i\omega t}}{i\,(\omega_{m+1,m}-\omega)-\Gamma_{m+1,m}/2}\left[\hat{\sigma}_{m+1,m+1}-\hat{\sigma}_{m,m}\right]\right\}, \tag{9.29}$$

$$\hat{F}_z = \text{Im}\left\{\frac{ig_F\mu_B B_{RF} N}{4\hbar}\sum_{m=-F}^{F-1}\frac{[F(F+1)-m(m+1)]\,e^{i\omega t}}{i\,(\omega_{m+1,m}-\omega)-\Gamma_{m+1,m}/2}\left[\hat{\sigma}_{m+1,m+1}-\hat{\sigma}_{m,m}\right]\right\}, \tag{9.30}$$

where $\Gamma_{m+1,m}$ is the linewidth of the Lorentzian response of the two-level system composed by the two adjacent Zeeman sublevels m and $m+1$.

The probe laser is linearly polarized along the z-direction and will undergo polarization rotation proportional to the spin $\hat{F}_y$ along the y-axis. By using a half waveplate and a PBS we can balance the two photodetectors such that their difference signal is proportional to the polarization rotation. The mean value of the atomic spins $\hat{F}_y$ will be zero, and no polarization rotation in the probe laser will be measured, unless an RF magnetic field is applied transversely to the static magnetic field. In our experiment we get the *MORS* signal from the photocurrent by using a lock-in amplifier to decompose it in its sine and cosine components and making the sum of their squared amplitudes to give $i(t) = \text{const}\cdot|A(\omega)|^2$, where $A(\omega)$ is the mean value of the curly brackets in equation 9.30. We then obtain the information about the populations by fitting

$$\text{MORS}(\omega) = \text{const}\cdot\left|N\sum_{m=-F}^{F-1}\frac{[F(F+1)-m(m+1)]}{i\,(\omega_{m+1,m}-\omega)-\Gamma_{m+1,m}/2}\left\langle\hat{\sigma}_{m+1,m+1}-\hat{\sigma}_{m,m}\right\rangle\right|^2 \tag{9.31}$$

to the experimental data. We see from equation 9.31 that the MORS signal is a sum of the complex amplitudes of Lorentzian functions, which is why the characteristic MORS signal has many peaks, as we

shall see in chapter 11. We can calculate the spin orientation (p) through

$$p = \frac{1}{F}\sum_{-F}^{F} m \cdot \langle \hat{\sigma}_{m,m} \rangle \,. \tag{9.32}$$

The MORS technique described in this section can be used as a tool to measure the atomic populations of the Zeeman sublevels. By using this information in equation 9.32 we can calculate the spin orientation which provides a characterization of the collective spin system. The quality of the prepared spin is essential for the backaction cancellation in gravitational-waves. This scheme is extremely sensitive to noise, especially at low frequencies and the closer the orientation is to one ($p = 1$) the closer the spin system is to a coherent state. A coherent spin state would provide the smallest average projection of J_x into the J_y and J_z components as seen in figure 8.1(b).

10 EXPERIMENTAL IMPLEMENTATION AND METHODS

This chapter begins with the description of our experimental implementation for the optical pumping. Afterwards we talk about saturated absorption spectroscopy and polarization spectroscopy, the tools we use to lock our lasers at a frequency that will preferentially induce the desired transitions. We then proceed to the MORS setup, for the characterization of the prepared polarization state.

10.1 Optical Pumping Setup

We start by describing our experimental setup for the optical pumping and explain how we generate the signal to lock them at the desired atomic transitions.

10.1.1 Setup

For the experimental implementation of the optical pumping we use two diode lasers placed on a breadboad for portability. The bottom one in figure 10.1, acting as the pump, is a Toptica DFB[1] diode laser and it is locked to the Cesium $D1$ line (@894 nm). The top laser is a Toptica DL Pro diode laser and is locked to the $D2$ line acting as the repump in our setup (@852 nm). Both of them have their beams with an elliptical profile and are sent though a pair of anamorphic prisms to correct for their respective ellipticities.

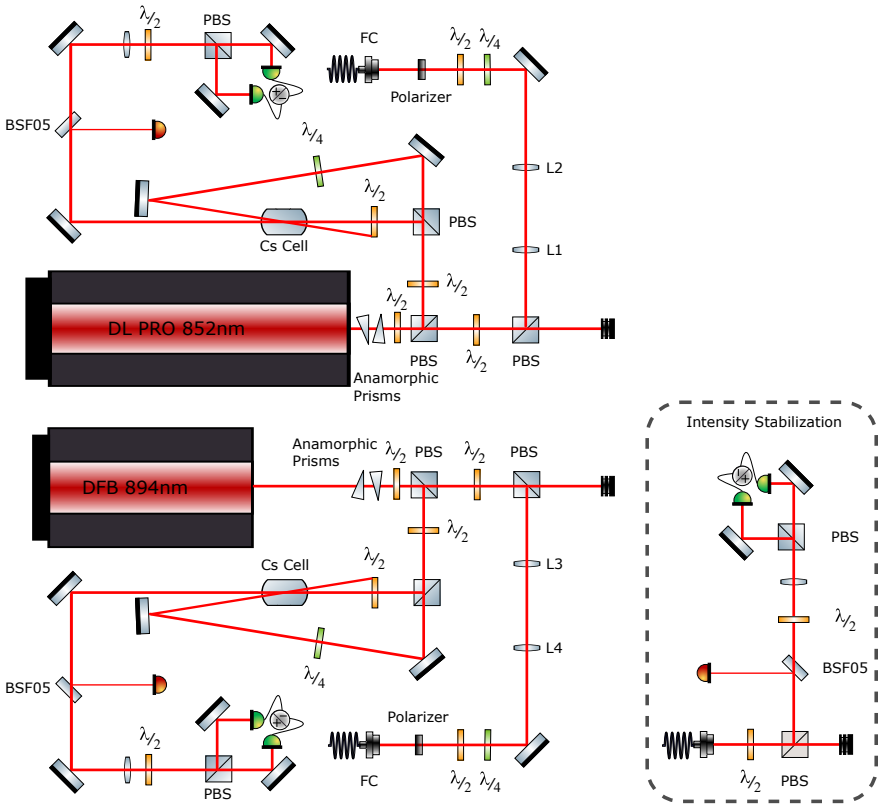

Figure 10.1: Schematic of the experimental setup for the optical pumping. The pump is an 894 nm Toptica DFB diode laser and the probe an 852 nm Toptica DL Pro diode laser. Both of which are frequency locked at a defined atomic transition using the polarization spectroscopy technique. The inset inside the dashed rectangle is a representation of the intensity stabilization scheme.

[1] Distributed feedback.

Their beams are then split at a polarizing beamsplitter (PBS) and a small part is tapped off and sent to a polarization spectroscopy (Pearman *et al.*, 2002) scheme to generate the signal for locking the laser. The remaining portion of the light is sent via a fiber (FC) to be sent to the atomic sample for the optical pumping.

In order to prepare a polarization state and measure polarization noise we have our atomic sample in a magnetic shield to have a homogeneous low noise magnetic field acting on the atoms. Then we could perform a Magneto Optical Resonance Signal (MORS) measurement to obtain the Larmor frequency, calculate the spin polarization and measure the projection noise. We will discuss these measurements in the next chapter where we introduce the results. Given the access restrictions to the lab due to the pandemic, we were not able test the final atomic sample and see how the optical pumping affects the polarization noise in it. Figure 10.2 is an actual picture of our optical pumping setup.

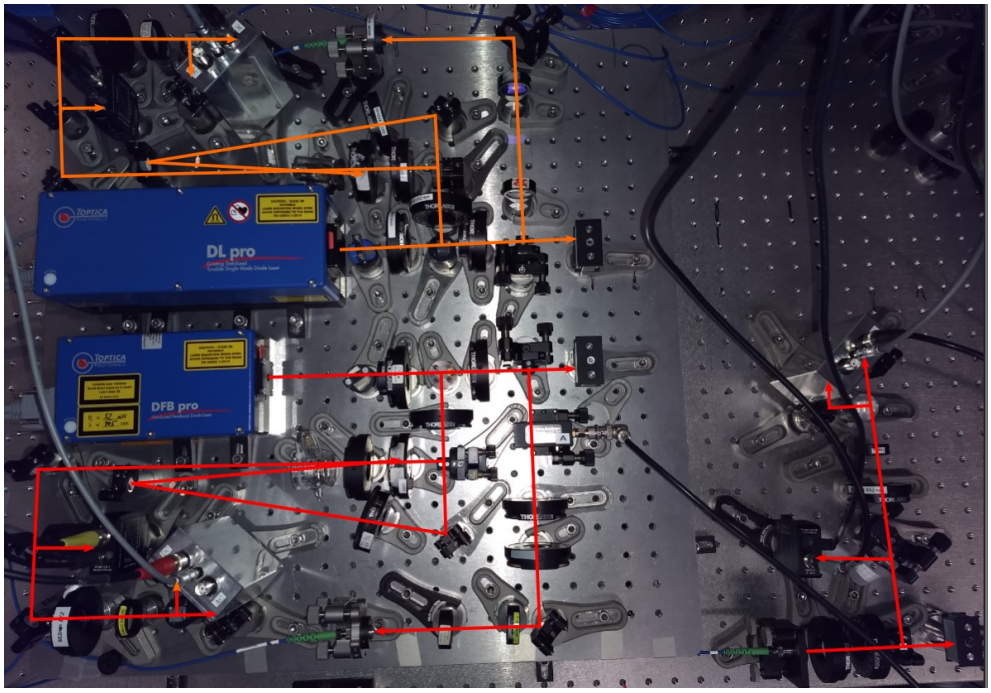

Figure 10.2: Picture of the optical pumping setup. The red and orange lines represent the optical path as the beam leaves the laser. The small setup in the bottom right is the intensity stabilization scheme.

10.1.2 Polarization Spectroscopy

As introduced in section 9.2, we want the pump to excite transitions from $F = 4$ to $F' = 4$ in the $D1$ line and the repump from $F = 3$ to $F' = 4$ in the $D2$ line. Hence, we need our lasers to have their central frequencies locked at these specific lines so that they will have the highest probabilities to excite the desired transitions. These transitions are depicted in figure 10.3 for the hyperfine levels of Cesium 133. The probe beam should be slightly detuned from the atomic transitions to avoid absorption.

Saturated absorption and polarization spectroscopy are important tools with many interesting applications in physics. We will not go through them in detail at this time. Much like we did with the optical pumping, we will briefly explain some core concepts necessary to understand how we can use them to lock our laser frequencies to an atomic transition. For more detailed description on saturated absorption and polarization spectroscopy we recommend the works of Schmidt *et al.* (1994); Pearman *et al.* (2002); Ratnapala *et al.* (2004); Harris *et al.* (2006).

As already discussed in previous sections, when near resonant light interacts with an atomic sample, part of it is scattered by an amount that mostly depends on the photon absorption cross section.

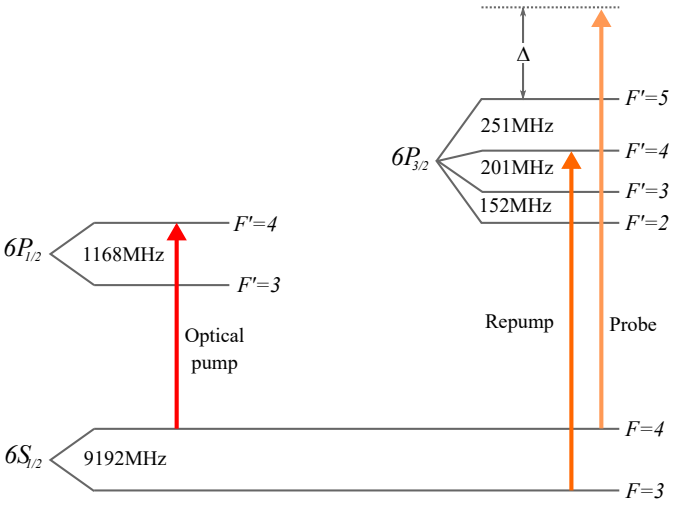

Figure 10.3: Atomic transitions in which pump and repump are locked to prepare the spin state. The pump is locked in the $F = 4 \longrightarrow F' = 4$ transition for the D1 line and the repump in the $F = 3 \longrightarrow F' = 4$ for the D2 line. The probe is Δ-detuned from the transition resonances.

Typically this cross section is determined by the lifetime of the excited state, by pressure broadening due to atomic collisions and Doppler Broadening due to thermal motion.

The combined effect of these phenomena results in an absorption lineshape that is a convolution of the Gaussian profile, given by the Maxwellian distribution due to Doppler broadening, and the Lorentzian profile due to the other two effects. This profile can be picked up by setting the laser to scanning mode around the resonance frequency and placing a photodetector on the probe beam (figure 10.4). The linewidth of the Doppler broadening is typically much larger than the linewidth of the hyperfine transitions, preventing us from resolving the hyperfine levels.

By sending a counter propagating beam (called pump in figure 10.4), much stronger than the probe, we can saturate the an atomic transition. This saturation essentially means that the pump induces such fast transitions (in both directions) between the populations of the ground and excited states, that the populations are balanced and absorption is reduced for this transition. This effect is responsible for the small peaks in the middle of the dips in figure 10.5a and in the red lines in figure 10.6, and is called *Saturated Absorption Spectroscopy* (Schmidt *et al.*, 1994).

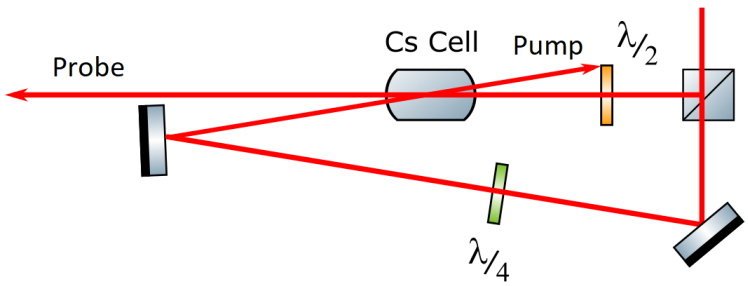

Figure 10.4: Schematic representation of the setup used for the polarization spectroscopy.

To obtain the signal we need to lock the lasers at an atomic transition we use a technique called *Polarization Spectroscopy* (Pearman *et al.*, 2002). It is closely related to the saturation absorption spectroscopy, but takes into account the birefringence induced in the atomic sample by circularly polarized light to generate a spectrum with a natural zero crossing at the transition resonance. It is then sent to a PID controled by a Redpitaya to feedback the current to the laser and stabilize it. The signal in figure

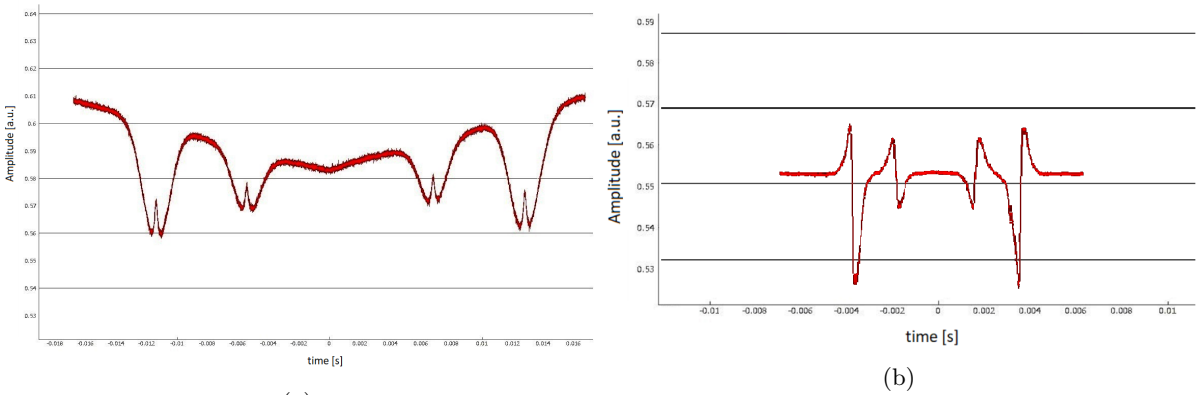

(a) (b)

Figure 10.5: Saturated absorption spectrum (a) and polarization spectroscopy signal (b) for the pump @ 894 nm, D1 transition of ^{133}Cs.

10.5b and the green signal in figure 10.6 are the actual polarization spectroscopy signals we use to lock our pump and repump lasers, respectively. The ramp at the transition provides a good feedback signal for the laser stabilization. Frequency is swept by changing the current in the laser diodes.

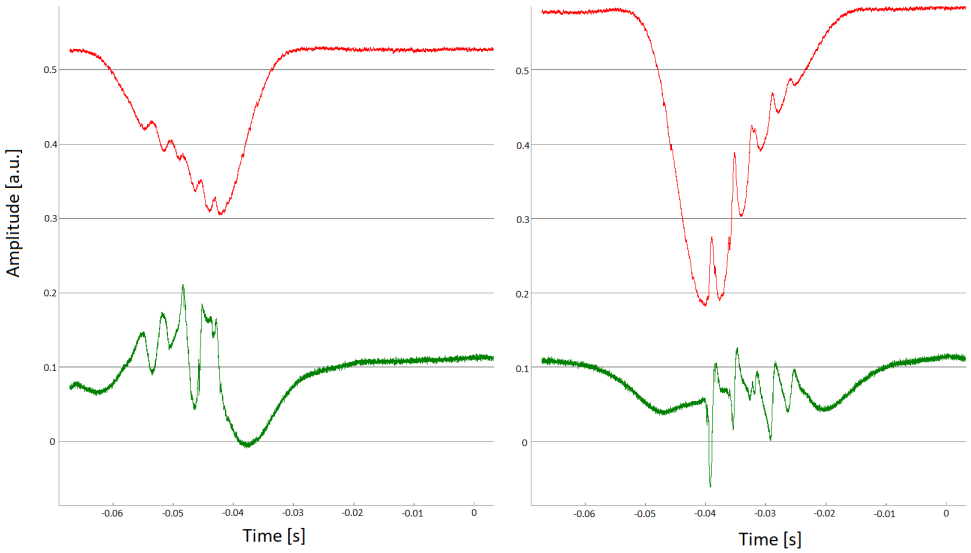

Figure 10.6: Saturated absorption spectrum (red lines) and polarization spectroscopy signal (green lines) for the repump @ 852 nm, D2 transition of ^{133}Cs.

10.2 The MORS Setup

The experiments with the cell inside the magnetic shield were performed in two distinct locations. The MORS and polarization noise measurements took place in the Cell Lab at the NBI, while the degaussing and free induction decay experiments were made in the GWD[2] lab, also at the NBI. In the configuration shown in figure 9.4, a cubic 5 mm Cesium cell is placed in the center of the magnetic shield. The pump and repump beams are σ_+ polarized in the x-direction to prepare the polarization state. A constant magnetic field (B_{bias}), also in the x-direction, breaks the degeneracy of the Zeeman sublevels and is responsible for the Larmor precession of the atomic spin. A radio frequency magnetic field (B_{RF})

[2]Gravitational-wave detector.

in the y-direction induces weak transitions between two adjacent Zeeman sublevels and this is picked up as polarization rotations of the linearly polarized probe using a balanced detection scheme. There are small variations to this setup depending on the information we want from the experiment and those will be made clear when explaining each individual result.

In the next chapter we present the atomic polarization results obtained using the optical pumping described here and measured using the MORS signal. We also introduce and discuss the results of a technique used to improve the shielding of magnetic shields called degaussing.

11 RESULTS AND MEASUREMENTS

In this chapter we will present the preliminary measurements we made with a Cesium cell inside a magnetic shield.

11.1 MORS measurement

The *MORS* measurements presented below were performed to get an experimental understanding of the technique. We used a 5 mm cesium cell placed in the center of the magnetic shield. This cell is usually used to map the magnetic field inside the shield and that is why is much smaller than the 8 cm cell that we planned to use in the final measurements. A larger cell would provide a higher optical depth that is essential for an efficient implementation of the backaction cancellation scheme (Khalili and Polzik, 2018).

The measurements were performed under the same conditions introduced in section 10.2, differing only by the presence or absence of the pump and repump beams. A bias magnetic field with a Larmor frequency of 514.7 kHz was applied in the x-direction and a weak oscillating field in the y-direction as shown in figure 9.4. The oscillating field was provided by an oscillating current generated by a lock-in amplifier that also demodulates the signal measured by the balanced detection. The sampling results were exported to a data file and are presented in figure 11.1.

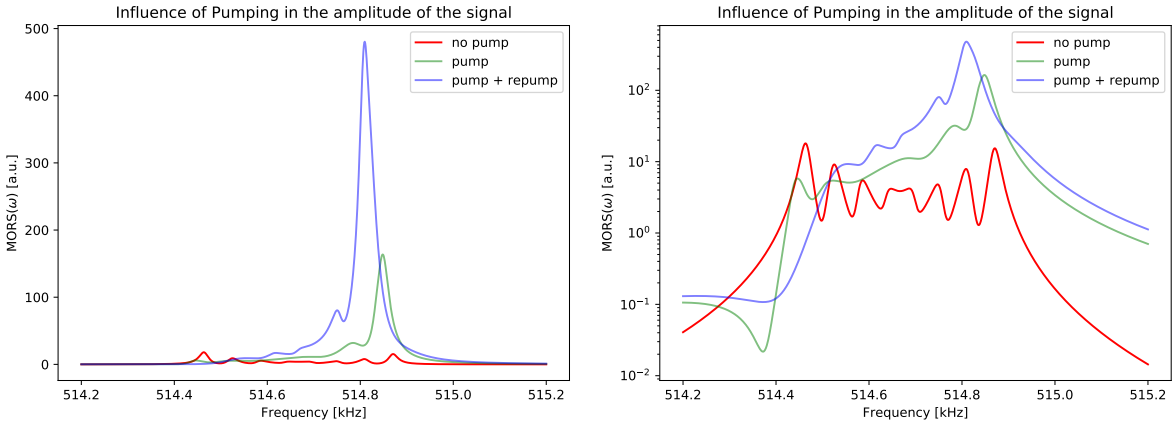

(a) Linear plot.

(b) Logarithmic plot.

Figure 11.1: Plots comparing the amplitude of the MORS signal between three different spin orientations: $p = 0.02$ with no optical pumping (red lines), $p = 0.76$ with a weak pump (gree lines) and $p = 0.88$ with pump and repump (blue lines). The linear plot allows the visualization of how relevant spin orientation is to the amplitude of the MORS signal. The logarithmic plot makes it easier to perceive the differences in the populations between the Zeeman sublevels.

In the fist measurement depicted in the red curve in figure 11.1a we allowed only the probe beam through the cell, with no optical pumping (no pump), and obtained a spin orientation of $p = 0.02$ (equation 9.32). For the second measurement in the green curve we added a 2.5 µW pump beam and the spin orientation increased to $p = 0.76$. Finally, for the third measurement in the blue curve, with the 2.5 µW pump and a weak repump (around 1 mW) we measured a spin orientation of $p = 0.88$. Keeping these results in mind when looking at figure 11.1, we can see that the amplitude of the signal increases with a higher spin orientation.

There are two main reasons for the amplitude of the signal to increase with the spin orientation and both are related to equation 9.31. One is the fact that the signal depends on the mean value of the differences in the populations between two adjacent Zeeman levels squared $|\langle\hat{\sigma}_{m+1,m+1} - \hat{\sigma}_{m,m}\rangle|^2$. For a

sample at room temperature, such as ours, and no optical pumping, this means that the populations are evenly distributed and the differences are close to zero. When the polarization increases, the populations tend to concentrate in the higher m_F Zeeman levels (for a σ_+ polarized pump) generating an imbalance in the populations and increasing the amplitude of the signal. The other reason is that resonances add up coherently. When the optical pumping sends the populations to the higher m_F levels (again for σ_+ polarization), the Lorentzians representing each response for adjacent Zeeman levels interfere constructively, further increasing the amplitude of the MORS signal (as seen in equation 9.31).

We then performed another experiment to study the polarization noise. In figure 11.2a we prepared the spin state with a 1 mW repump and no pump to obtain a spin orientation of $p = 0.68$. Then, adding a 5 µW pump we can now observe a single peak in figure 11.2b. The orientation in this situation increased to $p = 0.90$.

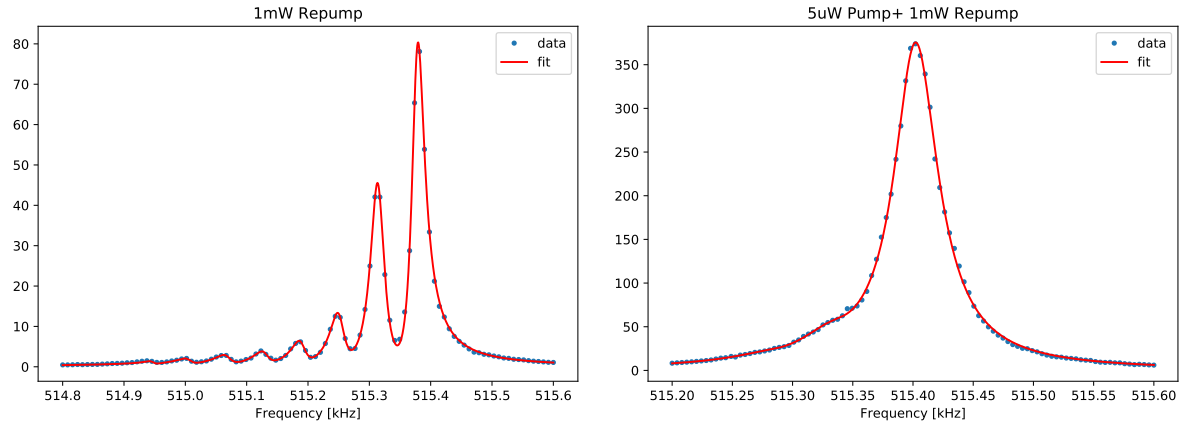

(a) (b)

Figure 11.2: Preparation of a spin state to measure the polarization noise. With a 1 mW Repump the spin orientation is $p = 0.68$ (a). Adding the pump it increases to $p = 0.90$ (b).

11.2 Polarization Noise measurement

Initially we prepared the states in figure 11.2 with a Larmor frequency of 515.4 kHz and then we reduced the amplitude of the bias field, while keeping everything else the same, to measure the polarization noise at lower frequencies. The spectrum in figure 11.3a shows the power spectral density after the balanced detection. The blue spectrum encompasses the electronic noise, shotnoise and atomic noise. It has a peak at 23.5 kHz which is associated with the atomic noise, while the base line represents the probe shotnoise. On figure 11.3b we fit a Lorentzian to the data points in that peak and obtain a linewidth of 70 Hz for the polarization noise at 23.5 kHz.

For the backaction cancellation in gravitational-wave detectors, we are interested in the smallest possible value for the spin linewidth. This, according to Khalili and Polzik (2018), would make the system linewidth dominated by the readout rate Γ_S (the spin oscillator readout rate was introduced in equation 8.5), making it easier to achieve the required parameters for the experimental implementation of this scheme.

11.2.1 Degaussing

Our last set of measurements is related to the characterization of the magnetic shield after it was moved to our lab. The ability of a magnetic shield to minimize the field inside a region may be reduced by its displacement to another location with different sources of magnetic field. The process of

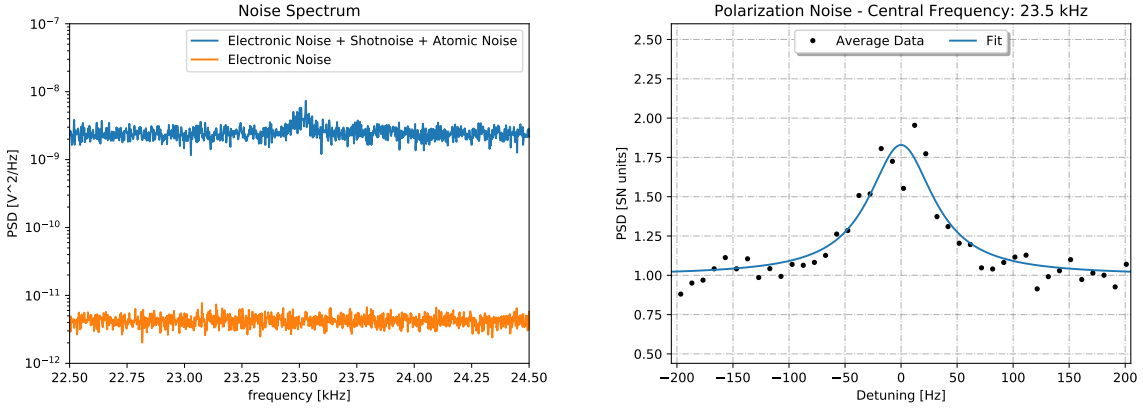

(a) (b)

Figure 11.3: (a) Power spectral density after balanced detection. (b) Fitting of the polarization noise spectrum indicates a linewidth of 70 Hz at 23.5 kHz.

bringing the internal field back to a minimum is called *degaussing* and is done, in our case, by applying a strong oscillating current to a large coil wrapped around the shield to have a strong oscillating magnetic field acting on it. Then, by slowly bring the current down to zero, the amplitude of the oscillating field will be slowly reduced and the magnetic moments inside the shield will align as to cancel each other out, leaving little to none remnant field inside.

To make sure that the degaussing worked we estimate the Larmor frequency of the atomic sample inside the shield before and after the process for comparison. The method we used for this measurement is called *free induction decay*, and it consists in applying a pulsing signal in the coils to generate a pulse of an oscillating magnetic field close to the Larmor frequency of the atomic sample. The polarized spin in the atomic sample will behave like a driven harmonic oscillator with the spin precessing with the frequency of the external pulse for as long as it lasts. When the pulse stops, the system falls back to a damped oscillator. Since the frequency of a damped oscillator is the resonance frequency for the system, by measuring the decay frequency we can measure the Larmor frequency of the remnant field inside the shield.

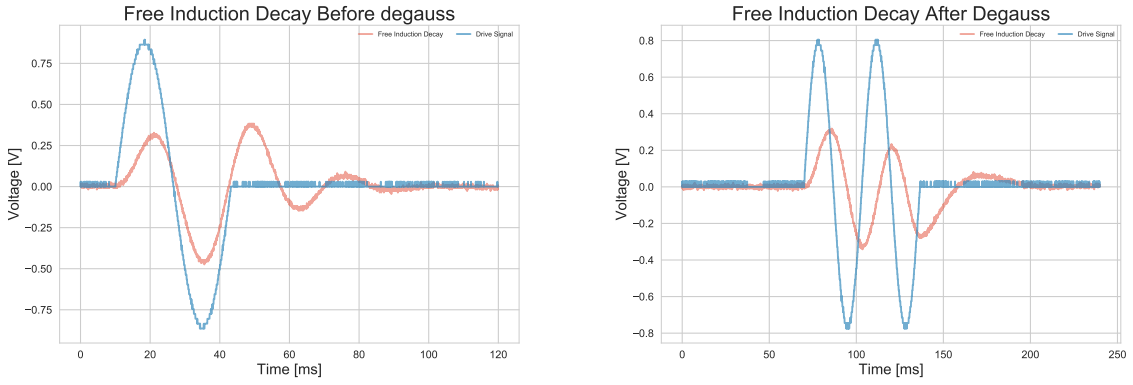

(a) (b)

Figure 11.4: (a) Free induction decay before degaussing indicates a Larmor frequency of 36 Hz. (b) After degaussing the free induction decay indicates that the Larmor frequency was reduced to 15 Hz.

We use the pump beam to obtain a higher spin orientation and increase the interaction with the magnetic field, and have the probe detuned from the atomic transitions to avoid absorption. In figure

11.4a we have the free induction decay before degaussing as the orange line. The blue line indicates the driving signal. We can see that, as expected, for the duration of the pulse, the free induction decay has roughly the same frequency as the driving signal. We calculate the Larmor frequency from the free induction decay after the pulse stops and find it to be around 36 Hz. In figure 11.4b we have the free induction decay after degaussing. Using the same procedure we find a Larmor frequency of 15 Hz, indicating that the degaussing of the magnetic shield was successful.

Given that the free induction decay is a coarse measurement, specially given that after degaussing the damping of the oscillation happens really fast, we decided to compare it with a 'MORS-like' measurement at this frequency. Basically we use a weak pump to have a better polarization of the atomic sample but no bias magnetic field. Then, we set the sweep range of the oscillating magnetic field B_{RF} between 3 Hz and 100 Hz and recorded the signal obtained from the atomic response. Given that there is no bias magnetic field provided by the coils in the experiment, the central frequency obtained from the MORS model would give the background magnetic field inside the shield. The procedure is very similar to the actual MORS measurement, but instead of fitting the MORS model we fit a single Lorentzian to the experimental data as shown in figure 11.5. The fitting resulted in a value of 10 Hz for the Larmor frequency.

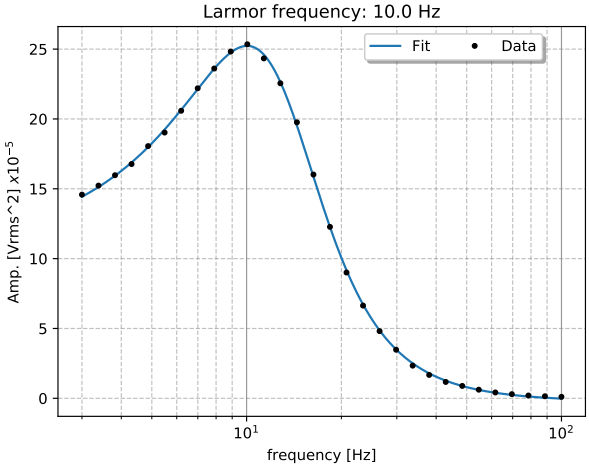

Figure 11.5: Lorentzian fit for the measured data indicates a Larmor frequency of $10Hz$.

We can conclude by comparing the free induction decay with this last measurement that the Larmor frequency of the shield after degaussing should be roughly around 10 Hz, a value low enough that it can be overlooked in measurements at higher frequencies, for instance, larger than 1 kHz. The next step would be to add the new coils, developed in the NBI group in a parallel project, and use them to try to compensate even further the effects of the residual field. These new coils would provide a more stable magnetic field and also allow for the implementation of a gradient field to compensate for the contamination of any background magnetic field that manages to get through the shield.

12 CONCLUSION

Initially we wanted to characterize one of the candidate cells ($8cm$ long) for the GWD setup by preparing a polarization state, using the pump and repump described in chapter 10.1, and measuring it along with its polarization noise. However, the quarantine took effect after we finished moving the magnetic shield to our laboratory and were about to start characterizing the magnetic field inside it.

Nevertheless, we were able to build system capable of preparing an atomic spin with the intention of using it as a negative mass reference frame in a back-action cancellation scheme. We began by building an optical pumping system and by using polarization spectroscopy to frequency lock the pump and repump lasers to specific atomic transitions between two desired hyperfine levels. They are then used to prepare the atomic spin state, which will be measured using the MORS technique.

With the pump and repump built we started taking measurements with a small cell inside the magnetic shield at its original location, the Cell Lab. We began by using the MORS technique to measure the spin orientation of an atomic sample as a way of better understanding the MORS. In a subsequent measurement we prepared a polarization state an measured the polarization noise associated with it. These measurements will be important in the future, when we set out to characterize the atomic cells we want to use in the back-action cancellation system.

Lastly, we moved the magnetic shield to the GWD Lab, performed a degaussing of the shield to improve its shielding at the new location and measured the Larmor frequency inside it to be around 10 Hz. We then decided to proceed with the next step, which would be to add the new coils and map the magnetic field along the longitudinal axis of the shield using the field generated by the coils to cancel, as best as possible, any residual field. This implementation was performed after my return to Brazil with the resuming operations in the lab. The techniques learned in this experience will set the basis for the atomic implementation in our lab targeting the development of quantum information protocols between atoms and light.

Part IV

Summary and Outlook

13 GENERAL CONCLUSION

In this thesis we wanted to build a system capable of generating entangled states of light in an OPO and also to prepare at an atomic polarization state. The future goal would be the implementation of a teleportation protocol between atoms and light resonant at different wavelengths.

For that we built an optical parametric oscillator capable of generating entanglement between signal and idler as shown by the violation of the DGCZ separability criterion. However, despite the squeezing of 2.4 dB in the amplitude subtraction quadrature, the sum of the phases presented excess noise. The tripartite analysis indicated that phonon noise was degrading the correlations due to the introduction of phase noise and that lowering the crystal temperature would be the best course of action towards improving the entanglement between the three beams. After reworking the cooling system of the OPO we were able to achieve the temperature of $-21\,^{\circ}\mathrm{C}$. We realigned the system e took some test measurements to check its operation conditions, but our works had to be interrupted because of the beginning of the internship at the Niels Bohr Institute for the realization of the second part of this work.

At the NBI we built an optical pumping system from scratch to be used in the preparation of an atomic polarization state. Using this pumping system, a magnetic shield and magnetic fields generated by coils, we were able to prepare and characterize an atomic polarization state with 90 % of the ensemble with the desired orientation and with a polarization noise of 2.6 dB above the shotnoise limit with a linewidth of 70 Hz and a central frequency of 23.5 kHz. These were supposed to be preliminary measurements and while we were in the middle of adding the final cell and new coils to improve the cell illumination and reduce the magnetic field noise the quarantine took effect in Denmark and we were not allowed in the lab. This was early March and we could not return until after I came back to Brazil in May.

Upon my return to Brazil, quarantine restrictions here prevented us from resuming our work with the OPO to improve the tripartite measurements and hopefully achieve better results. However, we are confident that the system is capable of achieving better results after some effort in improving the stability of the pump, essentially by reducing intensity fluctuations in the Ti:Sapph laser.

Once the OPO reaches its final goal of generating tripartite entanglement, with violation of the van Loock Furusawa inequalities, the preparation of an atomic polarization state with rubidium cells would be considered. With these two systems working properly the final step would be preparing the system for the implementation of quantum information protocols, such as teleportation. This would be an important step towards the development of quantum networks in our lab.

13.1 Teleportation protocol

A proposal of a teleportation protocol between atoms and light can be seen in figure 13.1. There, a triply resonant OPO generates entanglement between the reflected pump, signal and idler. A small sample is picked off the pump by the first beam splitter and sent to the Victor station to probe the atomic polarization state. The polarization state is prepared by the magnetic field B_{bias}, the pump and the repump in a coherent spin state by pumping the atoms to one of the extreme Zeeman levels of the ground state of rubidium. After interacting with the atomic sample the probe beam is mixed with the reflected pump at the Alice station, where a Bell measurement is performed.

The resulting signal is then sent through a classical channel to the Bob station, where the first electro-optical modulator (EOM) modulates the amplitude quadrature (AM) of one of the twin beams while the second EOM modulates the phase quadrature (PM) after having the noise ellipse rotated by the cavity to have phase converted to amplitude. The gain G in each channel is adjusted as to maximize the fidelity of the teleported state. The resulting state is measured at Victor and is then compared with the initial state prepared at the first Victor station to obtain the fidelity. Essentially, as introduced in section

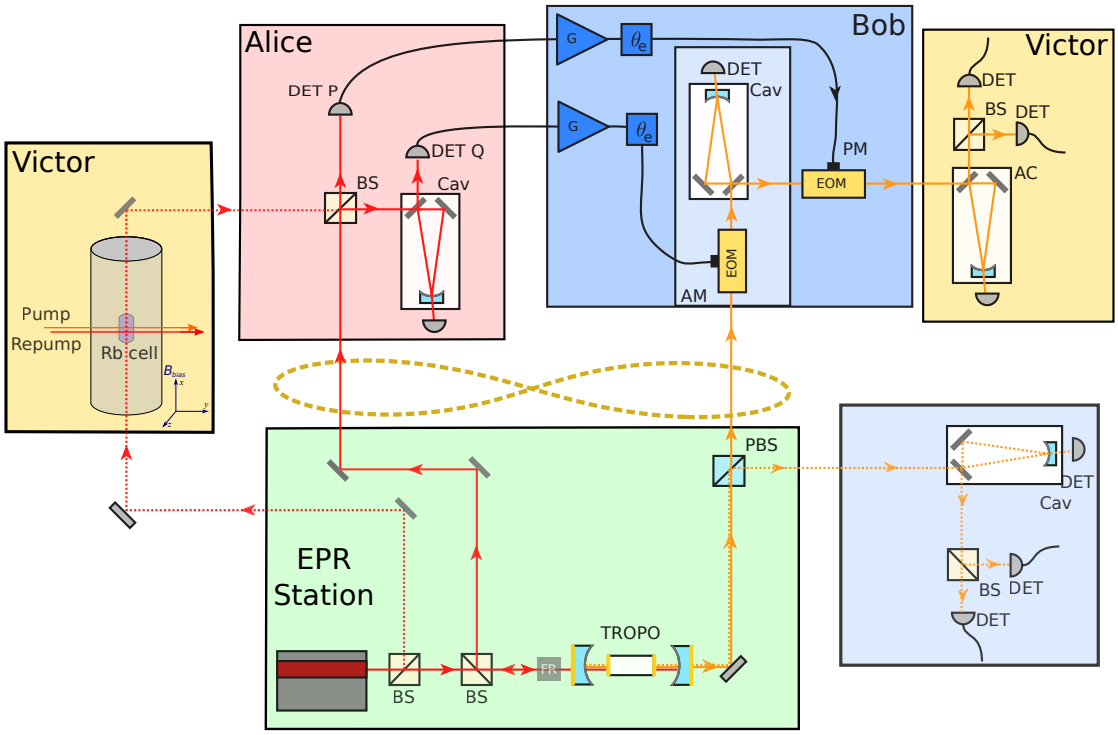

Figure 13.1: Proposal of the teleportation protocol of an atomic polarization state prepared in a rubidium cell and light.

8.1.2, the teleported quadratures will be the projection of the spin in the z direction $\hat{X}_S = \hat{J}_z/\hbar\sqrt{J_x}$ and the projection of the spin in the y direction $\hat{P}_S = \hat{J}_y/\hbar\sqrt{J_x}$, where $J_x = |\langle \hat{J}_x \rangle|/\hbar \gg 1$.

Since this configuration only uses the reflected pump and one of the twin beams, the fidelity is limited and may not overcome the non-cloning limit. For more information on why this is true in our system, and on similar scheme where the other twin beam can be used to improve the fidelity, refer to Andrade (2018).

BIBLIOGRAPHY

Albarelli, F., M. G. Genoni, M. G. A. Paris, and A. Ferraro, 2018 Resource theory of quantum non-Gaussianity and Wigner negativity. Physical Review A **98**: 052350.

Andrade, R. B. d., 2018 *Oscilador Paramétrico Ótico para uma interface átomos-luz*. Ph.D. thesis, Universidade de São Paulo.

Bachor, H. and T. C. Ralph, 2019 *A Guide to Experiments in Quantum Optics*. Wiley, third edition.

Barbosa, F. A. S., A. S. Coelho, K. N. Cassemiro, P. Nussenzveig, C. Fabre, A. S. Villar, and M. Martinelli, 2013 Quantum state reconstruction of spectral field modes: Homodyne and resonator detection schemes. Physical Review A **88**: 052113.

Barbosa, F. A. S., A. S. Coelho, L. F. Muñoz-Martínez, L. Ortiz-Gutiérrez, A. S. Villar, P. Nussenzveig, and M. Martinelli, 2018 Hexapartite Entanglement in an above-Threshold Optical Parametric Oscillator. Physical Review Letters **121**: 073601.

César, J. E. S., A. S. Coelho, K. N. Cassemiro, A. S. Villar, M. Lassen, P. Nussenzveig, and M. Martinelli, 2009 Extra phase noise from thermal fluctuations in nonlinear optical crystals. Physical Review A **79**: 063816.

Coelho, A. S., F. A. S. Barbosa, K. N. Cassemiro, A. S. Villar, M. Martinelli, and P. Nussenzveig, 2009 Three-Color Entanglement. Science **326**: 823–826.

Coelho, A. S. O., 2009 *Emaranhamento Tripartite no Oscilador Paramétrico Ótico*. Master's thesis, Universidade de São Paulo.

Cohen-Tannoudji, C., B. Diu, and F. Laloe, 1991 *Quantum Mechanics*. Wiley.

Debuisschert, T., A. Sizmann, E. Giacobino, and C. Fabre, 1993 Type-II continuous-wave optical parametric oscillators: oscillation and frequency-tuning characteristics. Journal of the Optical Society of America B **10**: 1668.

Duan, L.-M., G. Giedke, J. I. Cirac, and P. Zoller, 2000 Inseparability Criterion for Continuous Variable Systems. Physical Review Letters **84**: 2722–2725.

Eckardt, R. C., C. D. Nabors, W. J. Kozlovsky, and R. L. Byer, 1991 Optical parametric oscillator frequency tuning and control. Journal of the Optical Society of America B **8**: 646.

Ekert, A. K., 1991 Quantum cryptography based on Bell's theorem. Physical Review Letters **67**: 661–663.

Fabre, C., E. Giacobino, a. Heidmann, L. Lugiato, S. Reynaud, M. Vadacchino, and W. Kaige, 1990 Squeezing in detuned degenerate optical parametric oscillators. Quantum Optics: Journal of the European Optical Society Part B **2**: 159–187.

Furusawa, A., J. L. Sørensen, S. L. Braunstein, C. A. Fuchs, H. J. Kimble, and E. S. Polzik, 1998 Unconditional Quantum Teleportation. Science **282**: 706–709.

Furusawa, A. and P. van Loock, 2011 *Quantum Teleportation and Entanglement*. Wiley-VCH Verlag GmbH & Co. KGaA, Weinheim, Germany.

Galatola, P., L. Lugiato, M. Porreca, P. Tombesi, and G. Leuchs, 1991 System control by variation of the squeezing phase. Optics Communications **85**: 95–103.

Glauber, R. J., 1963 The Quantum Theory of Optical Coherence. Physical Review **130**: 2529–2539.

HAPPER, W., 1972 Optical Pumping. Reviews of Modern Physics **44**: 169–249.

Happer, W. and W. A. Van Wijngaarden, 1987 An optical pumping primer. Hyperfine Interactions **38**: 435–470.

Harris, M. L., C. S. Adams, S. L. Cornish, I. C. McLeod, E. Tarleton, and I. G. Hughes, 2006 Polarization spectroscopy in rubidium and cesium. Physical Review A **73**: 062509.

Julsgaard, B., 2003 *Entanglement and Quantum Interactions with Macroscopic Gas Samples*. Ph.D. thesis, University of Aarhus.

Julsgaard, B., A. Kozhekin, and E. S. Polzik, 2001 Experimental long-lived entanglement of two macroscopic objects. Nature **413**: 400–403.

Julsgaard, B., J. Sherson, J. L. Sørensen, and E. S. Polzik, 2004 Characterizing the spin state of an atomic ensemble using the magneto-optical resonance method. Journal of Optics B: Quantum and Semiclassical Optics **6**: 5–14.

Khalili, F. Y. and E. S. Polzik, 2018 Overcoming the Standard Quantum Limit in Gravitational Wave Detectors Using Spin Systems with a Negative Effective Mass. Physical Review Letters **121**: 031101.

Kimble, H. J., 2008 The quantum internet. Nature **453**: 1023–1030.

Kogelnik, H. and T. Li, 1966 Laser Beams and Resonators. Applied Optics **5**: 1550.

Krauter, H., C. A. Muschik, K. Jensen, W. Wasilewski, J. M. Petersen, J. I. Cirac, and E. S. Polzik, 2011 Entanglement Generated by Dissipation and Steady State Entanglement of Two Macroscopic Objects. Physical Review Letters **107**: 080503.

Krauter, H., D. Salart, C. A. Muschik, J. M. Petersen, H. Shen, T. Fernholz, and E. S. Polzik, 2013 Deterministic quantum teleportation between distant atomic objects. Nature Physics **9**: 400–404.

Mandel, L. and E. Wolf, 1995 *Optical coherence and quantum optics*. Cambridge University Press.

Mari, A. and J. Eisert, 2012 Positive Wigner Functions Render Classical Simulation of Quantum Computation Efficient. Physical Review Letters **109**: 230503.

Martinelli, M., C. L. Garrido Alzar, P. H. Souto Ribeiro, and P. Nussenzveig, 2001 Classical and quantum properties of optical parametric oscillators. Brazilian Journal of Physics **31**: 597–615.

Møller, C. B., 2018 *Quantum Back-Action Evasion in a Hybrid Spin-Optomechanical System*. Ph.D. thesis, University of Copenhagen.

Moraes, F. C. D. D., 2013 *Construção e caracterização de um laser contínuo de titânio-safira*. Master's thesis, Universidade de São Paulo, São Paulo.

Muñoz-Martínez, L. F., F. A. S. Barbosa, A. S. Coelho, L. Ortiz-Gutiérrez, M. Martinelli, P. Nussenzveig, and A. S. Villar, 2018 Exploring six modes of an optical parametric oscillator. Physical Review A **98**: 1–10.

Nielsen, M. A. and I. L. Chuang, 2010 *Quantum Computation and Quantum Information*. Cambridge University Press, Cambridge.

Pearman, C. P., C. S. Adams, S. G. Cox, P. F. Griffin, D. A. Smith, and I. G. Hughes, 2002 Polarization spectroscopy of a closed atomic transition: applications to laser frequency locking. Journal of Physics B: Atomic, Molecular and Optical Physics **35**: 5141–5151.

Pitkin, M., S. Reid, S. Rowan, and J. Hough, 2011 Gravitational wave detection by Interferometry (Ground and Space). Living Reviews in Relativity **14**: 5.

Ratnapala, A., C. J. Vale, A. G. White, M. D. Harvey, N. R. Heckenberg, and H. Rubinsztein-Dunlop, 2004 Laser frequency locking by direct measurement of detuning. Optics Letters **29**: 2704.

Schleich, W. P., 2001 *Quantum Optics in Phase Space*. Wiley-VCH Verlag GmbH & Co. KGaA, Weinheim, FRG.

Schmidt, O., K. M. Knaak, R. Wynands, and D. Meschede, 1994 Cesium saturation spectroscopy revisited: How to reverse peaks and observe narrow resonances. Applied Physics B Lasers and Optics **59**: 167–178.

Scully, M. O. and M. S. Zubairy, 1997 *Quantum Optics*. Cambridge University Press.

Seltzer, S. J., 2008 *Developments in Alkali-Metal Atomic Magnetometry*. Ph.D. thesis, Princeton University.

Siegman, A. E., 1986 *Lasers*. University Science Books.

Simon, R., 2000 Peres-Horodecki Separability Criterion for Continuous Variable Systems. Physical Review Letters **84**: 2726–2729.

Specht, H. P., C. Nölleke, A. Reiserer, M. Uphoff, E. Figueroa, S. Ritter, and G. Rempe, 2011 A single-atom quantum memory. Nature **473**: 190–193.

Steck, D. A., 2019 "Cesium D Line Data". Available online at http://steck.us/alkalidata (revision 2.2.1, 21 November 2019).

The LIGO Scientific Collaboration and the Virgo Collaboration, 2016 Observation of Gravitational Waves from a Binary Black Hole Merger. Physical Review Letters **116**: 061102.

Tsang, M. and C. M. Caves, 2010 Coherent Quantum-Noise Cancellation for Optomechanical Sensors. Physical Review Letters **105**: 123601.

Tsang, M. and C. M. Caves, 2012 Evading Quantum Mechanics: Engineering a Classical Subsystem within a Quantum Environment. Physical Review X **2**: 031016.

van Loock, P. and A. Furusawa, 2003 Detecting genuine multipartite continuous-variable entanglement. Physical Review A **67**: 052315.

Villar, A., M. Martinelli, and P. Nussenzveig, 2004 Testing the entanglement of intense beams produced by a non-degenerate optical parametric oscillator. Optics Communications **242**: 551–563.

Villar, A. S., 2008 The conversion of phase to amplitude fluctuations of a light beam by an optical cavity. American Journal of Physics **76**: 922–929.

Villar, A. S., K. N. Cassemiro, K. Dechoum, A. Z. Khoury, M. Martinelli, and P. Nussenzveig, 2007 Entanglement in the above-threshold optical parametric oscillator. Journal of the Optical Society of America B **24**: 249.

Villar, A. S., M. Martinelli, C. Fabre, and P. Nussenzveig, 2006 Direct Production of Tripartite Pump-Signal-Idler Entanglement in the Above-Threshold Optical Parametric Oscillator. Physical Review Letters **97**: 140504.

Walls, D. F. and G. J. Milburn, 2008 *Quantum Optics*. Springer Berlin Heidelberg, Berlin, Heidelberg.

Wootters, W. K. and W. H. Zurek, 1982 A single quantum cannot be cloned. Nature **299**: 802–803.

Zeuthen, E., E. S. Polzik, and F. Y. Khalili, 2019 Gravitational wave detection beyond the standard quantum limit using a negative-mass spin system and virtual rigidity. Physical Review D **100**: 62004.